Doctoral Dissertation

博士論文

3-D isotropic and anisotropic structure in the lowermost mantle beneath the circum-Pacific inferred using waveform inversion: Constraints on geodynamics above the core-mantle boundary

(波形インバージョンによる環太平洋下の最下部マントルの 3 次元等方 S 波速度及び異方性構造の推定：核–マントル境界上のダイナミクスの制約)

A Dissertation Submitted for the Degree of Doctor of Philosophy

December 2019

令和元年１２月博士（理学）申請

Department of Earth and Planetary Science,

Graduate School of Science, The University of Tokyo

東京大学大学院理学系研究科地球惑星科学専攻

Yuki Suzuki

鈴木 裕輝

Abstract

In this study, we extended our group's localized waveform inversion methods to infer 3-D transverse isotropic structure with a vertical symmetric axis (VTI), applied it to a large dataset to infer the large-scale heterogeneity in a broad area, obtained new data from seismic array observations, and confirmed that the method used in this study is sufficiently robust to infer 3-D structure.

The lowermost several hundred km of the Earth's mantle immediately above the core-mantle boundary (CMB), commonly called the D″ (Dee double prime) region, is the thermal boundary layer (TBL) of mantle convection and play a major role in governing the modality of convection in the mantle. The D″ region especially beneath past and present subduction zones provides clues for understanding the dynamics of the Earth's mantle, because thermally and chemically distinct slab materials can perturb the temperature and mantle flow. Hence, it is important to study (i) whether primordial material exists in D″; (ii) how thermal and chemical heterogeneity has developed in D″ especially beneath subduction zone in order to understand the thermal and chemical evolution of the Earth.

Although previous tomographic studies found a large low S-velocity (seismic shear wave velocity) provinces (LLSVPs) in the lowermost mantle beneath the Pacific, due to a lack of resolution it remains unclear whether the LLSVP consists of clusters of small-scale low-velocity anomalies or a large-scale anomaly. We recently deployed a seismic array in Thailand (TSAR) which provides a dataset with wide azimuthal coverage at the western Pacific LSLVP. We assemble the new dataset including waveforms recorded by TSAR, conduct waveform inversion for the 3-D shear wave velocity structure, and find high-velocity anomalies extending vertically to a height of

~400 km above the CMB beneath the Philippine Sea and small-scale low-velocity anomalies with a diameter of ~300 km at the CMB beneath New Guinea. As the locations of the high-velocity anomalies are consistent with the past Izanagi-plate subduction boundary, the high-velocity anomalies can be interpreted as the cold subducted slab remnant. With a diameter of ~300 km, low-velocity anomalies can be interpreted as a small-scale thermal-plume cluster which is explained by mainly thermal effect, rather than a part of thermo-chemical pile, although we cannot rule out the possibility that the low-velocity anomalies are small-scale chemical anomalies. Chemical heterogeneities resulting from basalt entrained to the base of the mantle by past subduction or as long-lived (~4 Gyr) remnants of chemical differentiation in the early Earth, can be expected at the CMB. However, the amplitude of low S-velocity anomalies in our inferred model suggest that chemical composition anomalies with an impurity content of 5–6 percent produce at most ~+1 percent density anomaly. This implies that chemical anomalies could be entrained by the convection and thus could not survive in the lowermost mantle about 4 Gyr. We therefore conclude that: (1) the shape of the low-velocity anomalies in our inferred model beneath the western Pacific appear to be plume clusters rather than a large-scale anomaly such as a thermo-chemical pile; (2) while the LLSVP may be due to the chemical effects, the inferred S-velocity structure around the edge of the western Pacific LLSVP found by this study is likely to be explained by mainly thermal effects.

Since the D″ region is considered to be destination of chemically and thermally distinct cold subducted oceanic lithosphere (slab) which interacts with the hot TBL above the CMB and cause the disturbance of temperature and flow in the lowermost mantle, we conduct waveform inversion to infer the isotropic and anisotropic structure of D″ beneath the northern Pacific in order to understand the thermal and chemical evolution

processes of the D″ region beneath the subduction zone. We analyzed not only transverse but also radial component of a large number of waveforms recorded by full USArray broadband seismic stations in the US during 2004–2015. Inferred 3-D isotropic S-velocity structure shows high-velocity anomalies possibly corresponding to subducted Izanagi slab, which reach the CMB, and low-velocity anomalies continuous from the CMB to 400 km above the CMB possibly associated with the hot material of the thermal boundary layer immediately above the CMB. We then conduct waveform inversion to infer the 3-D anisotropic structure within D″ beneath the Northern Pacific in order to infer the flow direction at the lowermost mantle. The observed positive and negative perturbation of anisotropic parameter ($\delta\xi$) is corresponding to horizontal and vertical flow in D″, respectively, taking into account the recent progress of mineral physics. Hence, it is found that paleo-Izanagi plate subducted ~240 Ma reaches the lowermost mantle, lies almost horizontally, inducing vertical upwelling flow of the hot material of the thermal boundary layer.

Our inferred seismic structure would suggest that:

(i) the LLSVP (at least the western part of the Pacific LLSVP) consists of an aggregate of smaller-scale low-velocity would be explained by mainly thermal effect, suggesting that the existence of low viscosity material in D″ beneath the western Pacific and the vigorous small-scale convection;

(ii) the slab sinks into the lowermost mantle beneath the northern Pacific with a low dip angle. This implies that segregation of basalt from depleted material could occur in this ~100 Myr, suggesting that the lowermost mantle beneath the subduction zone could be chemically distinct due to the accumulation of the basaltic materials enriched in the incompatible elements and radiogenic elements.

Table of Contents

Acknowledgments

I am deeply grateful to my PhD advisor Kenji Kawai for his teaching, guidance, and support during this PhD, and to Robert J. Geller, who supervised me during my Master course and continued to do so during my PhD. They both taught me what it is to be a researcher. I would also like to thank my three seniors Kensuke Konishi, Kei Hasegawa, and Anselme F. E. Borgeaud for their support and guidance during my Master course and this PhD. I thank my co-authors Kawai Kenji, Robert J. Geller, Kensuke Konishi, Anselme F. E. Borgeaud, Satoru Tanaka, Weerachai Siripunvaraporn, Songkhun Boonchaisuk, Noisagool Sutthipong, Yasushi Ishihara, Taweoon Kim.

I thank the members of Kenji Kawai's group: Anselme F.E. Borgeaud, Tsubasa Ue, Hanaya Okuda, Trishit Ruj, and Keyur De for their comments and advices during the group meetings. I thank the older members of Robert J. Geller's group, Nozomu Takeuchi, and Tatsuhiko Hara for helpful discussions.

I thank the professors of the Solid Earth group, especially Ataru Sakuraba, Masahiko Sato, Keisuke Nishida, Tsuyoshi Iizuka, Kei Hirose, Simon Wallis, Ryosuke Ando, and Satoshi Ide for their helpful remarks, encouragements, and advices. I also thank the professors of the Earthquake Research Institute, especially Satoru Honda, Hisayoshi Shimizu, Nozomu Takeuchi, and Takashi Iidaka, for their teachings and comments during my Master and PhD degree.

I thank the professors of the deep Earth group of the Arizona State University (ASU), especially Ed Garnero, Dan Shim, and Mingming Li for their helpful discussions, comments, encouragements, and advices during and after my stay in in the ASU.

I would also like to thank professors outside of the University of Tokyo, especially Yukio Isozaki, Nobumasa Funamori, Taku Tsuchiya, Jun Tsuchiya, Sebastian

Ritterbex, Maxim Ballmer, Takashi Nakagawa, Satoshi Kaneshima, and Toshiki Ohtaki for their teachings, advices, and encouragements. I also wish to thank Yukako Baba, Shio Watanabe, Nami Tonegawa, and Sachiko Ohishi for their great administrative support during my PhD.

I thank the office mates, especially Hajime Kawahara, Akifumi Nakayama, Yuhiko Aoyama, Keita Itano, Sho Shibata, and Tadahiro Kimura for their fruitful scientific discussions.

I also thank financial support from Leading Graduate Course for Frontiers of Mathematical Science and Physics.

Last and definitely not least, I thank my family members for their support all along the way.

Chapter 1 General introduction

1.1 Information on mantle convection from seismic tomography

Analysis of observed seismic waves is one of the most powerful tools for inferring the structure and understanding the dynamic process in the Earth's interior. Seismic mantle tomography has been used since the 1970's (Aki et al., 1977; Dziewonski et al., 1977; Sengupta & Toksöz, 1976) to analyze travel-time data to infer the Earth's 3-D structure (e.g., Romanowicz, 2003). Results from tomographic studies have contributed greatly to studies on the topics in solid Earth science such as mantle dynamics, mineral physics, and geochemistry. Further improvements in observations and methods of seismological data analysis are essential, because such progress leads to further progress in other fields of solid Earth science.

The pioneering works on 3-D seismic travel-time tomography are Aki et al. (1977), Dziewonski et al. (1977), and Sengupta & Toksöz (1976). Aki et al. (1977) and Dziewonski et al. (1977) applied inverse theory to infer the regional 3-D structure of the lithosphere beneath an array of seismic stations, and the global structure of the Earth's lower mantle, respectively, using travel-time residuals of teleseismic direct P-waves. Seismologists in 1970s and 1980s focused on the lower mantle, using P wave travel-time data (e.g., Dziewonski et al., 1977; Dziewonski, 1984), and on the upper mantle using surface wave dispersion data (e.g., Woodhouse & Dziewonski 1984; Nataf et al., 1986; Tanimoto, 1986). In parallel, many regional P-wave tomographic studies of the upper mantle inferred structure in subduction zones because of the geometry of sources and stations was favorable (e.g., Kamiya et al., 1988; van der Hilst & Spakman, 1989).

Tomographic studies on global P-velocity structure used the extensive dataset of arrival travel-time picks provided over the past 50 years in the bulletins of the International Seismological Center (ISC). In using this dataset, the large quantity of global data available (hundreds of thousands to millions of travel-time picks) compensates for the absence of control on the quality of individual picks. The tomographic mantle models are parameterized in terms of local basis functions, typically cells of size ~1° to 3° in the upper mantle, and ~1° to 5° in the lower mantle (Fukao et al., 1992; van der Hilst et al., 1997).

Since sources (mostly around subduction zones) and stations (mostly on land) are inhomegeneously distributed, P-wave travel-time tomography provides good resolution under subduction zones but less coverage under the oceans both in the upper and lower mantle. In order to improve resolution of 3-D structure under the oceans, it is necessary to add later phases to the dataset. For example, Obayashi & Fukao (1997) used PcP and investigated mantle volumetric structure as well as structure at the core mantle boundary (CMB). Boschi & Dziewonski (2000) also used PcP as well as core-phases such PKPdf and PKPbc, which allowed them to investigate trade-offs between structure in the mantle and the core. These P velocity models provided clear images of high velocity subducted slabs under the western Pacific and the Americas, and they clarified the interaction of these subducted slabs with the 660 km discontinuity around the mantle transition zone (Fukao et al., 2001). Several subducted slabs, such as beneath Alaska, Japan, and Tonga, deflected to horizontal when they hit the bottom of the upper mantle and extend over a distance of ~1000 km in the transition zone along the 660 km discontinuity, whereas others, such as beneath Mariana, Caribbean, and US, appear to penetrate deep into the lower mantle (Fukao et al., 2001).

The earliest theoretical framework using waveforms and surface wave phase velocities in tomographic studies is generally that of zeroth order asymptotic theory for normal modes and surface waves (the path average approximation (PAVA); e.g., Woodhouse & Dziewonski, 1984), in which it is assumed that sensitivity is confined to the great circle path between the epicenter and the station and varies along this path only with depth. PAVA is sufficient to compute synthetic surface wave seismograms, but it is not sufficient for body waves, which have relatively high wavenumber vertical components. Li & Tanimoto (1993) derived a more accurate method which models the body wave sensitivity to structure along the path. Li & Romanowicz (1995) then developed a nonlinear asymptotic normal mode approach (NACT, nonlinear asymptotic coupling theory), and applied it to relatively long wavelength body waves. NACT was used in waveform tomographic study in the late 1990's and first half of the 2000's for whole mantle S velocity structure (Li & Romanowicz 1996; Megnin & Romanowicz 2000) and radial anisotropic structure (Gung et al., 2003; Panning & Romanowicz 2004).

The above S-velocity models suffer from the same limitations as the P-velocity models in terms of data coverage. Su et al. (1994, 1997) and Gu et al. (2001, 2003) conducted "joint inversion" using body wave travel-time data and body wave waveform data. Three-dimensional S-velocity models of the mantle have also been produced using the ISC database (Robertson & Woodhouse 1996).

Most models of mantle S-velocity structure have relied on direct analysis of seismic waveforms in one form or another. Data extracted from seismic waveforms include surface-wave dispersion and structural constraints from the splitting of normal modes, as well as the travel times of a number of different seismic phases such as S, SS, SKS and ScS. Recent mantle S-velocity models that use various combinations

of data extracted from seismic waveforms include those of Masters et al. (2000), Megnin & Romanowicz (2000), Gu et al. (2001, 2003), Kustowski et al. (2008) and Ritsema et al. (1999, 2011). Although the database derived from seismic waveforms is large and becoming larger, the number of observations used to constrain mantle S-velocity variations are still far smaller than the ISC database provides for P-velocity structure. Thus, the S-velocity models tend to have lower resolution than the ISC-based P-velocity models. On the other hand, the use of surface waves and multibounce seismic phases such as SS waves gives a more uniform global coverage of the mantle as well as more information on upper mantle seismic structure. Grand (1997, 2002) inferred a global S-velocity model using such multibounce seismic data.

More recently (in the late 2000s), several groups tried to extract information from observed waveforms. Chen et al. (2007) inverted phase-delay measurements of P and S waves to determine the 3-D structure of the Los Angeles region, using the finite difference method (FDM) to compute synthetic seismograms. Tape et al. (2009, 2010) inverted for crustal structure beneath southern California using the spectral element method (SEM; Komatitsch & Vilotte 1998; Komatitsch et al., 2000) to compute synthetic seismograms. They used waveform data to obtain travel time or phase data for finite frequency kernels (Dahlen & Tromp 1998). Waveform inversion was conducted using a data set consisting primarily of surface waves by Fichtner et al. (2008, 2009, 2010) using SEM synthetics. The UC Berkeley group developed waveform tomography techniques for global S velocity structure and anisotropic structure using SEM to compute synthetic seismograms (Lekić & Romanowicz 2011; French & Romanowicz 2014, 2015).

1.2 Global scale lowermost mantle structure

Previous global-scale tomographic studies (e.g., Masters et al., 2000; Houser et al., 2008; Simmons et al., 2010; Koelemeijer et al., 2016) have revealed large-scale heterogeneity at the base of the mantle, called the degree-2 pattern, with two large low shear velocity provinces (LLSVPs; Fig. 1.1) beneath the Pacific and Africa surrounded by high-velocity regions. Although the high velocity anomalies are interpreted as cold material associated with downward convection of former oceanic plates, the origin of the LLSVPs has been controversial.

Several conceptual models have been developed in recent years to explain the observed LLSVPs. It is dynamically difficult to account for the large low-velocity anomalies beneath Africa and the Pacific with an isochemical mantle, even with models that impose a large-scale pattern of downwelling by employing geologically recent plate velocities as surface boundary conditions (e.g., Bunge et al., 1998; McNamara & Zhong, 2005). In dynamical models that lack a thermochemical component, plumes tend to organize into clustered networks of thin upwellings (plume clusters) that form away from downwelling regions (e.g., Schubert et al., 2004; McNamara & Zhong, 2005). Although current research is assessing whether regions of plume clusters could explain the large, low-velocity anomalies in the lowermost mantle found by seismic tomography (Ritsema et al., 2007), it has been suggested that thermochemical models of mantle convection provide the best explanation for the existence of the LLSVPs. Thermochemical models that attempt to explain the dynamics related to LLSVPs beneath Africa and the Pacific typically fall into two categories. Both invoke a large volume of anomalously dense mantle material; however, they differ in terms of the relative buoyancy and geologic longevity of the chemical anomaly (Garnero et al., 2007). The

detailed seismic structure within and around the margin of the LLSVP are required to elucidate the origin of the LLSVP (i.e., to distinguish between plume clusters and thermochemical piles).

In contrast to LLSVPs, several studies have aimed to establish the correlation between the location of high-velocity anomalies in the Earth's lower mantle inferred by tomographic studies and the location of paleo subduction zones. Several studies are based on a global P-velocity models inferred using travel-time tomography and a 3-D initial model by Amaru (2007) (van der Meer et al., 2010, 2018), while other studies use several (~10) S- (Domeier et al., 2016) and P-velocity models (Shephard et al., 2017). Domeier et al. (2016) showed a global correlation between the location of paleo subduction zones from 10–200 Ma, and slabs in the lower-mantle, as inferred by several previous tomographic models down to at least ~2300 km depth, assuming that slabs sink vertically. This could suggest penetration of slabs deep into the lower mantle on a global scale, although slabs in the lower mantle typically appears as broadened high-velocity anomalies.

Van der Meer et al. (2010, 2018) conducted a more detailed comparison between high-velocity anomalies in the lower mantle and past subduction zones. Van der Meer et al. (2018) classified more than 90 slabs, giving their top and bottom depths, and the ages of the start and end of subduction, relying on previous interpretations and existing geophysical records. Around half of the slabs identified by van der Meer et al. (2018) reside in the lower mantle only. One particularity of their interpretation is that they propose that several of these lower mantle paleoslabs are remnants from past intra-oceanic subduction zones, which are not included in recent plate reconstruction models (Müller et al., 2016). If subducted slabs reach the lowermost mantle, segregation of

subducted mid-ocean ridge basalt (MORB) in the lowermost mantle will be an important mechanism in the long-term thermal and chemical evolution of the mantle and core.

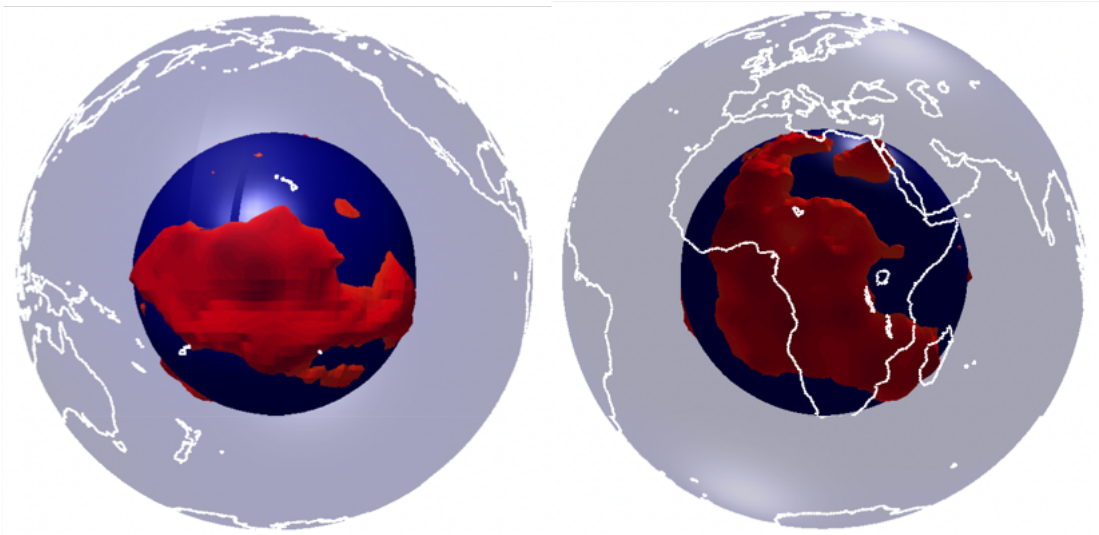

Figure 1.1. Cartoons depicting Pacific (left) and Africa (right) LLSVPs in red. The core is solid blue, while the coastlines are drawn on a transparent gray surface. We plotted the isosurface of δVs=0.5 of the SEMUCB_WM1 model (French & Romanowicz, 2014).

1.3 Anisotropy in the deep Earth

Seismic anisotropy in the Earth's mantle has been considered to be related to mantle flow and deformation of the mantle material. Seismic anisotropy in the Earth's mantle have been extensively investigated. The pioneering work of Raitt (1963) reported azimuthal anisotropy under the Moho in the Mendocino escarpment and Hess (1964) interpreted this reported seismic azimuthal anisotropy as due to large-scale mantle convection that produced alignment of olivine crystals. The emergence of seismic tomography made it possible to map the variations of radial and azimuthal anisotropy. These variations of azimuthal anisotropy turned out to have a regular form, with an indication of the direction of spreading around mid-ocean ridges (Tanimoto & Anderson, 1985; Montagner & Tanimoto, 1990, 1991), while differences in the velocity of vertically polarized Rayleigh waves and transversely polarized Love waves could suggest the location of upwelling or downwelling flow (e.g., Nataf et al., 1984; Montagner, 2002).

1.3.1 Seismic anisotropy in the deep mantle

In contrast to the upper mantle, most of the lower mantle appears to be isotropic, except in the lowermost several hundred km, in the D″ region, where evidence for seismic anisotropy has been proposed since the late 1980s, mostly from shear wave splitting measurements. Shear wave splitting analysis is one of the most commonly used techniques to detect anisotropy in the Earth's deep interior and infer the mantle flow direction (Silver & Chan 1991). The early observations of shear wave splitting attributed to anisotropy in D″ by Vinnik et al. (1989) reported elliptically polarized S_{diff} waves, for raypaths which sample the lowermost mantle in the central Pacific along a direction for which splitting was absent in SKS. Because the absence of the splitting in SKS phase

implied that there was no contamination from upper mantle anisotropy, they suggested that the splitting originated in the lowermost mantle and could be due to the presence of anisotropy in D″. Mitchell & Helmberger (1973) and Lay & Helmberger (1983) observed time shifts between the arrival of ScSH and ScSV, which they attributed to the presence of a high-velocity region at the base of the mantle. Several studies followed in the 1990s, reporting splitting times of up to 10 s in shear waves, such as ScS and S_{diff} that propagate in the lowermost mantle, and interpreted them as suggesting the presence of several percent of VTI (Vertical Transverse Isotropy) in the deep mantle.

Early observations and forward modeling studies on D″ anisotropy mostly relied on data from isolated stations, which made it difficult to constrain the geometry of the anisotropy, due to a lack of sampling of the target regions by waves propagating in different directions (Maupin, 1994). Thus, most studies only reported the differences in SH and SV propagation times, leading to models of apparent VTI. However, evidence for azimuthal anisotropy has been suggested, either from waveform complexity (Garnero et al., 2004a; Maupin et al., 2005) or, when the geometry permitted, from measurements of splitting on raypaths sampling the target region in at least two directions (e.g., Wookey & Kendall, 2008). Regions where this has been possible are central America using S and ScS data from the dense USArray (Nowacki et al., 2010), the northwest Pacific (He & Long, 2011), using ScS data from the F-net in Japan, and Siberia using S and ScS data from CNSN and German Regional Seismic Network (GRSN) (Wookey & Kendall, 2008). Several studies using S_{diff} at the southern border of the African LLSVP, based on data from the Kaapval array, show lateral variations of anisotropy (e.g., Cottaar & Romanowicz, 2013), with strong anisotropy in the fast velocity region outside the LLSVP, increasing towards its border and apparently

disappearing inside the LLSVP. Caution must be taken when interpreting apparent splitting in S_{diff}, due to isotropic heterogeneity potentially affecting SV_{diff} in a significant way (Borgeaud et al., 2016; Komatitsch et al., 2010). However, the strong elliptical shape of the particle motion outside of the African LLSVP (To et al., 2005), where isotropic velocities are relatively fast, contrasting with the linear particle motion for raypaths travelling inside the LLSVP, cannot be accounted for by isotropic heterogeneity.

In order to improve our understanding of the variation and nature of seismic anisotropy in the lowermost mantle, we must be able to make accurate corrections for upper mantle anisotropy. One possible approach is to construct global whole mantle tomographic models of anisotropy. Such an approach is attractive, because a variety of seismic waveforms can be included, in particular fundamental and overtone surface waves, which provide constraints on the anisotropy in the uppermost mantle (Debayle & Ricard, 2013). Combining surface wave data with various body waveforms that sample the entire mantle could provide improved resolution and characterization of deep mantle anisotropy. Thus in the future, it would desirable to follow this approach.

Apparent splitting of shear waves sampling the D″ region could be due to other causes than anisotropy, such as propagation in a complex heterogeneous medium near the boundary between the solid mantle and the fluid outer core (Borgeaud et al., 2016; Nowacki & Wookey, 2016; Parisi et al., 2018). Since shear wave splitting analysis assume that radial and transverse components propagate along the same raypath and have the same sensitivity with respect to each point along the path, careful waveform analysis is therefore necessary before attributing splitting observations to anisotropy.

As discussed above, all shear wave splitting studies measure the travel-time differences between SV and SH arrival times and use this to infer the anisotropic

structure. With the exception of Kawai & Geller (2010), no previous study has quantitatively directly inferred the anisotropic elastic constants within D″. Kawai & Geller (2010) computed the sensitivity of two horizontal (transverse and radial) components of the seismic wave field due to perturbations to the velocity structure in the lower mantle and found that, due to the boundary condition of zero tangential traction at the CMB, resolution of the anisotropy (i.e., of the values of the TI elastic constants L and N) within about one wavelength of the CMB is effectively impossible. Their result shows the limitations of ray theory, which is an infinitely high frequency approximation. However, they successfully conducted simultaneous inversion of a data set of radial and transverse waveforms for multiple sources and receivers and were able to infer the 1-D TI anisotropic S-wave structure beneath the Pacific in the lowermost 400 km of the mantle (except for the depth range 0–100 km above the CMB). They found that the TI elastic constant L is larger than the TI elastic constant N in the depth range of about 200–400 km above the CMB, suggesting that the origin of the Hawaiian hotspot is at the CMB. In section 4.5 of this thesis, we extend their method to 3-D anisotropic S-velocity structure and conduct waveform inversion using the large waveform data from USArray to infer D″ anisotropic structure beneath the northern Pacific.

1.4 Seismic array observation

Publicly available global seismic networks continue to grow, with data from thousands of seismic stations (both temporary and permanent) available for any given earthquake at present. Data centers, such as the Incorporated Research Institutions for Seismology (IRIS), National Research Institute for Earth Science and Disaster Resilience (NIED), Northern California Earthquake Data Center (NCEDC), Geological Survey of Canada (GSC), and Observatories and Research Facilities for European Seismology (ORFEUS) provide freely available digital seismic waveform data in large volume. Such global seismic datasets have played an important role in both forward and inverse studies on determination of Earth's structure. The deployment of high quality modern seismic networks such as USArray carried out in the Earth Scope project gives the opportunity to study the detailed structure in of Earth's lowermost mantle in unprecedented ways with the availability of large volume high quality seismic data. USArray is, for example, composed of more than 700 high quality broadband seismic stations are deployed across the United States of which 400 are deployed in a rolling grid that advances every 2 years (Rost & Garnero, 2004).

New deployment of seismic observation arrays in region which presently have a low density of seismic stations also important. Since the density of seismic stations in Thailand was low compared with neighboring countries (e.g., China and India), we recently deployed a broadband seismic observation array named the Thai Seismic Array (TSAR; Tanaka et al., 2019) starting in January 2016 with the deployment of 2 pilot stations. The array installation was completed with 40 stations in February 2017, and the operation continued until the end of January 2019. Since array observations provide dense and uniform sampling of a particular region of the Earth's interior, it is

desirable to conduct waveform inversion to obtain a high resolution seismic image for that region. In this dissertation, we focus on the D″ region beneath the western Pacific with dataset recorded by TSAR as well as other seismic networks in east Asia and Australia (Chapter 3), and beneath the northern Pacific mostly using USArray data (Chapter 4).

1.5 Waveform inversion

As discussed above, studies of the Earth's internal structure, particularly the fine structure of the upper mantle transition zone and D″, are one of the most important tools for better understanding geodynamic processes. One approach is to analyze data sets consisting of secondary information such as measured P wave first arrival times, phase velocity of surface waves, or eigenfrequencies of modes of free oscillation. The other approach is to conduct direct inversion of the observed waveforms for seismological Earth structure.

Full waveform inversion is a technique to determine the Earth's structure using the observed waveform data themselves (Tarantola 1984), rather than intermediate parameters such as travel times, as the data to be inverted. This technique is widely employed in both exploration and global seismology. The advantages of direct waveform inversion especially for deep Earth structure are: (i) Better resolution, especially for the low velocity anomalies, will be achieved. (ii) Information from overlapping phases can be utilized. (iii) The quantity of information will increase, as waveform inversion fully utilizes all of the information contained in the observed waveform, whereas travel-time tomography uses only part of the available information. Woodhouse & Dziewoski (1984) commented that 'full' waveform inversion for

aspherical Earth model is unfeasible, since it takes a long time to compute partial derivatives and a number of iterations for non-linear inverse problem. However, developments in the 36 years since that paper now make it feasible to conduct waveform inversion.

For the past 30 years the global seismology research group at University of Tokyo has been working on determining 3-D Earth structure by full waveform inversion using observed seismic waveform data. Initial work was based on making accurate computations of the eigenmode of a laterally heterogeneous model and their partial derivatives using the variational method (Tsuboi & Geller, 1987). Hara et al. (1991) then used this method to compute synthetic seismograms and performed iterative linearized waveform inversion for laterally heterogeneous upper mantle structure (for spherical harmonics degree up to 4), using observed waveform data from the IDA network in the period range between 200 and 220 s.

In the course of the study by Hara et al. (1991), they realized that modal summation to compute synthetic seismograms and their partial derivatives was an unnecessary intermediate step, since it could be computed directly by solving a system of linear equations. They called this approach “the Direct Solution Method (DSM)” (Geller et al. 1990; Hara et al. 1991; Geller & Ohminato 1994). Forward modeling computation methods based on the DSM each for spherically symmetric (1-D) isotropic Earth models (Cummins et al. 1994a, b; Takeuchi et al. 1996), for 2-D and 3-D heterogeneous isotropic Earth models in spherical coordinates (Cummins et al. 1997; Takeuchi et al. 2000) and for spherically symmetric transversely isotropic Earth models (Kawai et al. 2006) have been developed.

Geller & Takeuchi (1995) derived a theory to obtain optimally accurate numerical operators by formal estimation and minimizing the error of numerical solutions of the weak form of the elastic equation of motion in the frequency domain. The extension to time domain schemes is given by Geller & Takeuchi (1998), and Takeuchi & Geller (2000) extended this scheme to 2-D and 3-D isotropic Earth models. Using these optimally accurate operators improved the accuracy of synthetic seismograms by about 10–30 times without increasing CPU time (Geller & Takeuchi 1998). Geller et al. (2013a, b) recently reformulated the concept of "optimally accurate operator" and developed a basic concept named the "cell-based optimally accurate method (C-OPT)". Hasegawa et al. (2018) extended this scheme to spherical coordinates. We will compute highly accurate synthetic seismograms using "C-OPT" scheme for 3-D heterogeneous Earth models in the future.

Seismic mantle tomography based on waveform inversion using the DSM for computation of synthetic waveforms was conducted in the early 1990s by our group. Geller & Hara (1993) presented two equivalent algorithms: one is a matrix formulation which is advantageous for the case of an Earth model parameterized in terms of a global basis, and another is a wavefield formulation which is advantageous for the case of an Earth model parameterized in terms of a local basis for iterative linearized waveform inversion for 3-D Earth structure. Hara et al. (1993) then used the DSM to compute synthetic seismograms and their partial derivatives for a laterally heterogeneous Earth model and performed iterative linearized waveform inversion for laterally heterogeneous upper mantle structure, using observed long wavelength (200–400 s) surface wave data from the IDA and GEOSCOPE networks. This efficient algorithm for for computing both synthetics and their partial derivatives makes it feasible to conduct

waveform inversion of surface wave data for 3-D heterogeneous models of the upper mantle (Hara & Geller 2000; Hara 2004). Takeuchi & Kobayashi (2004) conducted waveform inversion of body wave data for whole mantle structure in which linear spline functions rather than the eigenfunctions of the modes of the spherically symmetric model for the vertical dependence of the trial functions were used to compute synthetics and their partial derivatives. More recently, Takeuchi (2007) and Takeuchi (2012) conducted waveform inversion using three-dimensional Born kernels and obtained the three-dimensional SH velocity structure of the whole mantle expanding the laterally heterogeneous structure in spherical harmonics up to angular order 18, SH18CE and SH18CEX model, respectively.

In the past 10 years, there have been new deployments of seismometers (see section 1.4). One is the introduction of broadband array networks (Rost & Garnero 2004). As they are deployed densely (e.g., F-net, Hi-net), they are suitable for determining local structure and local seismic activity. Another is deployment of portable broadband seismic stations such as USArray. As they are deployed temporary, typically for a few years, they are suitable for studies of the structure in particular regions. Kawai & Geller (2010a) reformulated waveform inversion for localized structure, computing partial derivatives, based on the wavefield formulation of Geller & Hara (1993), for 3-D anisotropic Earth structure at particular points in space. The earliest 1-D models based on this formulation was obtained by Kawai et al. (2007a, b). They inverted seismic body-wave waveform data for the vertical dependence of (isotropic) shear velocity structure in the D″ layer beneath Central America (Kawai et al., 2007a), the Arctic (Kawai et al., 2007b) and northern Asia (Kawai et al., 2009), using transverse components of relatively long period broadband waveforms (20–200 s). They showed the existence of high shear

velocity in the upper half of D″ and low shear velocity in the lower half of D″ beneath these regions.

After these studies our group conducted waveform inversion for localized 1-D isotropic shear velocity structure in the lowermost mantle for various region. Konishi et al. (2009) studied the fine structure of the edge of the large low shear velocity province (LLSVP) beneath the western Pacific, and found a low S-velocity zone in the depth range from about 2550-2750 km, with the greatest decrease (relative to Preliminary Reference Earth Model; PREM (Dziewonski & Anderson, 1981)) of about 0.2 km/s in the zone from about 200 to 250 km above the CMB. They called this S-velocity structure an "S-shaped model". Kawai & Geller (2010a) also studied S-velocity structure in the lowermost mantle beneath the Central Pacific using the transverse component of broadband waveforms for the period range 8–200 s. They found 1.0 percent to 1.5 percent velocity decreases and velocity increases in the zones from 400 to 500 km and from 300 to 400 km above the CMB, respectively. In addition, they found 0.5 percent to 1.0 percent velocity increases and decreases in the zones from 100 to 200 km and from 0 to 100 km above the CMB, respectively.

Kawai & Geller (2010b) examined S-velocity structure in the lowermost mantle beneath the Hawaiian hotspot, which is located away from the center of the Pacific LLSVP and to the northwest of the region studied by Kawai & Geller (2010a). They discussed the detailed difference in S-velocity structure obtained by Konishi et al. (2009), Kawai & Geller (2010a), and Kawai & Geller (2010b).

We can apply localized waveform inversion method (Geller & Hara 1993; Kawai et al., 2010a) not only for 1-D isotropic elastic parameter, but also for 1-D anisotropic and anelastic structure. Kawai & Geller (2010c) inverted the horizontal two

components (transverse and radial) of observed seismic waveforms to determine the radial profile of anisotropic (transversely isotropic) shear wave velocity in the lowermost mantle beneath the Pacific, and found that the TI elastic constant L is larger than the TI elastic constant N in the depth range from about 200–400 km above the CMB. Since anisotropic structure is considered to be due to the flow and deformation of the mantle material, it is desired to directly constrain the elastic constants in an anisotropic in order to understand the mantle dynamics. The obtained anisotropic structure in Kawai & Geller (2010c) was interpreted as evidence for vertical flow due to thermal buoyancy, which might be related to the origin of the Hawaiian hotspot. Fuji et al. (2010) developed a methodology for waveform inversion of body-wave waveform data for 1-D elastic and anelastic structure and applied it to the upper mantle and mantle transition zone (MTZ) beneath the northwestern Pacific. More recently, Konishi et al. (2016) applied this method to the lowermost mantle beneath the western Pacific.

Today we can analyze large amount of waveform data provided by various dense seismic array networks due to great progress of computational technology and methods. Our group has developed methods for waveform inversion for three-dimensional (3-D) localized structure (Kawai et al., 2014) and has applied these methods to infer the 3-D S-velocity structure in D″ beneath Central America (Kawai et al., 2014), beneath the western Pacific (Konishi et al., 2014), beneath the northern Pacific (Suzuki et al., 2016), and beneath Central America (Borgeaud et al., 2017). Suzuki et al. (2016) and Borgeaud et al. (2017) studies confirmed the presence of strong high-velocity anomalies in the D″ region beneath two long-lived subduction zones (corresponding to paleo subducted slabs), but also the presence of strong low-velocity anomalies just above the CMB extending vertically around the high-velocity anomalies, resulting in the

inference of a smaller-scale convection pattern than had been possible in previous global studies. Recently, Borgeaud et al. (2019) extended and conducted this method to infer the 3-D S-velocity structure in mantle transition zone (MTZ) beneath the Central America and the Gulf of Mexico. They found complex subduction modality of the Cocos slab, possibly due to the thermal structure of the Cocos slab.

1.6 This study

In this study, in order to improve our understanding of the thermal and chemical evolution of the Earth, we image the 3-D S-velocity structure in the D″ region beneath the western and northern Pacific with higher resolution than in previous tomographic models. These two regions are important in investigating the history of the solid Earth, since these are possible places where chemical differentiation such as basalt segregation from subducted slab took place in the past or will take place in the future.

In Chapter 3, we assemble waveforms recorded by TSAR and Australia stations as well as other temporary and permanent networks around Southeast Asia, allowing us to examine the detailed structure inside and around the western margin of the Pacific LLSVP with better azimuthal coverage than previous regional studies. We then conducted localized waveform inversion for the high-resolution 3-D S-velocity structure around the margin of the Pacific LLSVP in D″.

In Chapter 4, we first conduct waveform inversion with a large waveform dataset of the transverse component from the full deployment of the USArray in order to image the high-resolution 3-D isotropic shear wave velocity structure of the D″ region beneath northern Pacific. We also conduct for the first time waveform inversion

using not only transverse component but also radial component for 3-D anisotropic (vertically transverse isotropy; TI) structure within the D″ region, giving an insight into the flow direction (vertical or horizontal) in the lowermost mantle.

We discuss the implications of the inferred models of the D″ region beneath the western and northern Pacific to understand the thermal and chemical evolution of the Earth based on previous geodynamics studies (Chapter 5). We discuss in particular, (i) possible chemical anomalies such as Fe or Al at the western margin of the Pacific LLSVP based on our inferred small-scale low-Vs structure, and (ii) possible ongoing chemical differentiation such as segregation of the basalt in oceanic crustal material from depleted material in D″ beneath the northern Pacific subduction zone based on our inferred isotropic and anisotropic structure in D″.

Chapter 2 Methods

2.1 Inverse problem

The synthetic wavefield $\boldsymbol{u}_{syn}(\boldsymbol{r})$ at a seismic station located at a point $\boldsymbol{r}$ at the Earth's surface is a nonlinear functional of the Earth's structure model $\boldsymbol{m}$

$$\boldsymbol{u}_{syn}(\boldsymbol{r}) = \boldsymbol{f}[\boldsymbol{m}](\boldsymbol{r}). \tag{1}$$

In general, the recorded wavefield $\boldsymbol{u}_{obs}(\boldsymbol{r})$ differs from the synthetic wavefield $\boldsymbol{u}_{syn}(\boldsymbol{r})$ by a quantity called the waveform residual:

$$\boldsymbol{r} = \boldsymbol{u}_{obs} - \boldsymbol{u}_{syn}. \tag{2}$$

Here, we assume that we have a large number of seismic records truncated around the seismic phases used for the inversion for a total of N time windows. The residual $\boldsymbol{r}$ is built by juxtaposition of the N time-windows. If the functional $\boldsymbol{f}$ in eq. (1) is not too nonlinear, and if we already have a good guess of the initial Earth's model $\boldsymbol{m}^0$, eq. (2) can be linearized around $\boldsymbol{m}^0$, as follows:

$$\begin{aligned} \boldsymbol{r} = \boldsymbol{u}_{obs} - \boldsymbol{f}[\boldsymbol{m}^0 + \delta\boldsymbol{m}](\boldsymbol{r}) &\approx \boldsymbol{u}_{obs} - \boldsymbol{f}[\boldsymbol{m}^0](\boldsymbol{r}) - \frac{\delta \boldsymbol{f}}{\delta \boldsymbol{m}}[\boldsymbol{m}^0](\boldsymbol{r})\delta\boldsymbol{m} \\ \Leftrightarrow \boldsymbol{r} &\approx \delta\boldsymbol{d} - \frac{\delta \boldsymbol{f}}{\delta \boldsymbol{m}}[\boldsymbol{m}^0](\boldsymbol{r})\delta\boldsymbol{m}, \end{aligned} \tag{3}$$

where $\delta\boldsymbol{m}$ is the vector of perturbations from the initial model $\boldsymbol{m}^0$, and $\delta\boldsymbol{d} = \boldsymbol{u}_{obs} - \boldsymbol{f}[\boldsymbol{m}^0](\boldsymbol{r})$ is the waveform residual for the initial model. The inverse problem seeks to find $\delta\boldsymbol{m}$ so that $\boldsymbol{r} = 0$. In practice, the perturbation for Earth's model $\delta\boldsymbol{m}$ is developed using a finite basis of M elements (constant-velocity blocks in this dissertation), and the residual $\delta\boldsymbol{d}$ is discretized by sampling the waveforms with a sampling frequency of 1 Hz, and contains NK points, where $K \approx 80$ represents the average number of points in a time-window for dataset used in this dissertation. The discretized version of eq. (3) for $\boldsymbol{r} = 0$ is given as follows (assuming a strict equality):

$$\boldsymbol{A}\delta\boldsymbol{m} = \delta\boldsymbol{d}, \tag{4}$$

where $\boldsymbol{A}$ is called the partial derivative kernel

$$A_{ij} = \frac{\delta f_i}{\delta m_j}. \tag{5}$$

If the inverse problem is well posed, we have $M \ll NK$, i.e., the number of model parameters is much smaller than the number of data points. This means that eq. (4) does not have a solution, and the best we can do is to minimize $\|\boldsymbol{r}\|^2$ as follows:

$$\|\boldsymbol{r}\|^2 = (\boldsymbol{A}\delta\boldsymbol{m} - \delta\boldsymbol{d})^T\boldsymbol{W}(\boldsymbol{A}\delta\boldsymbol{m} - \delta\boldsymbol{d}), \tag{6}$$

where we introduced the (diagonal) data weighting matrix $\boldsymbol{W}$, used to roughly equalize the contribution of each record, and defined as follows:

$$W_{ij} = \delta_{ij}\frac{1}{\max\limits_{k\in\{T_i\}}(\boldsymbol{u}_{obs})_k}, \tag{7}$$

where $\{T_i\}$ is the set of indices of data points that are contained in the time-window to which data point i belongs to. For the case of the D″ layer, we also weight the data to equalize the uneven azimuthal distribution of records (see sections 3.2 and 4.2 for details). Setting the gradient of eq. (6) to zero leads to the least-square equation that defines the inverse problem as follows:

$$\boldsymbol{A}^T\boldsymbol{W}\boldsymbol{A}\delta\boldsymbol{m} = \boldsymbol{A}^T\boldsymbol{W}\delta\boldsymbol{d}. \tag{8}$$

In this dissertation, the synthetics (eq. (1)) and partial derivatives (eq. (5)) are computed for initial 1-D models (PREM) using the DSM (Kawai et al., 2006).

2.1.1 Weighting factor

The distribution of epicentral distances and azimuths of the records in our dataset is shown in Figs. 3.2, 4.2. The distribution of epicentral distances and azimuths is not homogeneous. We remedy this to the extent possible by weighting the

records to homogenize the epicentral distance and azimuth histograms. We compute weighting factors for each bin of the two histograms so that the variance is minimized

$$\sum_{i=1}^{N} \left(k_i - \overline{k}\right)^2 + \lambda(k_i - 1)^2. \tag{9}$$

2.1.2 Conjugate gradient

We solve eq. (8) using a truncated conjugate gradient method in which we truncate the expansion at the n^{th} conjugate gradient (CG) vector (see Kawai et al., 2014), with n chosen to minimize a modified version of the Akaike Information Criterion (Akaike, 1977).

The conjugate gradient method is an iterative method to solve a system of linear equations defined by a positive definite matrix, which is the case of the inverse problem eq. (8). For simplicity, we rewrite eq. (8) as follows:

$$\boldsymbol{A}^T\boldsymbol{A}\boldsymbol{x} = \boldsymbol{A}^T\boldsymbol{b}, \tag{10}$$

where $\boldsymbol{A}^T\boldsymbol{A}$ is a M×M matrix. The conjugate gradient method consists in finding the solution to eq. (10) iteratively using descent directions given by vectors $\boldsymbol{p}_i$ mutually conjugate to each other, which is the case if

$$\boldsymbol{p}_i^T\boldsymbol{A}^T\boldsymbol{A}\boldsymbol{p}_j^T = 0, \forall i, j \in \{1, 2, .., M\}. \tag{11}$$

The $\{\boldsymbol{p}_i\}$ form a base of $\mathbb{R}^M$, so that the solution $\boldsymbol{x}$ to eq. (10) can be written as a linear combination using this basis. The method starts with an initial vector $\boldsymbol{p}_0$ given by the gradient eq. (10), assuming that the initial solution $\boldsymbol{x}_0 = 0$,

$$\boldsymbol{p}_0 = \boldsymbol{A}^T\boldsymbol{b}, \tag{12}$$

and iterates over $k = 0, 1, .., N \leq M$, defining the next conjugate gradient vector $\boldsymbol{p}_k$ as close as possible to the residual $\boldsymbol{r}_k$

$$\boldsymbol{r}_k = \boldsymbol{A}^T\boldsymbol{b} - \boldsymbol{A}^T\boldsymbol{A}\boldsymbol{x}_k, \tag{13}$$

$$\boldsymbol{p}_k = \boldsymbol{r}_k - \sum_{i<k} \frac{\boldsymbol{p}_i^T \mathbf{A}^{\mathrm{T}} \boldsymbol{A}\boldsymbol{r}_k}{\boldsymbol{p}_i^T \mathbf{A}^{\mathrm{T}} \boldsymbol{A}\boldsymbol{p}_i} \boldsymbol{p}_i. \tag{14}$$

The solution at step $k+1$ is then given by

$$\boldsymbol{x}_{k+1} = \boldsymbol{x}_k + \alpha_k \boldsymbol{p}_k, \tag{15}$$

where

$$\alpha_k = \frac{\boldsymbol{p}_k^T \boldsymbol{r}_k}{\boldsymbol{p}_k^T \boldsymbol{A}^T \boldsymbol{A}\boldsymbol{p}_k}. \tag{16}$$

We note that in eqs. (13), (14), and (16), we do not have to compute the matrix multiplication $\boldsymbol{A}^T\boldsymbol{A}$, but just the matrix-vector products $\boldsymbol{A}\boldsymbol{x}_k$, $\boldsymbol{A}\boldsymbol{p}_i$, and $\boldsymbol{A}\boldsymbol{r}_k$. Hence, the conjugate gradient method avoids the computation of $\boldsymbol{A}^T\boldsymbol{A}$, which is computationally intensive when the number of parameters becomes large. The models inferred in this dissertation are for $n = 6$. A small number of vectors minimizes the solution error and avoids overfitting the data.

2.1.3 Variance and AIC

For the regular (without damping) inverse problem eq. (8) the variance reduction (labeled VR) is defined as follows:

$$\begin{aligned} \text{VR (percent)} &= \frac{|\boldsymbol{s}-\boldsymbol{u}|^2}{|\boldsymbol{u}|^2} \cdot 100 = \frac{|\boldsymbol{A}\delta\boldsymbol{m} - \delta\boldsymbol{d}|^2}{|\boldsymbol{u}|^2} \cdot 100 \\ &= (\delta\boldsymbol{m}^T\boldsymbol{A}^T\boldsymbol{A}\delta\boldsymbol{m} + 2\delta\boldsymbol{m}^T\boldsymbol{A}^T\delta\boldsymbol{d} - |\delta\boldsymbol{d}|^2) \cdot 100. \end{aligned} \tag{17}$$

Using this definition, the VR for the data is 100 percent.

As mentioned in section 2.1.1, the conjugate gradient method used to solve the inverse problem is truncated to the first n conjugate gradient vectors based on a modified version of the AIC criterion (Akaike, 1977). The (modified) AIC_n^{α} for the

first n CG vectors and the empirical redundancy parameter α is given as follows:

$$AIC_n^{\alpha} = N^{\alpha} ln(2\pi) + N^{\alpha} ln(VR_n) + N^{\alpha} + 2(n+1), \tag{18}$$

with

$$N^{\alpha} = \frac{N}{\alpha} = \frac{1}{\alpha}\frac{T_{min}}{2} \cdot (\text{Number of data points at 1Hz sampling}), \tag{19}$$

where N is the minimum number of sampling points to represent the data vector $\delta \boldsymbol{d}$ (i.e., two points per minimum period).

2.2 Data correction

It is well known from previous tomographic studies that the shallow structure (~0–300 km depth) is strongly heterogeneous, with S-velocity anomalies that can reach ~10 percent. For such strong velocity anomalies, it is not possible to approximate the wavefield as a linear perturbation to the wavefield for the initial 1-D model.

In this dissertation, we conduct localized waveform inversion for the 3-D S-velocity structure of the D″ region (between 0–400 km above the CMB) without modeling the part of the Earth above the target region. It is therefore necessary to correct the data to account for the effect of the 3-D structure outside (i.e., above) D″. We use the autopick method developed by Fuji et al. (2010), which uses the S phase as a reference phase to correct the data for the travel-time residual due to the structure close to the source and receiver (Fig. 2.1).

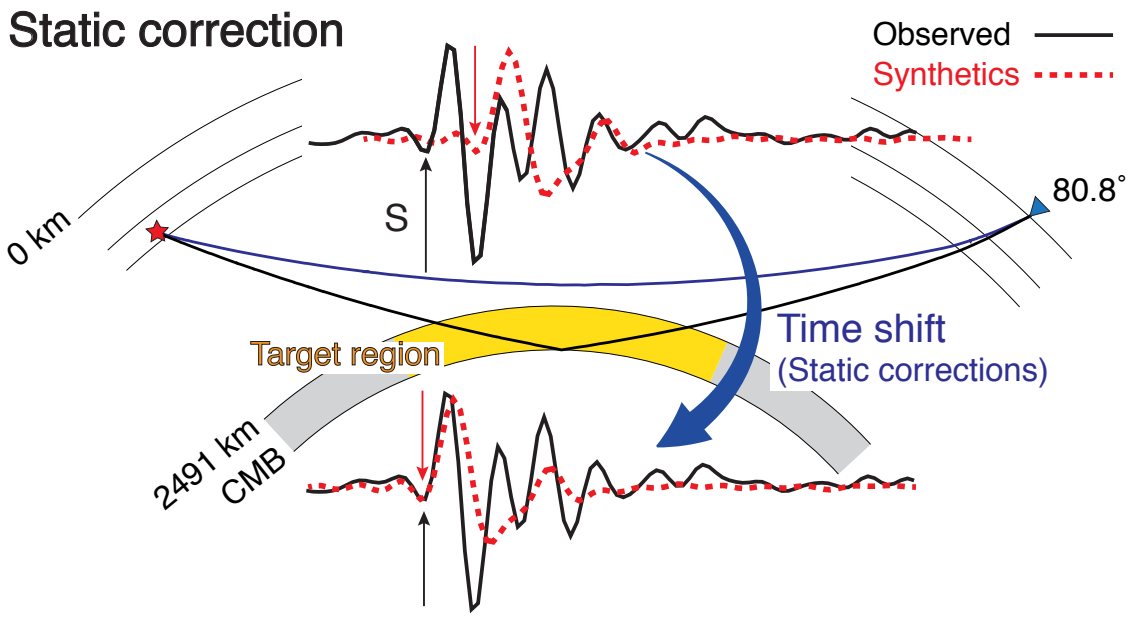

Figure 2.1. Corrections for the shallow structure for the case of D″. The direct S-wave (red line) turns above the target region in D″ (shown in yellow), and is used as a reference phase to correct the data for the 3-D heterogeneities near the source (red star) and the station (blue inversed triangle).

2.3 Validation of inferred model

As for any kind of seismic tomography, it is necessary to validate the models obtained using waveform inversion to check that the resolution of the partial derivative kernel is enough to resolve the smallest scale 3-D variations in the inferred model, and to check the robustness of inferred models with respect to possible source of errors due to 1) data errors, and 2) unmodeled properties (e.g., unmodeled part of the Earth in the case of local tomography).

2.3.1 Resolution test

The (linear) checkerboard test is the most widespread test to check the resolving power of the kernel. It is performed by computing approximate input synthetics $\boldsymbol{s^c}$ for a 3-D checkerboard pattern of alternating high- and low-velocity anomalies by multiplying the kernel with the checkerboard pattern anomalies as in follows:

$$\boldsymbol{s}^c = \boldsymbol{s}^0 + \boldsymbol{A}\delta\boldsymbol{m}^c \Rightarrow \delta\boldsymbol{d} = \boldsymbol{s}^c - \boldsymbol{s}^0 = \boldsymbol{A}\delta\boldsymbol{m}^c, \tag{20}$$

and then performing an inversion using $\boldsymbol{s^c}$ as input data. Substituting eq. (20) in the inverse problem eq. (8) yields eq. (20).

The checkerboard test has been criticized by some authors, mostly because it does not check the nonlinearity of eq. (5) that arises because of the relatively strong deviations between the initial model and the inferred 3-D model (Rawlinson & Spakman, 2016). Localized waveform inversion method can resolve lateral heterogeneities from waveforms propagating only in a relatively narrow range of azimuths because of the large amount of information contained in the waveforms, which are linearly independent. Since our dataset includes waveforms whose incidence angles differ from one another and whose most sensitive point, that is, the turning point, is

different for each record, we can resolve laterally heterogeneous structures.

Nonlinearity can, however, be checked by computing exact synthetics for the input checkerboard pattern using a 3-D wave propagation code such as SPECFEM3D_GLOBE (Komatitsch & Tromp, 2002a, b; Komatitsch et al., 2015). We call this test "nonlinear checkerboard test". Although the linear checkerboard test is widely used in seismic tomography, its nonlinear version is not common. One of the reasons why nonlinear checkerboard tests are usually not performed is that they require the computation of exact synthetics for the 3-D structure, which is computationally intensive. Also, for tomographic studies that perform several iterations for the actual inversion (French & Romanowicz, 2014), a similar number of iterations would have to be performed for the nonlinear checkerboard test, which means that the nonlinear checkerboard test has the same computational cost as the actual inversion. We perform the nonlinear checkerboard test for the case of the D″ layers (sections 3.4, 4.3, and 4.5), and show that the linear approximation is reasonable for these two cases (for perturbations of strength 2.5 percent).

The third and last type of resolution test performed in this dissertation is a point-spread function test. The point-spread function test is similar to the checkerboard test, with the only difference that the input synthetics are computed for a point anomaly (i.e., only one voxel is perturbed) rather than for checkerboard pattern anomalies. This test allows to quantify the (nominal) amount of spreading (or smearing) from a point anomaly to other voxels in the model, and is equivalent to computing a particular column of the resolution matrix, defined as follows:

$$\delta \boldsymbol{m}^{est} = \boldsymbol{R}\delta \boldsymbol{m}^{true}, \tag{21}$$

where $\delta \boldsymbol{m}^{est}$ and $\delta \boldsymbol{m}^{true}$ are the inferred, and actual model perturbations, respectively.

Indeed, for instance if the point anomaly corresponds to the j^{th} voxel in the vector of model parameters, then $\delta \boldsymbol{m}^{true} = \hat{\boldsymbol{e}}_{\boldsymbol{j}}$, which implies that $\delta \boldsymbol{m}^{est} = \boldsymbol{R}\hat{\boldsymbol{e}}_{\boldsymbol{j}} = \boldsymbol{R}_j$, the j^{th} column of $\boldsymbol{R}$.

We note that, as discussed by Rawlinson & Spakman (2016), these kind of resolution tests obtained by solving the inverse problem for a synthetic input are currently widely used, even though current computers allow for the computation of the full resolution matrix for most of the current tomographic models. However, even the full resolution matrix does not tell us about the "actual" resolution of the tomographic inversion, because the actual inverse problem is non-linear (Romanowicz, 1991). Resolution tests using synthetic input can, on the other hand, test the validity of linearizing the inverse problem if the synthetic input is computed by solving the (non-linear) forward problem (as discussed above).

2.3.2 Robustness test

Even when the resolution is good, artifacts in the inferred model can arise because of errors in the data (e.g., noise, misorientation of the seismometer), or in unmodeled structure or source parameters (e.g., hypocenter, moment tensor, source-time function). In this dissertation, we test the robustness of inferred models for errors in the unmodeled structure above the target region (see section 3.3), which we believe is the major source of possible artifacts in the inferred models. We do not check the errors in the model due to possibly inaccurate source parameters. However, a recent study showed that waveform inversion for the structure of D″ is most likely not so sensitive to errors in the source parameters (Yamaya et al., 2018), as long as the minimum period used in the inversion is larger, or comparable to the duration of the source-time function of the

earthquakes used (i.e., that only earthquake with relatively small magnitude are used), which is the case for this work.

The robustness tests we performed are described in detail in sections 3.4, 4.3, and 4.5, so that we will only enumerate them here. We tested: 1) the orthogonality between partial derivatives in the target region and partial derivatives near the sources, 2) the changes in the model when inverting with 50 percent of the data randomly picked among the full dataset (jackknife test).

2.3.3 Improvement window

We introduce the 'improvement window' to evaluate the improvement of synthetic waveform fitting to observed record. We define the 'improvement window' as 20 s before to 30 s later from the expected ScS arrival for initial model, PREM. We compute the variance reduction for this improvement window and show in the Tables 3.1, 3.2, 4.1, and 4.2. We also show the examples of waveform fitting improvement (observed, synthetic for initial model, and synthetic for final model) in Fig. 2.2. As relatively long-period (from 12.5 s or 20 s to 200 s) seismograms at epicentral distances around 90˚ are used in this study, it is difficult to identify phases such as S, ScS and other phases associated with complex structure in the lowermost mantle. Note that as the waveform records shown here are only a small portion of our data set, the fit for individual waveforms is not particularly meaningful. However, the fit of the synthetics for the final model (CG6) to the observed data is reasonably good for every epicentral distance range.

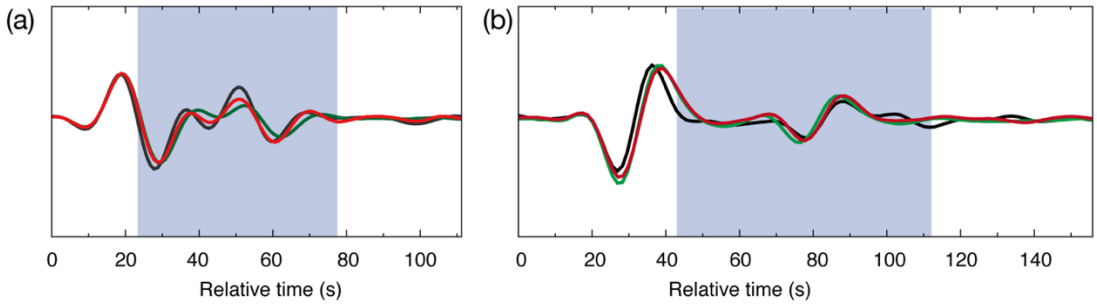

Figure 2.2 Examples of waveform improvement for event stacked waveforms. The traces are in period range (a) 20–200 s and (b) 12.5–200 s stacked in epicentral distance range 74.5˚<Δ≤75.5˚ for event (a) #382 and (b) #305 in Table B1, respectively (the time-shifts used in the inversion are applied to the observed data). Observed traces are shown in black. Synthetic waveforms for the initial model PREM (green), and final model (red). Blue shaded timewindows are 'improvement window', which is 20 s before and 30 s late from expected ScS arrival. As shown in Tables 3.1 and 3.2, the variance reductions for improvement window of both inversion (12.5 s and 20 s) are 34.5 and 36.2 percent, respectively.

Chapter 3 The isotropic 3-D S-velocity structure in D″ beneath the western Pacific

3.1 Introduction

The lowermost several hundred kilometers of the Earth's mantle immediately above the core-mantle boundary (CMB), called the D″ region, is the thermal boundary layer (TBL) of mantle convection; the D″ region is thought to be both thermally and compositionally heterogeneous. Previous global-scale tomographic studies (e.g., Ritsema et al., 2011; French & Romanowicz, 2014; Bozdağ et al., 2016) have revealed two separated large-scale low shear-velocity provinces at the CMB beneath the Pacific and Africa (LLSVPs; e.g., Garnero & McNamara, 2008; Garnero et al., 2016) surrounded by high-velocity regions that are interpreted as cold material associated with downward convection of former oceanic plates (e.g., Domeier et al., 2016; Shephard et al., 2017). Although the LLSVPs occupy ~30 percent of the area of the CMB, their origin and composition have been controversial (Garnero et al., 2016). In order to better understand the thermal and chemical evolution of the Earth it is therefore essential to investigate the fine seismic velocity structure of LLSVPs.

Several geodynamic simulations suggest that the LLSVPs represent small-scale clusters of (relatively chemically homogeneous) thermal plumes seen as continuous structure due to a lack of resolution of seismic tomography (e.g., Bunge et al., 1998; Schubert et al., 2004; Schuberth et al., 2009; Davies et al., 2012). On the other hand, thermochemical effects, such as enrichment in dense material including iron as well as incompatible elements, were suggested to produce large-scale low-velocity anomalies associated with large chemically distinct piles which are also considered to be a

primordial geochemical reservoir (e.g., Bull et al., 2009; Zhang et al., 2010; Li et al., 2014). The former and latter models are called ‘plume clusters’ and ‘thermo-chemical piles,’ respectively. High resolution imaging of the structure inside and at the edge of the LLSVP can contribute to better understanding of whether the low-velocity anomaly is due to thermal clustering or thermochemical piles (Davies et al., 2012).

Due to the relatively favorable locations of seismic sources and receivers, D″ beneath the western Pacific is one of the most suitable regions for inferring the detailed seismic structure within and at the edge of the LLSVP. However, the detailed seismic velocity structure in D″ beneath the western Pacific remains controversial, because of the limitations of previous imaging methods and data coverage. For example, the location of the western boundary of the LLSVP differs from model to model (see Fig. 3.1a).

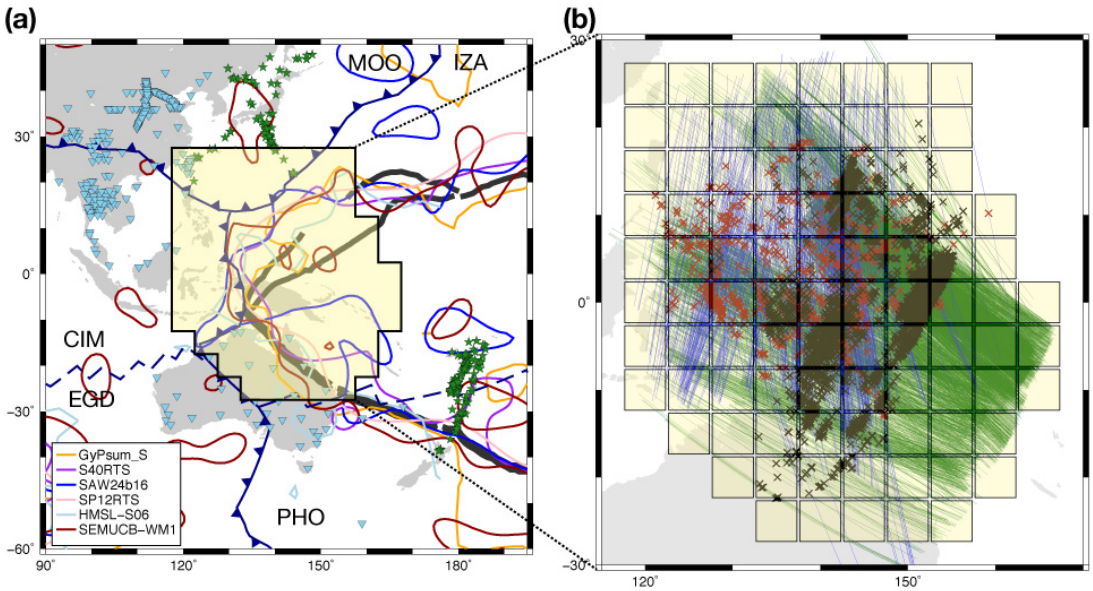

Figure 3.1 (a) Event–receiver geometry for this study. Light-blue inverted triangles and green stars show the locations of the stations and the earthquake sources used in this study, respectively. Six curves (see legend at bottom left) denote the boundaries of the LLSVP for each model: Simmons et al. (2010) for the GyPsum model; Ritsema et al. (2011) for S40RTS; Mégnin & Romanowicz (2000) for SAW24b16; Koelemeijer et al. (2015) for SP12RTS; Houser et al. (2006) for HMSL-S06; French & Romanowicz (2014) for SEMUCB-WM1), where the LLSVPs are assumed to correspond to 30 percent of the CMB area as shown in Garnero et al. (2016). Dark-blue saw-toothed and dashed lines denote subduction zones and mid-ocean ridges 200 Ma on the surface, respectively (Young et al., 2019). Abbreviations: CIM, Cimmerian terranes; EGD, East Gondwana; IZA, Izanagi plate; MOO, Mongol-Okhotsk Ocean; PHO, Phoenix Plate. (b) Raypath coverage in the study area. Waveforms from 545 deep- and intermediate-focus earthquakes beneath Tonga-Fiji and in and around Japan (green stars in (a)) recorded at stations of the TSAR, AU, and other seismic networks (see Supplemental text; light-blue inverted triangles in (a)) provide dense raypath coverage of the target region in the depth range from 0 to 400 km above the CMB. Yellow squares denote the locations of voxels for the parameterization. Green (E–W dataset) and blue (N–S dataset) lines show ScS raypaths that sample the target region, and black (E–W dataset) and brown (N–S dataset) crosses show ScS bounce points at the CMB.

In general, short-wavelength low-velocity anomalies are difficult to image with travel-time tomography, because low-velocity anomalies have only a small effect on travel times, due to wavefront healing effects (Nolet & Dahlen, 2000). Previous studies using both P- and S-waves reported that both amplitude effects such as focusing/defocusing due to finite-frequency and waveform complexity due to multi-pathing, implying the existence of laterally heterogeneous low-velocity structure in our study region (He et al., 2006; Sun et al., 2009; Tanaka et al., 2009). In order to better image the seismic structure in D″ beneath the western Pacific, it is necessary to apply a method which can take into account finite frequency effects, using a dataset of broadband seismic waveforms with wide azimuthal and epicentral distance coverage.

In this study we image the structure using waveform inversion, which is able to make full use of all the information in waveforms, such as amplitudes and complex interacting phases, which is difficult to handle using either travel-time tomography or waveform forward modeling. Our group recently applied localized waveform inversion techniques (Kawai et al., 2014) to much larger datasets to invert for the 3-D S-velocity structure in D″ beneath the northern Pacific (Suzuki et al., 2016) and Central America (Borgeaud et al., 2017) using relatively shorter period data (up to 12.5 s period), and in and around the mantle transition zone beneath Central America (Borgeaud et al., 2019), with high resolution (150-250 km laterally; ~50 km vertically) for both low- and high-velocity anomalies.

3.2 Data and Methods

In order to improve data coverage in D″ beneath the western Pacific we recently deployed a seismic array of 40 portable broadband stations throughout Thailand (Thai Seismic Array—TSAR; Tanaka et al., 2019), which operated from late 2016 to early 2019. The Australian National Seismograph Network (AU) also provides excellent quality waveform data which sample our target region in the North-South direction. We combined waveforms recorded by TSAR and AU stations as well as other temporary and permanent networks around Southeast Asia, allowing us to examine a wider region of the western margin of the Pacific LLSVP with better azimuthal coverage than previous regional studies. Our dataset consists of ~11,000 transverse component waveforms of ground velocity recorded at epicentral distances $68^\circ<\Delta<101^\circ$ from 545 deep- and intermediate-focus earthquakes that occurred around Japan and Tonga-Fiji in the period from 2002 to 2017 (see Table B1 for details). The number of waveforms for earthquakes in and around Japan, recorded by broadband seismic stations in Australia and the South Pacific is ~3,100 records; the rays propagate approximately north to south (hereafter referred to as N–S dataset). The number of waveforms for earthquakes around Vanuatu and Fiji-Tonga Islands and stations in Thailand, Vietnam, Myanmar, Malaysia, and South China is ~8,000 records, whose paths are approximately east to west (hereafter, E–W dataset). We correct the sensor mis-orientation following Yu et al. (2017), based on the minimization of the P-wave energy in the transverse component. We conduct localized 3-D waveform inversion using transverse component records which include S, ScS, and other phases between them in the passband 12.5–200 s. We also invert data in the passband 20–200 s to see whether or not there is significant frequency dependence. Before inversion we weight the data to homogenize the distribution of distances and

azimuths (see section 2.1.1 and Fig. 3.2).

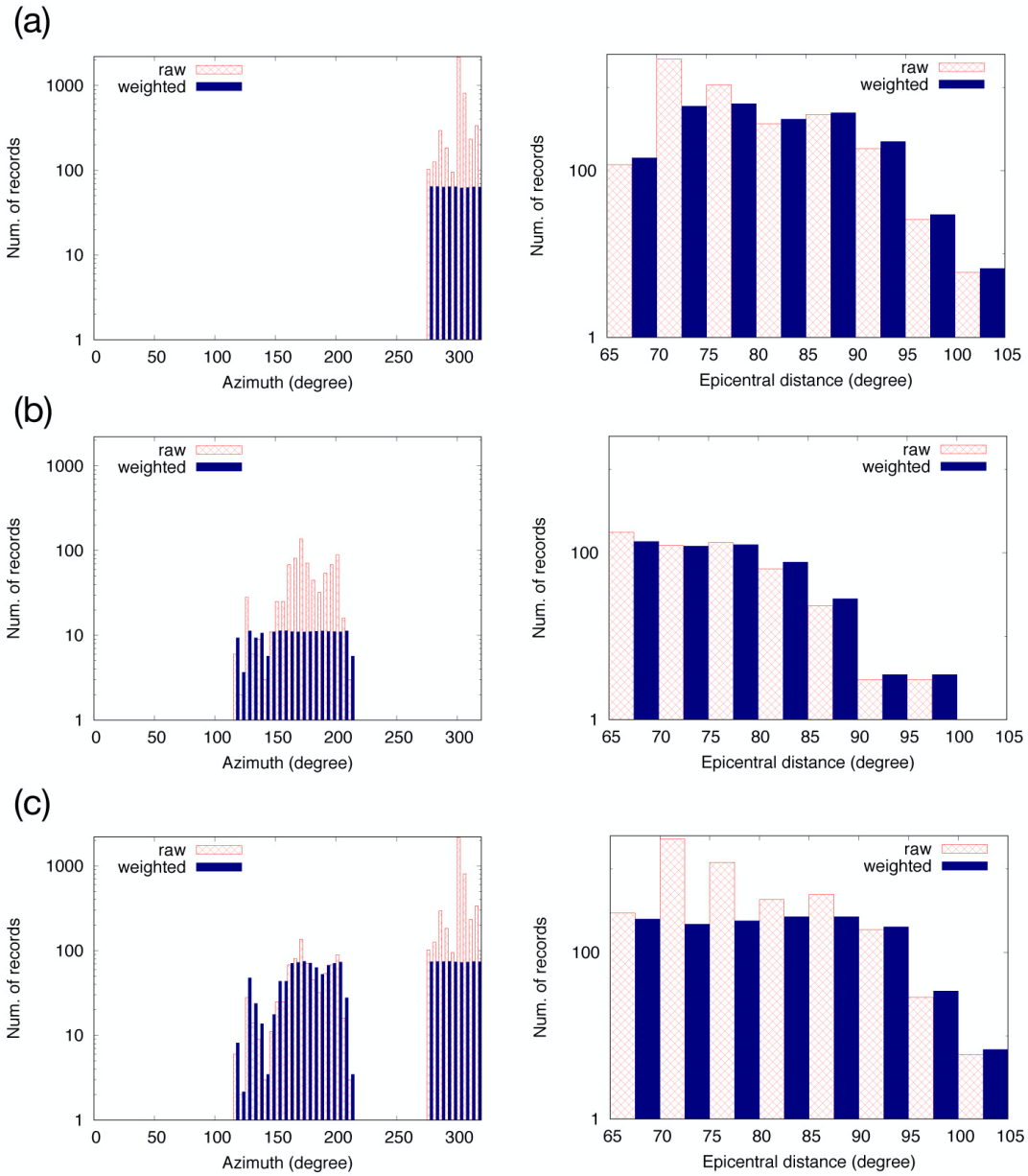

Figure 3.2 Distributions of azimuths (left) and epicentral distances (right) for the records used in the inversion. The original distribution is shown in red, while the weighted distribution is shown in blue. The records are weighted to homogenize the distribution of azimuths and epicentral distances (see section 2.1.1). (a) E-W dataset, (b) N-S dataset and (c) complete dataset used in this study.

3.3 Results

3-D S-velocity structure at the western margin of the Pacific LLSVP

Map views of the S-velocity model obtained by our inversion using data in the period range between 12.5 and 200 s are shown in Fig. 3.3(a). The final model achieved more than 30 percent variance reduction in the 'improvement window' (see section 2.3.3) which is the part of the seismogram that is most sensitive to the structure in D″ (Tables 3.1 and 3.2). We note the following key features. (i) There are significant (up to ~3.5 percent) high-velocity anomalies beneath the Philippine Sea that extend vertically from the CMB to 400 km above the CMB (marked by blue arrows in each panel), whose location is generally consistent with that of the past Izanagi-plate boundaries at the ages shown in each panel (Young et al., 2019). (ii) There are small-scale low-Vs anomalies with a diameter of ~300 km (up to ~3.5 percent slower than PREM) immediately above the CMB (Fig. 3.3). (iii) There is a vertically continuous (CMB to at least 400 km above the CMB) low-velocity structure above the low-velocity anomalies at the CMB (Fig. 3.3).

Model	Variance (percent)	Variance for 'improvement window'	AIC (α=400)
PREM	100.7		—
PREM with time shift	91.3	91.9	3763.8
CG6	88.3	54.4	3727.0

Table 3.1 Variance and Akaike information criterion (AIC) value for each model of the inversion using data in the period range between 12.5 and 200 s. Variance of the synthetics for PREM, PREM with time-shifts with static corrections, and our final model with six conjugate gradient vectors (CG6; see Fig. 3.3a). CG6 minimizes the AIC computed with an empirical redundancy parameter of α=400.

Model	Variance (percent)	Variance for 'improvement window'	AIC (α=250)
PREM	97.5		—
PREM with time shift	84.1	84.6	5652.5
CG6	79.1	48.4	5529.1

Table 3.2 Variance and Akaike information criterion (AIC) value for each model using data in the period range between 20 and 200 s. Variance of the synthetics for PREM, PREM with time-shifts with static corrections, and our final model with six conjugate gradient vectors (CG6; Fig. 3.3b). CG6 minimizes the AIC computed with an empirical redundancy parameter of α=250.

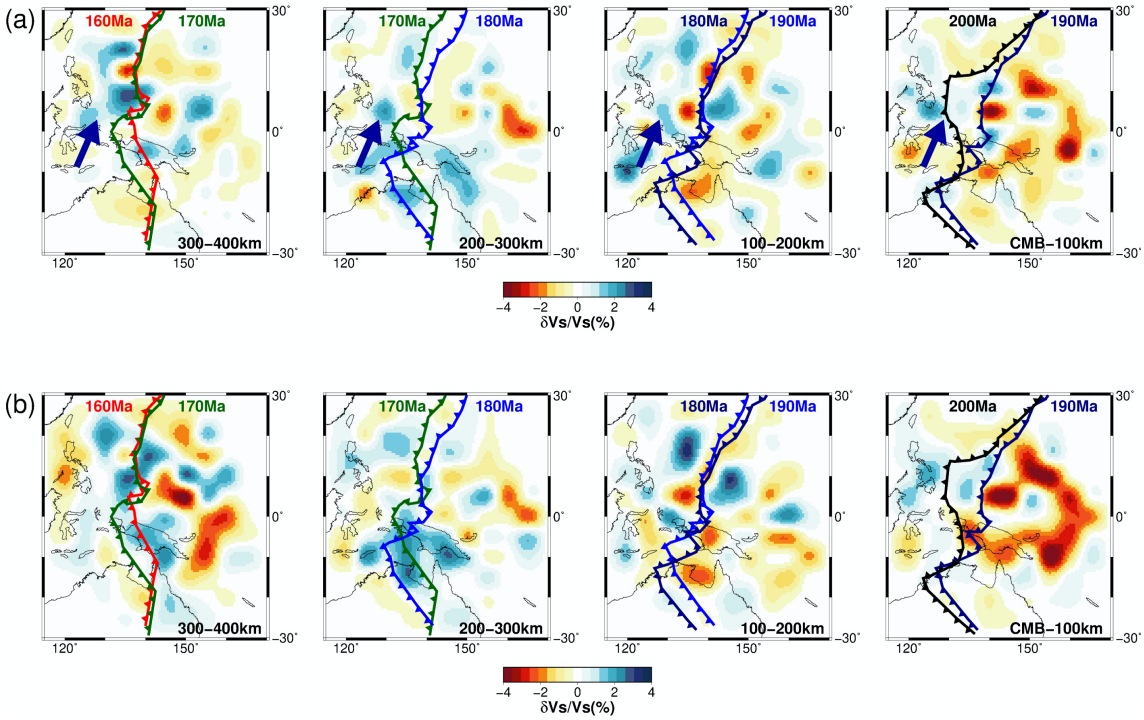

Figure 3.3 Results of our inversion for the 3-D S-wave velocity structure. (a) The top four panels show results using data in the period range between 12.5 and 200 s for the four depth layers from the CMB to 400 km above the CMB, respectively. (b) The bottom four panels show results for longer period range data (from 20 to 200 s). Assuming a global average slab sinking rate of ~1.4 cm/year, remnants of the subducted Izanagi slab 200 Ma should be found at the CMB, 190 Ma should be found 100 km above the CMB, and so on, as shown in the respective panels. The location of the vertically continuous high-velocity anomaly beneath the Philippine Sea (blue arrows), agrees with the location of the reconstructed paleo-Izanagi subduction on the surface at each depth (Young et al., 2019). Small-scale low-velocity anomalies exist immediately above the CMB and some of the low-Vs anomalies extend to a height of 400 km above the CMB.

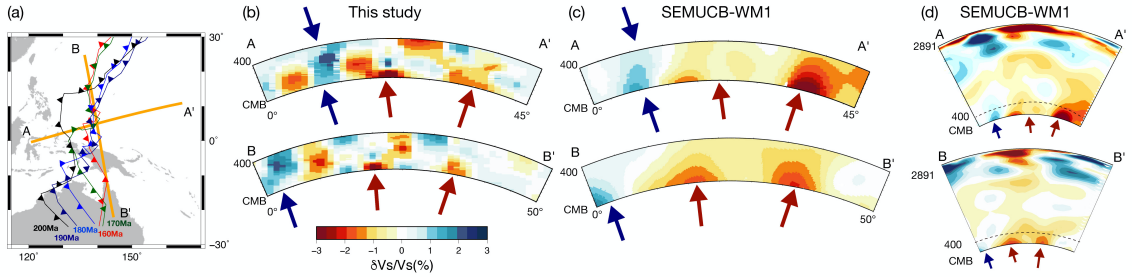

Figure 3.4 Cross-sections for the 3-D shear wave velocity structure (A–A′ and B–B′). (a) Map of the studied area. The orange lines show the orientation of the two cross-sections. The Izanagi-plate boundaries on the surface at various ages are shown in the same way as in Fig. 3.2. (b) Cross-sections for the model obtained using data in the passband 12.5–200 s. (c, d) Cross-sections for the model obtained by a previous global waveform inversion study (French & Romanowicz, 2014). The locations of high- (low-) velocity anomalies, marked by blue (red) arrows in panels (b), (c), and (d), are in good general agreement. The continuous low-velocity anomaly in cross-section B–B′ for our model corresponds to the low velocity anomaly continuous up to the surface in cross section B-B′ in panel (d). Note that the maximum amplitude shown by the color scale in panel (b) is the same as in (c) and (d).

In Fig. 3.4 we compare our S-velocity structure for the lowermost 400 km beneath the western Pacific to that obtained by a previous global waveform inversion study (SEMUCB-WM1; French & Romanowicz, 2014). As shown in Fig. 3.3a, we present cross-sections along two profiles: northwest(A) to southeast(A′), roughly perpendicular to the reconstructed Izanagi plate boundary ~200 Ma; and southwest(B) to northeast(B′), roughly parallel to the past Izanagi plate boundary. The location of high- and low-velocity anomalies (marked by the red and blue arrows, respectively in Fig. 3.4) immediately above the CMB in our model (Fig. 3.4b) generally agrees with that shown in the global tomography model (Figs. 3.4c and 3.4d), but our model has finer resolution. In Fig. 3.5, we compare the lowermost layer of our model using data in both passbands

(12.5–200 s and 20–200 s) to that for the SEMUCB-WM1 model. The inversion result for the longer period range data (Figs. 3.3b and 3.5b) is generally consistent with the SEMUCB-WM1 model; however, the model obtained using shorter period range data (Figs. 3.3a and 3.5a) has relatively small (a diameter of ~300 km) scale low-Vs areas at the western margin of the Pacific LLSVP. The inversion of shorter-period (up to 12.5 s) waveforms makes it possible to image smaller-scale structure with finer resolution than global tomography.

The northeast boundary area of the study area and the southwest boundary of the study area of Konishi et al. (2014) partially overlap. In order to confirm the consistency between the two studies, we are planning to assemble the two-target areas into a single dataset and to conduct the 3-D waveform inversion for the entire region in the near future.

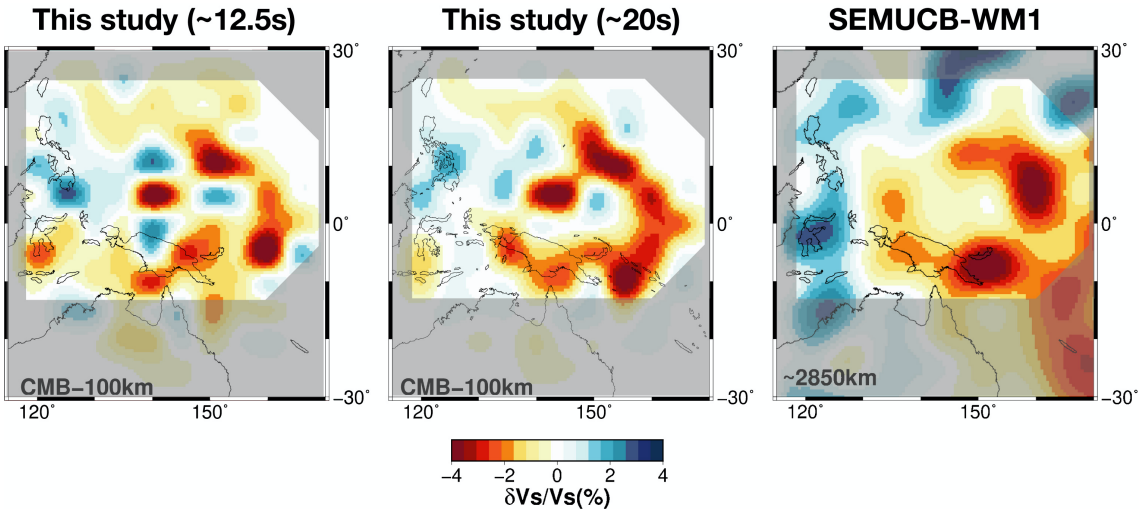

Figure 3.5 Comparison with global tomographic model (map view). Left panel is lowermost layer of our final model using data in the period range between 12.5 and 200 s and middle panel is lowermost layer of our final model with the data in the period range between 20 and 200 s, while right panel is 2850 km depth slice of the SEMUCB-WM1 model (French & Romanowicz, 2014) for this study region. Each panel has been grayed out where our dataset lacks resolution.

We conducted tests to confirm the resolution and accuracy of the model (Figs. 3.6 to 3.8). To check the ability of our methods and dataset to resolve the structure in the target, we conduct a spatial resolution check ('Checkerboard test'; see Figs. 3.6, 3.7, and 3.8). To evaluate the trade-off between target structure and shallow structure such as subducted Pacific and/or Philippine Sea slabs, we also verify that our partial derivative kernel for structure in the target region is nearly completely independent of the partial derivative kernel for the upper mantle (100-500 km depth) structure beneath the western Pacific subduction zone (see Fig. 3.10).

Since we combined the E–W and N–S datasets, the dataset used in our inversion has wider azimuthal coverage than previous studies. Previous travel-time analysis and waveform modeling studies (He et al., 2006; Takeuchi et al., 2008)

investigated the western portions of the regions investigated in this study and suggested laterally sharp S-velocity variation at the western edge of the Pacific LLSVP using only E–W raypaths, whose boundary is to the almost N–S direction. Since the waveforms used in the previous studies sample the low-velocity region, finite frequency effects such as focusing/defocusing and wavefront healing should be considered in order to investigate the structure of the boundary of the Pacific LLSVP in more detail. On the other hand, our dataset with wider azimuthal coverage can provide better constraints on the spatial S-velocity variation of the LLSVP and its surrounding mantle, especially the location of the boundary.

3.4 Resolution and validation check

To examine the ability of our method to resolve the structure in the target region, we conduct synthetic resolution ('checkerboard') tests (Figs. 3.6 and 3.7). We confirm that for an ideal noise-free case that the waveform inversion method and dataset used in this study can resolve the lateral heterogeneity well in all the depth ranges for the target region of this study. Since longer wavelengths are expected to have less resolving power than shorter wavelengths, this difference in the resolution could produce the small differences between the 3-D S-velocity models shown in Figs. 3.3a and 3.3b. Even when the resolution is good, artifacts in the inferred model can arise because of errors in the data (e.g., noise). In order to further investigate the resolution difference between the period ranges to check the robustness of our inferred model, we will conduct the checkerboard test with artificial noise.

As an additional test of the validity of the Born approximation for

inversion for S-velocity in D″, we show a “nonlinear checkerboard test” in Fig. 3.8. The input model is the same as for the linear case. Synthetic seismograms for this model were computed using full 3-D waveform calculation (SPECFEM3D_GLOBE; Komatitsch & Tromp, 2002a, b; Komatitsch et al., 2015). Because of heavy computational requirements with increasing maximum frequency, we computed synthetics down to ~13 s and filtered them with a bandpass filter between 20 and 200 s. The result (Fig. 3.8) shows that the inversion using the Born approximation underestimated the absolute amplitude of the perturbations by about 20 percent (~2 percent for the inversion result, compared to the 2.5 percent perturbation of the input pattern) but that the pattern of high- and low-velocity anomalies was reasonably well recovered.

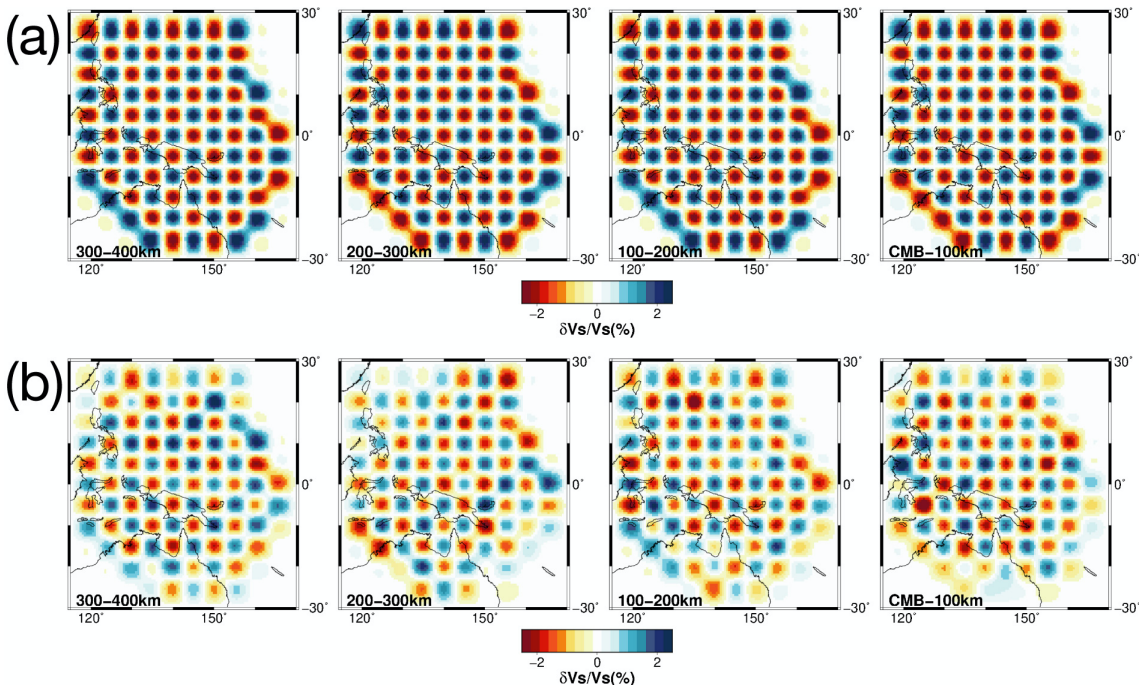

Figure 3.6 Synthetic resolution test (‘Checkerboard test’) for the period range data (~12.5 s). The input patterns with 2.5 percent heterogeneities of dimension 5˚ x 5˚ laterally x100 km vertically are shown on the top panel (a). The dataset and the number of CG vectors for the checkerboard test are the same as for the actual inversion. This result shows that we can nominally resolve almost all the voxels in the target region. (b) is showing checkerboard test results for complete dataset. Note that the maximum amplitude shown by the color scale in panel (a) is the same as (b).

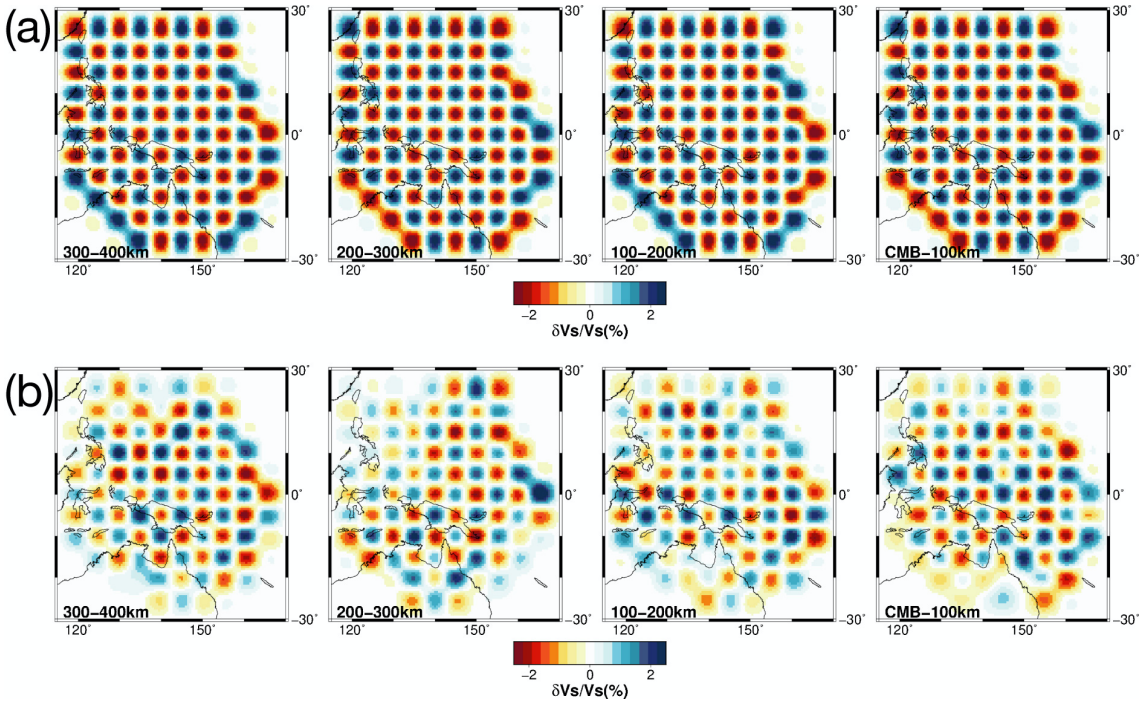

Figure 3.7 Synthetic resolution test ('Checkerboard test') for the dataset in the passband 20–200 s. The input patterns with 2.5 percent heterogeneities of dimension 5˚ x 5˚ laterally x100 km vertically are shown on the top panel (a). The dataset and the number of CG vectors for the checkerboard test are the same as for the actual inversion. This result shows that we can nominally resolve almost all the voxels in the target region. (b) is showing checkerboard test results for complete dataset. Note that the maximum amplitude shown by the color scale in panel (a) is the same as (b).

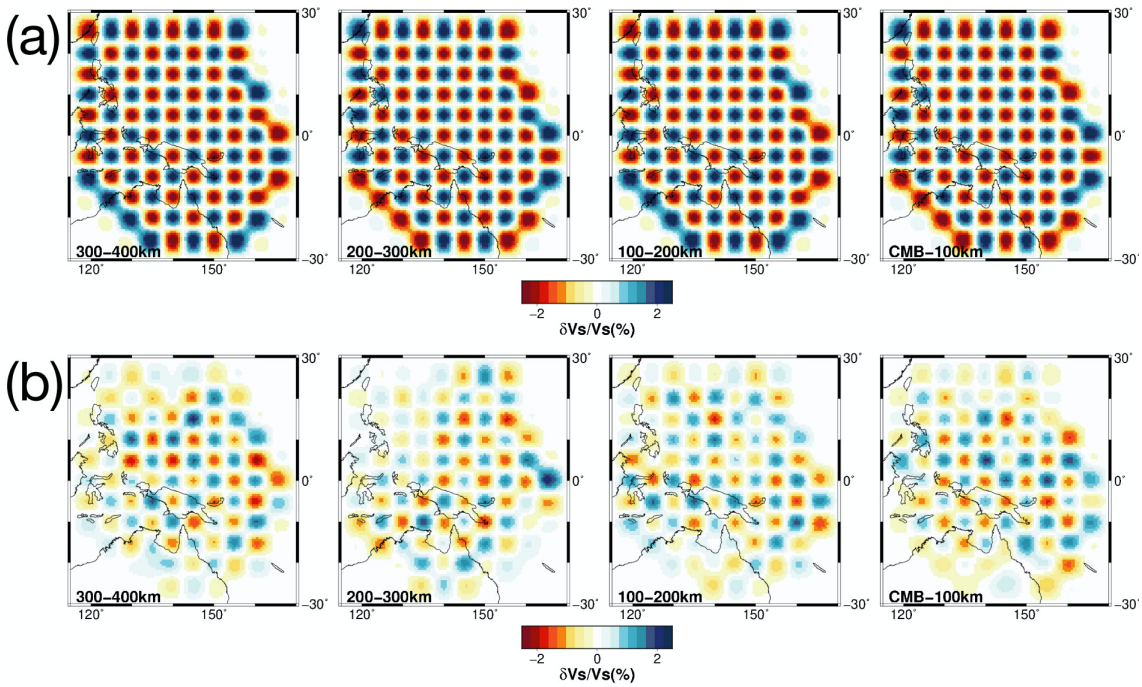

Figure 3.8 A nonlinear checkerboard test by using input synthetics computed using full 3-D waveform calculation (SPECFEM3D_GLOBE; Komatitsch and Tromp, 2002a, b; Komatitsch et al., 2015). Input checkerboard pattern used for the full 3-D wave calculation is the same as for linear case (Figs. 3.6 and 3.7), with 2.5 percent heterogeneities of dimension 5 ˚ x 5 ˚ laterally and 100 km vertically. The synthetics for this input pattern are accurate down to a period of ~13 s, and filtered with a Butterworth bandpass filter between 20–200 s, as for the actual inversion.

In our inversion process, the target region is only in the lowermost 400 km of the mantle and the structure for shallow regions is assumed to be the anisotropic PREM model (Dziewonski & Anderson 1981). In order to examine the possible effects of shallow structure, such as the subducting Pacific and Philippine Sea slabs, on the inversion results, we also checked the independence of the partial derivatives for perturbations in such regions from those in the target region in the lowermost mantle (Fig. 3.9). This indicates that if we had only one station and one record then it would be

impossible to resolve the tradeoff, but with a total of thousands of records (many stations for many events) the inversion algorithm can resolve the tradeoff with only a small uncertainty. As shown in Fig. 3.2, the dataset in this study is large enough to effectively eliminate the trade-off between shallow structure and structure in the target region when all seismograms and all stations are used. Our present dataset allows us to resolve structure in D″ over a wider horizontal region (a range of about 2000 km) as compared to about 1000 km for Konishi et al. (2014). This better facilitates an investigation of the structure inside the Pacific LLSVP.

As an additional check of the absence of smearing, we conducted point-spread function tests (Fig. 3.10). The results confirm the absence of smearing in the North-South direction. This suggests that the fact that the ring-shape and vertically continuous low-velocity anomaly is probably a feature of the actual structure in D″ beneath western Pacific, and not an artifact due to smearing.

A previous ScS-S differential traveltime analysis reported relatively large positive travel time anomalies (but less than 10 s) in the observed waveforms which sampled the D″ region beneath the western Pacific (Takeuchi et al., 2008; He et al., 2006). In order to roughly determine the observed arrival times for our data, we measure the phase delay times as the time shifts from the predicted onset time for PREM which give the best cross-correlation coefficient. We observed relatively large positive time shifts interpreted as ScS phase delays (but less than 10 s) as shown in Fig. 3.16 (the horizontal axis of Fig. 3.16 indicates the observed phase delay). We then compute time shifts of the final 3-D synthetic waveforms, which are computed using the first order Born approximation as shown in Fig. 3.16. Fig. 3.16 shows that: 1) positive time shifts up to ~8 s; 2) generally good correlation between synthetic and observed data for positive time

shifts; 3); relatively poor correlation for negative time shifts; 4) that the determination of the best correlation time is difficult, since the ScS phase is overlapping with later S phases. To check the epicentral distance dependency, we plot the time shifts of the selected dataset for epicentral distances less than 80˚ (Fig. 3.16b). Fig. 3.16b shows that the variation of the time shifts for shorter epicentral distance indicates similar to the variation of time shifts for the complete dataset.

Although the first order Born approximation cannot reproduce a phase delay greater than $\pi/2$, our obtained time shifts for the Born synthetics reproduces phase delays of up to ~8 s. Note that the time shifts interpreted as ScS phase delay should not be used for validation of the inferred model because our dataset consists of not only S and ScS but also phases between S and ScS due to superposition of wavefields excited by heterogeneous structure in D″.

In order to check the improvement of waveforms after inversion, we show in Fig. 3.11 record sections for two events of stacked waveforms in 1-degree epicentral distance bins for the data, synthetics for PREM, and Born synthetics for the 3-D model. Fig. 3.11 shows that not only the ScS phase is improved by the inversion, but also the later S phases. We also confirm visually that the fit to the data for the waveforms computed using SPECFEM3D_GLOBE for our 3‑D final models (Fig. 3.3a) is generally improved (see Fig. 3.12). Figs. 3.12 and 3.13 shows that 3-D synthetics using the Born approximation generally agree with the 3-D synthetics computed using SPECFEM3D_GLOBE. This implies that 3-D synthetics using the Born approximation are a sufficient approximation in this period range (i.e., 12.5–200 s) for the 3-D synthetics computed using SPECFEM3D_GLOBE. Since SEM synthetics have reasonably good agreement with the first order Born synthetics in terms of a time shift interpreted as ScS

delays up to ~8 s, the perturbation of wavefields of later phases of the direct S phase should be due to superposition of wavefields excited by heterogeneous structure in the D″ region, i.e. constructive and/or destructive interference.

The first order Born approximation is only strictly accurate for infinitesimal perturbations. We perform the block test using waveforms accurately computed for spherical symmetric perturbations using the DSM (Geller & Ohminato, 1994; Kawai et al., 2006). The input models with spherically symmetric perturbations of -3.5 percent in layers 100 km-thick just above the CMB are reasonably well recovered in our study region. Fig. 3.17 shows that the recovered amplitude matches that of the input model. This implies that the Born approximation can reproduce the relatively strong and long-wavelength perturbation within a target region. We also conduct a different type of block test using the Born approximation (Fig. 3.18). We compute the Born synthetics for input models in Fig. 3.18 and then conduct the inversion. The obtained pattern after inversion recovered: (a) the low-velocity conduit; (b) a high-velocity anomaly surrounded by small-scale low-velocity patches; (c) small-scale low-velocity patches. This implies that these characteristic structures (a–c) in our inferred model are not an artifact.

Panning et al. (2009) suggested that the simple and computationally efficient PAVA-based non-linear modification improves the performance of the linear Born approximation by improving the modeling of the effects of the long-wavelength structure for fundamental mode for Rayleigh wave. We conduct 1-D iterative inversion for the S-velocity structure (Kawai et al., 2007; Konishi et al., 2009) in the target region with respect to the global reference model PREM and obtained regional 1-D spherical symmetric structure as a typical long-wavelength heterogeneity (hereafter called PREM′; see Fig. 3.14). Note that we think that PREM′ is not simply the horizontal average of Fig

3.3a. Since it is necessary to compare PREM′ with the average 3-D velocity structure which varies according to the resolution, finding the optimum way to determine the average structure taking into account the lateral variation of resolution is an important topic for future research. We then use PREM′ as the starting model for the 3-D inversion and then conduct 3-D waveform inversion. Map views of the resulting 3-D model are shown in Fig. 3.15. This 3-D S-velocity model is in good general agreement with the 3-D model obtained using PREM as an initial model shown in Fig. 3.3. This robustness between the S-velocity models shown in Figs. 3.3 and 3.15 implies the long-wavelength heterogeneity does not significantly affect the final inversion result. Here we list the possible reasons for this agreement: 1) Panning et al. (2009) conducted several synthetics comparison for surface waves not for body waves which we use in the inversion in this study. Figs. 2–5 of Panning et al. (2009) show that errors in the fundamental mode are relatively large but that errors for overtone modes are small; 2) we use waveforms in the period range 12.5–200 s, while Panning et al. (2009) used the waveforms in the period range 120–200 s; 3) we use differential waveforms including S and ScS phases but Panning et al. (2009) isolated Rayleigh waves.

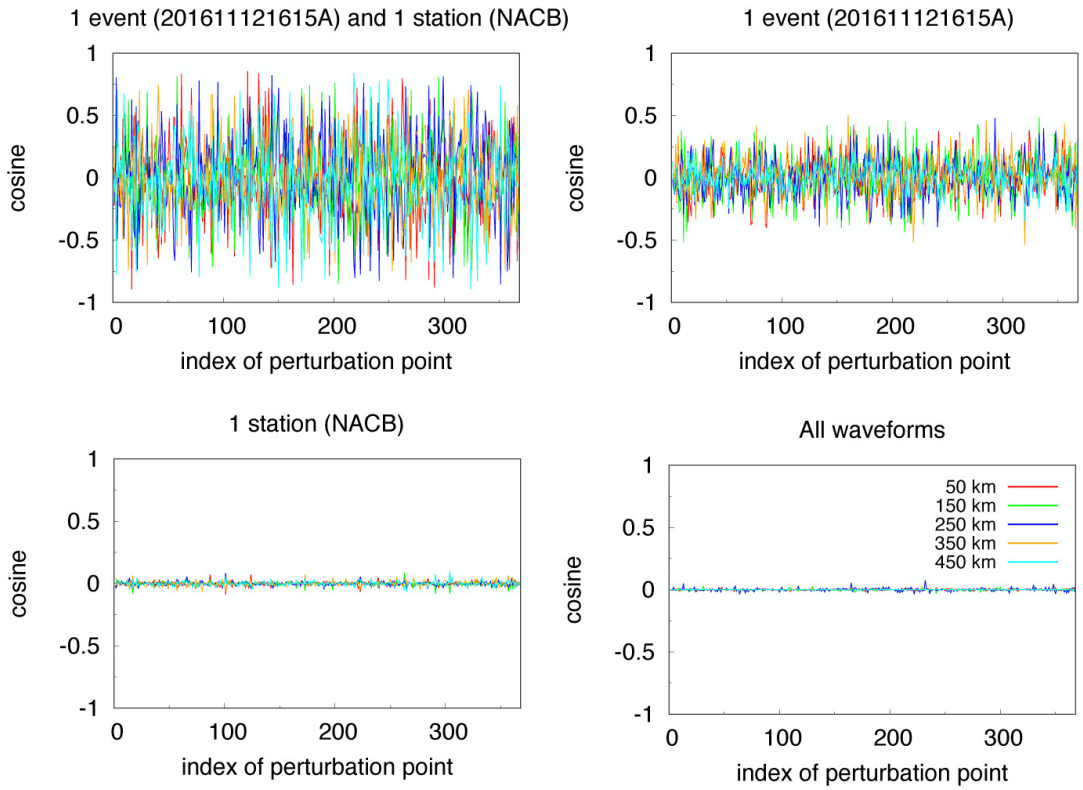

Figure 3.9 Cosine of the angle between the vector of partial derivatives for each of the 368 voxels in the target region (D″) and the vector of partial derivatives for each of the 5 voxels in the upper mantle beneath the western Pacific subduction zone at 30˚ N, 120˚ E and 50, 150, 250, 350, and 450 km depth, to consider effects from subducted Pacific and Philippine Sea slabs in the upper mantle. The legend for each panel is the same as that shown in panel d). The four panels indicate the increasing number of records used in the partial derivative vectors: (a) one station, one event (1 record); (b) all stations, one event (14 records); (c) one station, all events (371 records); (d) all stations, all events (5381 records).

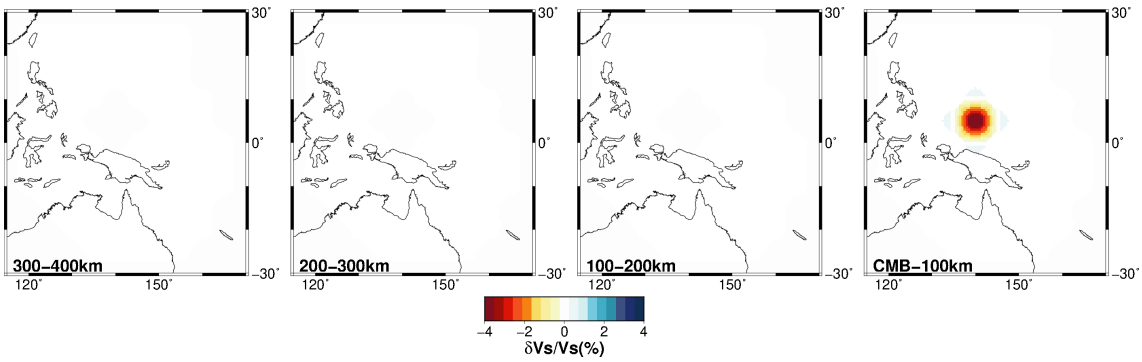

Figure 3.10 Point-spread function. Panel shows the result of inversion for a synthetic input model with only one voxel perturbed. S-velocity -3.5 percent at 140˚ longitude, 5˚ latitude, and 50, 150, 250, and 350 km above the CMB. The results do not show any effect of smearing from the perturbed voxel, suggesting that the inversion can resolve voxels individually.

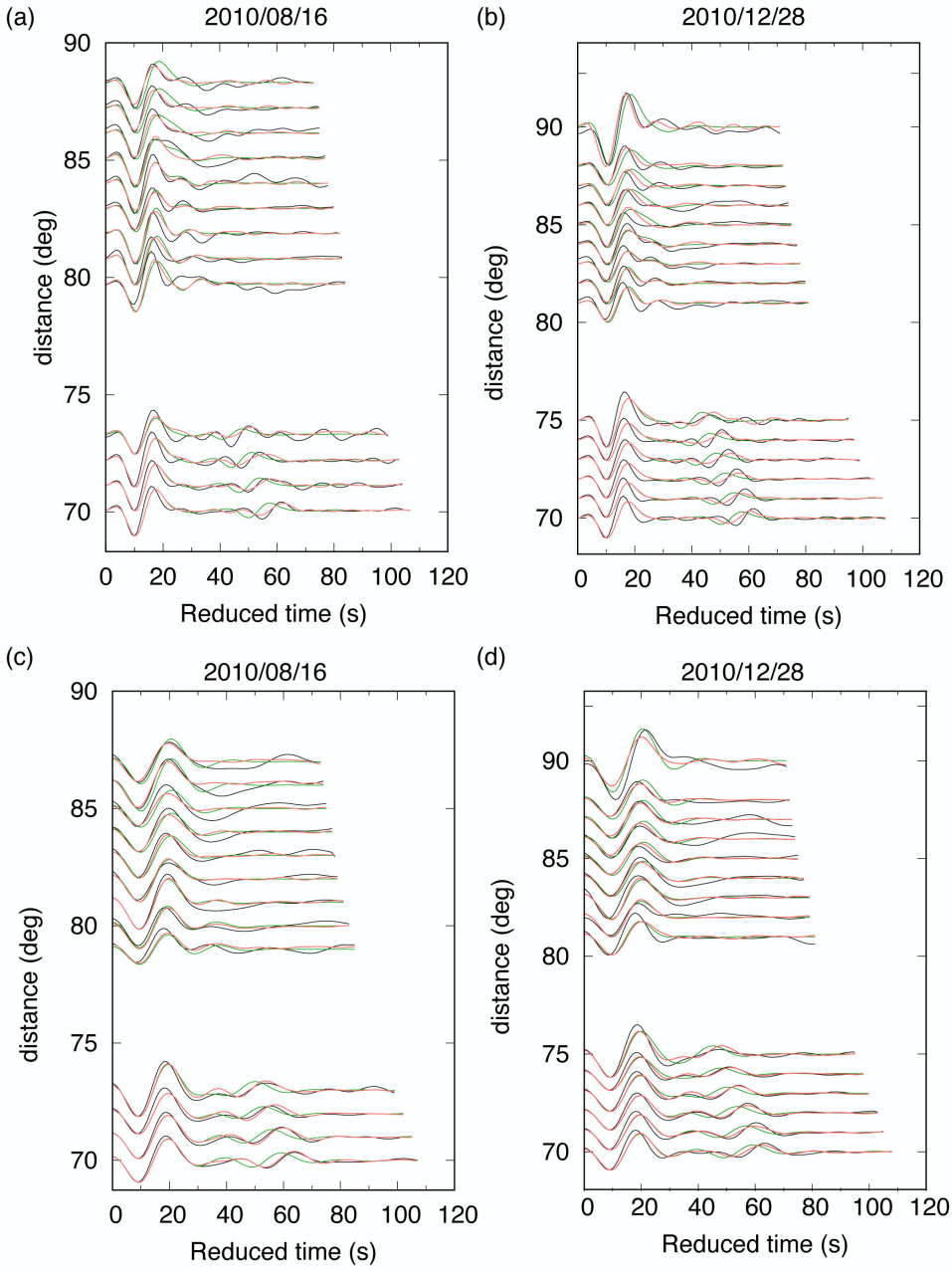

Figure 3.11 Quality control stacks. Record sections for the two events #319 and #325 in Table B1. The traces are stacked every 1˚ of epicentral distance (the time-shifts used in the inversion are applied to the observed data). Observed traces are shown in black. The top row, (a) and (b), shows synthetic waveforms in the passband 12.5–200 s for the initial models PREM (green), and final model (pink). The bottom row, (c) and (d), shows synthetic waveforms in the passband 20–200 s for the initial model PREM (green), and final models (pink).

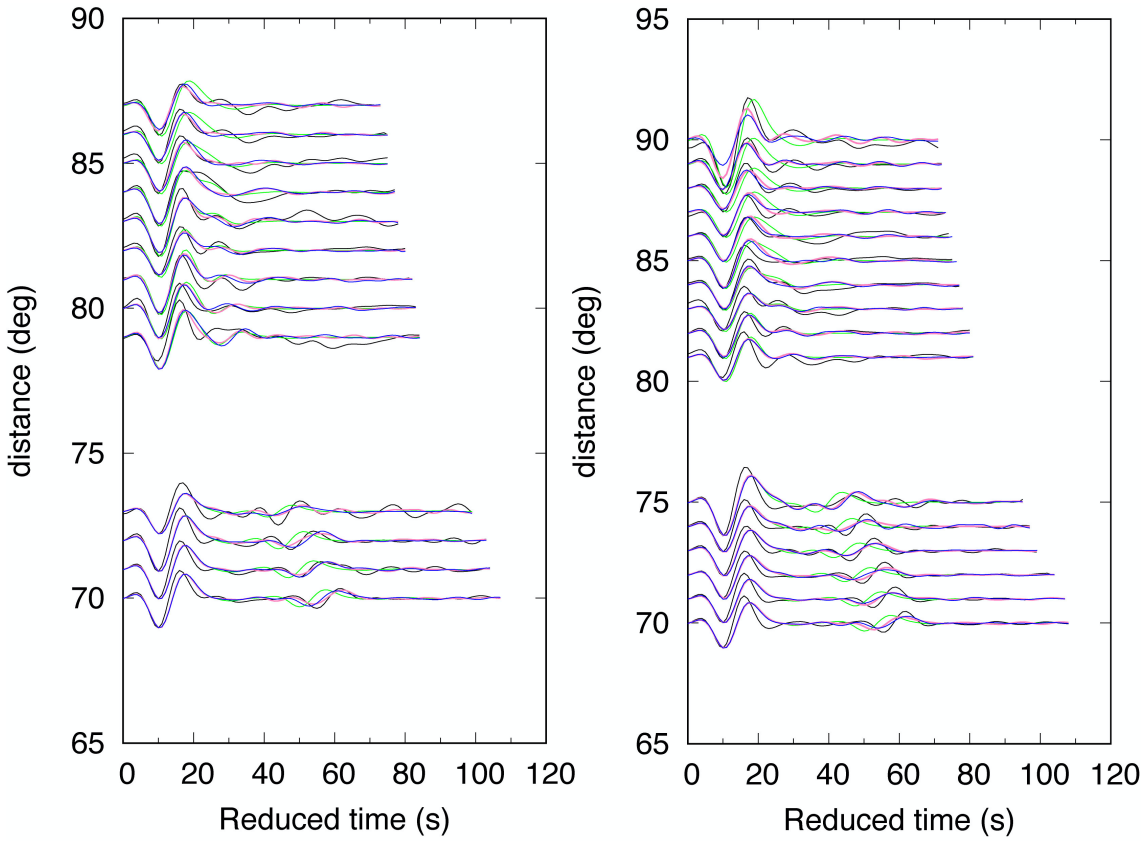

Figure 3.12 Quality control stacks to verify the improvement of synthetics after the inversion. Record sections are shown for the two events #319 and #325 in Table B1 stacked in 1˚ epicentral distance bins. Panels show record sections for actual data (black lines), synthetics for PREM (green lines), synthetics for the final model using Born approximation (pink lines), and synthetics for the 3-D final model using SPECFEM3D_GLOBE (blue lines). The waveforms are in the passband 12.5–200 s.

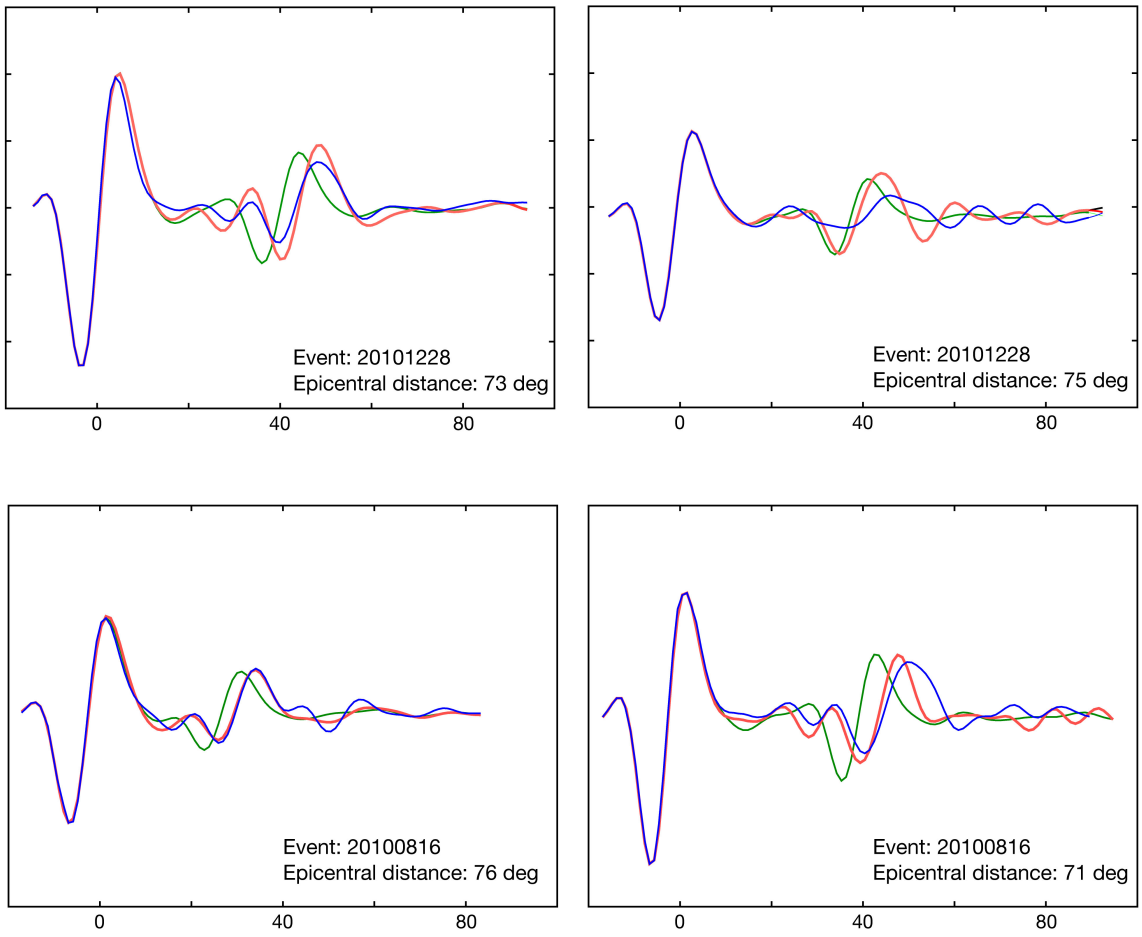

Figure 3.13 Waveform traces to verify the improvement of synthetics after the inversion. Waveforms are shown for the two events #319 and #325 in Table B1 in the passband 12.5–200 s. Panels show waveforms for synthetics for PREM (green lines), synthetics for the final model using Born approximation (pink lines), and synthetics for the 3-D final model using SPECFEM3D_GLOBE (blue lines).

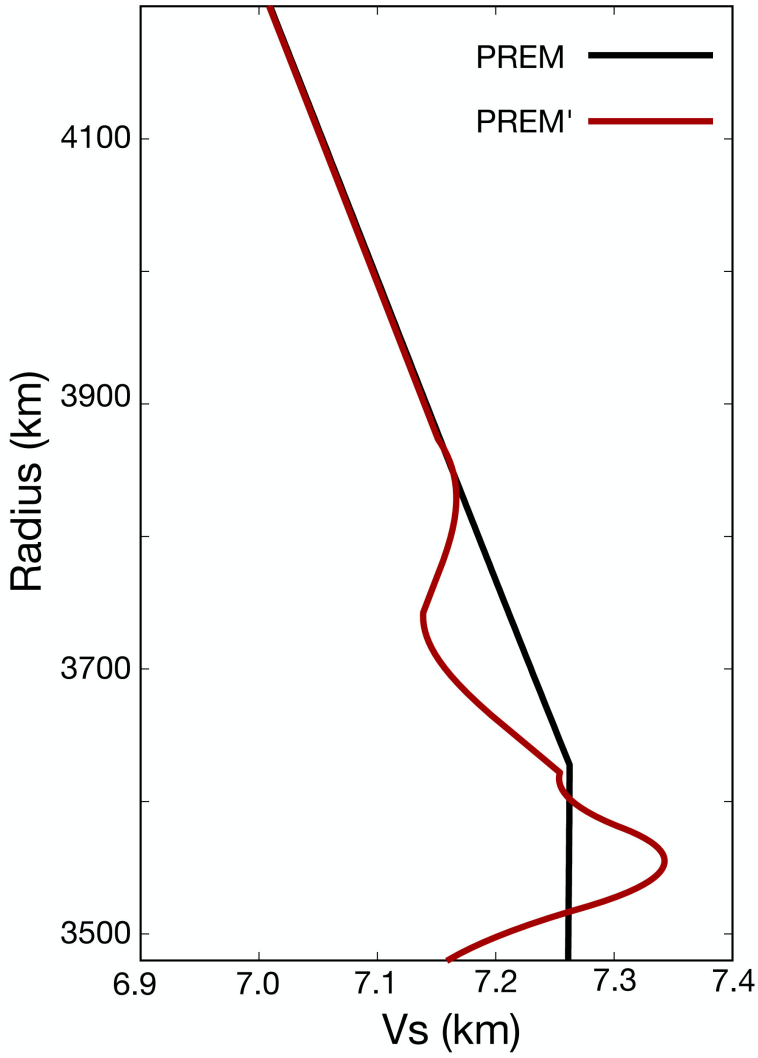

Figure 3.14 Initial models for 3-D inversions. I used two different 1-D models as initial models in the inversion for 3-D structure. PREM is a global reference model (Dziewonski & Anderson, 1981), and PREM′ is a local model we inferred for the lowermost 400 km of the mantle beneath western Pacific using 1-D waveform inversion (Kawai et al., 2007; Konishi et al., 2009) with the same dataset as for 3-D inversion.

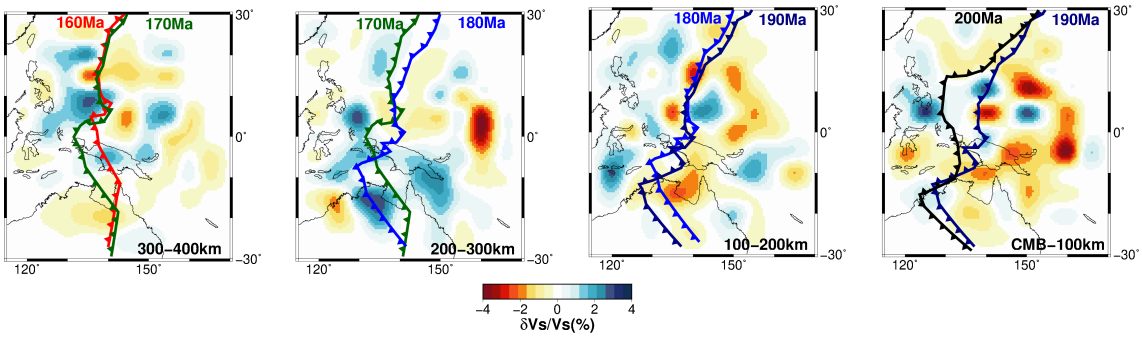

Figure 3.15 Same as Fig. 3.3a but using PREM′ (Fig. 3.13) as the initial 1-D model. The velocity perturbations are shown with respect to PREM. The inversion result using PREM as the starting 1-D model shown in Fig. 3.3a and the inferred model using PREM′ as the initial 1-D model are in generally good agreement, which suggests that the inferred model is robust.

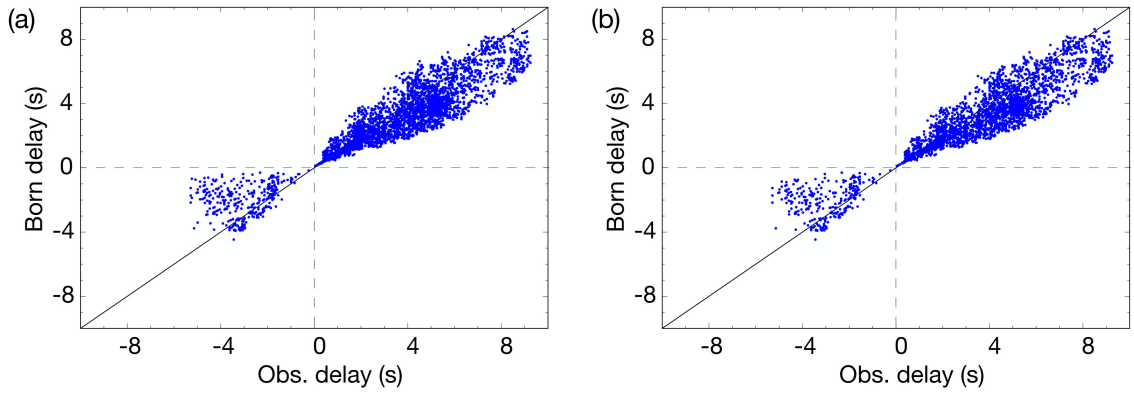

Figure 3.16 ScS phase delay as the time shifts comparison between observed waveform and synthetic waveform for the final model which was obtained using the Born approximation. We measured ScS phase delay times from 1-D synthetic seismogram for PREM computed by DSM (Geller & Ohminato, 1994; Kawai et al., 2006). (a) Complete dataset. (b) Selected dataset for epicentral distances less than 80˚.

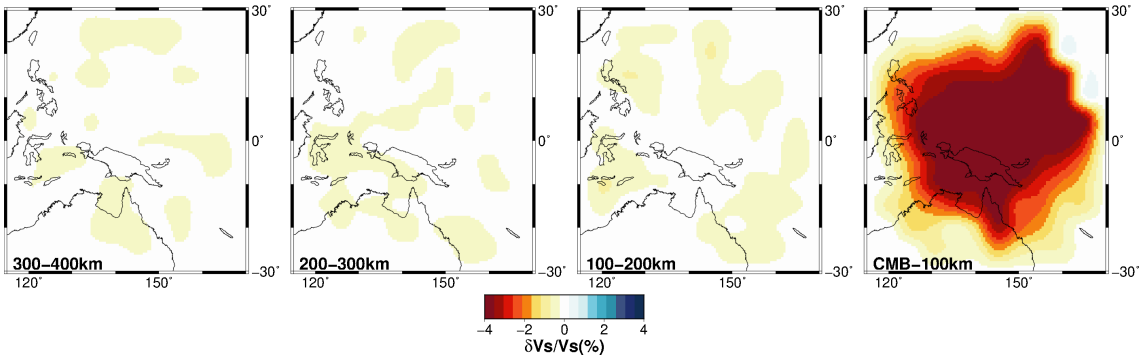

Figure 3.17 Block test. 3-D inversion using as input exact 1-D synthetics computed with the DSM (without using the Born approximation) for 1-D models that differ from PREM by a 3.5 percent decrease the S-velocity 0–100 km above the CMB.

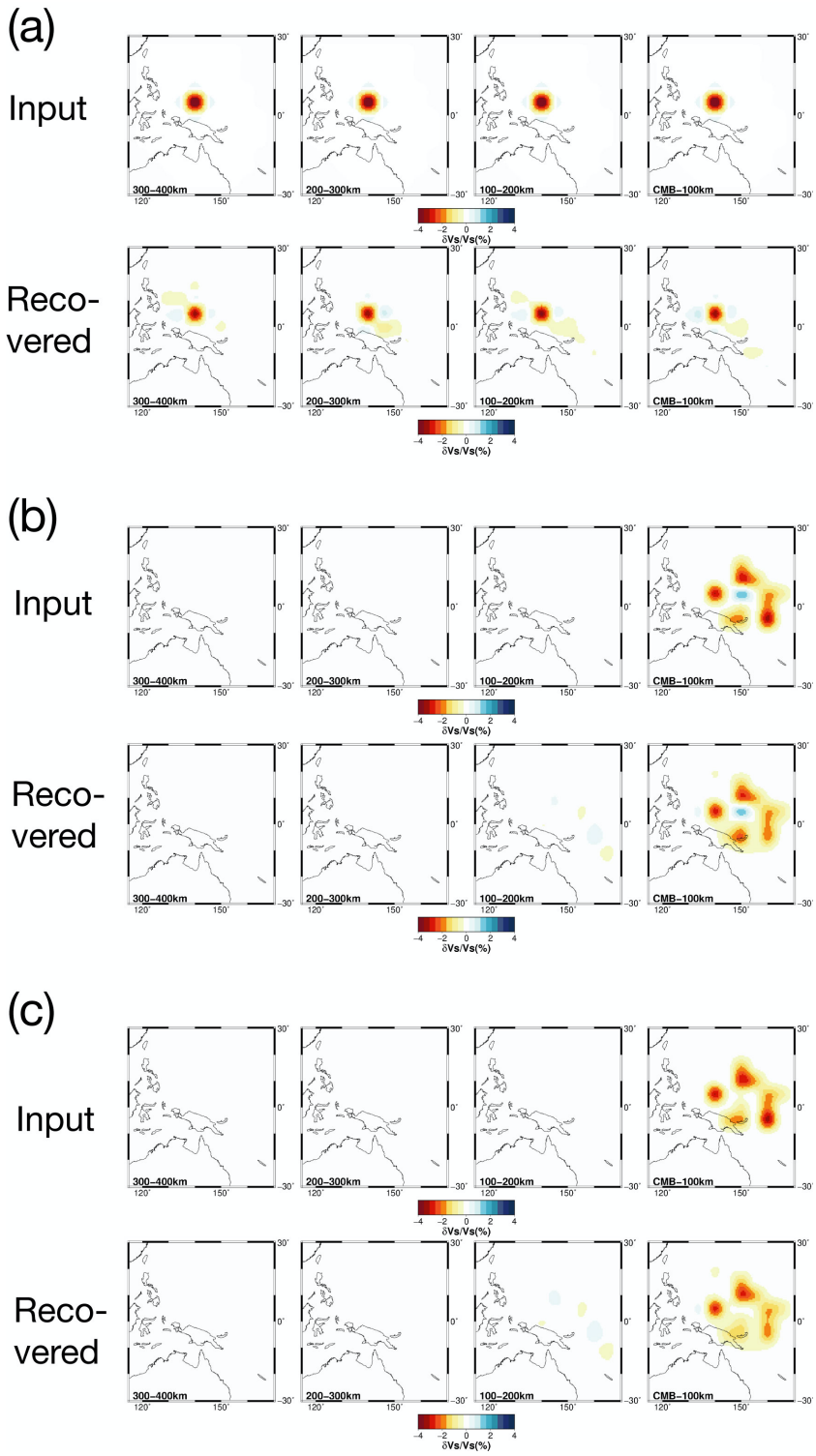

Figure 3.18 Block tests using the Born approximation. Panels (a–c) show the result of inversion for a synthetic input model ("Input" for each panel). These results show that the input models are reasonably well recovered.

3.5 Discussion and Geophysical implications

We conduct 3-D waveform inversion and obtained small-scale D″ structure. The inferred model shows following key features; (i) There are significant (up to ~3.5 percent) high-velocity anomalies beneath the Philippine Sea that extend vertically from the CMB to 400 km above the CMB (marked by blue arrows in each panel in Fig. 3.3), whose location is generally consistent with that of the past Izanagi-plate boundaries at the ages shown in each panel of Fig. 3.3; (ii) There are small-scale low-Vs anomalies with a diameter of ~300 km (up to ~3.5 percent slower than PREM) immediately above the CMB (Fig. 3.3); (iii) There is a vertically continuous (CMB to at least 400 km above the CMB) low-velocity structure above the low-velocity anomalies at the CMB (Figs. 3.3 and 3.4). We consider following 3 possibility to interpret the inferred S-velocity structure; (a) we assume that the S-velocity anomalies can be primarily attributed to effects of temperature and the high- and low-velocity anomalies indicate colder and hotter than average temperatures at each respective depth; (b) in case that the inferred S-velocity anomalies can be explained by temperature, chemical anomalies, or a combination of the two; (c) alternative possible chemical compositional anomaly.

(a) Temperature anomalies

Since the S-velocity anomalies can be primarily attributed to effects of temperature, the high- and low-velocity anomalies indicate colder and hotter than average temperatures at each respective depth. Our model thus suggests the presence of cold material at the CMB and upwelling flows of hot material from the CMB, suggesting that the western margin of the LLSVP consists of a cluster of smaller-scale thermal plumes

(Fig. 3.19).

The magnitude of the high-velocity anomalies in D″ could be due to the total effects of low temperatures and the phase transition from the bridgmanite (abbreviated as MgPv below) to the Mg-post-perovskite (abbreviated as Mg-pPv below) phase (Murakami et al., 2004; Tsuchiya et al., 2004). Of the ~3.5 percent of the high-Vs anomalies in our obtained 3-D S-velocity structure model, ~1.5 percent can be explained by the MgPv to Mg-pPv phase transition. The remaining +2.0 percent anomaly can be explained by a 450 K decline in temperature, using the temperature derivative for Mg-pPv under lowermost mantle *P-T* conditions (Wentzcovitch et al., 2006). On the other hand, when we assume the MgPv to Mg-pPv phase transition does not occur in our target region, ~3.5 percent of the high-Vs in our model can be explained by a ~730 K decline in temperature. Since, due to vigorous convection of the outer core, the lateral variation of the CMB temperature could be small (Stevenson, 1981), a 450 K or 730 K decrease in temperature over a depth range of ~50-100 km, or less above the CMB strongly suggests the presence of cold material.

The small-scale low-velocity anomalies with a diameter of ~300 km could be explained by high temperature anomalies. The velocity contrast observed in the lowermost 100 km of the mantle is around -3.5 to 3.5 percent over less than 200 km vertically and 300 km laterally. If the low-velocity anomalies immediately above the CMB found in this study are interpreted as due to temperature anomalies alone, the region up to ~100 km above the CMB would reach the CMB temperature of 3800 K (Kawai & Tsuchiya, 2009), because temperature deviations of ~1300 K from the mantle adiabat at the CMB of 2500 K (Brown & Shankland, 1981) would produce a ~5 or ~4 percent velocity reduction for the Mg-pPv or Mg-Pv phase, respectively (Wentzcovitch et al.,

2006).

Previous seismological studies suggested an abrupt lateral transition in S-velocity (e.g., He et al., 2006; Takeuchi et al., 2008; Idehara et al., 2013) at the margins of LLSVP called the 'sharp-sided boundary' of the LLSVP. While it is generally considered too sharp to be explained by isochemical thermal features (e.g., Ni et al., 2002; McNamara and Zhong, 2005), Davies et al. (2012) pointed out that it was not necessary to invoke chemical heterogeneity to produce observed short-wavelength variation in seismic velocity at the margin of LLSVP, because their model showed that hot thermal anomalies beneath the western Pacific are closely bounded by cold material with a steep thermal gradient of 800–1000 K/100 km. The geometry of low-velocity anomalies immediately above the CMB adjacent to the vertically extended high-velocity anomalies found in this study is consistent with the results for a sharp-sided boundary of the Pacific LLSVP (He et al., 2006 and Takeuchi et al., 2008), although we also inferred laterally heterogeneous structure inside the low-velocity region (see Fig. 3.19). This suggests that the sharp boundary at the western Pacific can be explained by a subducted cold paleoslab, which is consistent with previous geodynamical studies considering past plate motion at the surface (Davies et al., 2012).

(b) Temperature, chemical, or a combination

Since it is difficult to explain several percent velocity increase as the result of differences in chemical composition alone, we here consider the low-velocity anomalies. The low-velocity regions in the lowermost mantle can be explained by high temperatures, chemically distinct material, or a combination of the two. Pyrolite is widely

thought to be the average composition of the lower mantle (Wentzcovitch et al., 2004), but the details of the bulk composition of the lower mantle remain controversial (Ringwood, 1989; Cottaar et al., 2014). Chemical compositions with increased amounts of impurities such as Fe and Al have lower shear velocities than pyrolite (Tsuchiya, 2011; Zhang et al., 2016). Such chemical heterogeneity, resulting from exchanges between the core and the mantle, from partial melting in the TBL, from basalt entrained to the base of the mantle by past subduction, or as long-lived remnants of chemical differentiation in the early Earth, is expected at the CMB (Garnero & McNamara, 2008).

Our inferred structure within LLSVP suggests that western Pacific LLSVP consists of a cluster of small-scale low-velocity anomalies with a diameter of ~300 km. We considered if the chemical anomaly can explain seismic low velocity anomalies. About 2 or 3 percent low-Vs anomalies could be due to chemical compositional impurities such as Fe and Al (Tsuchiya & Tsuchiya 2006; Zhang et al., 2006). Such chemical anomalies with an impurity content of 5–6 percent produce ~2 or ~3 percent low-Vs anomalies (Wentzcovitch et al., 2006; Tsuchiya & Tsuchiya, 2006) and could be produced as drift by mantle flow in the LLSVP. Then, isolated chemically distinct regions could be intensively heated due to heat flux from the core and radioactive heating.

Chemical heterogeneities with enriched iron content (that is, basaltic composition) have a lower seismic velocity than pyrolite and can explain strong negative anomalies (Tsuchiya, 2011). They are also denser than pyrolite and thus could remain close to the CMB. Our model shows that significant low-velocity anomalies are in the lowermost 100 km of the mantle. Chemical anomalies at the CMB also provide the possible explanation for the significant velocity gradient we observe within 100 km of

the CMB.

(c) Alternative possible chemical anomalies

Subducted basaltic oceanic crust (MORB) is a complex mineral assemblage that is enriched in calcium perovskite (CaPv) (compared to pyrolite). Recent calculations (Kawai & Tsuchiya, 2015) and sound-velocity measurements at lower-mantle pressures (Gréaux et al., 2019; Thomson et al., 2019) showed that the shear modulus of (cubic) CaPv is lower than previously calculated, which suggests that MORB has lower S-velocity than pyrolite in the lower-mantle. We, therefore, CaPv could possibly explain relatively strong low-velocity anomalies near the CMB.

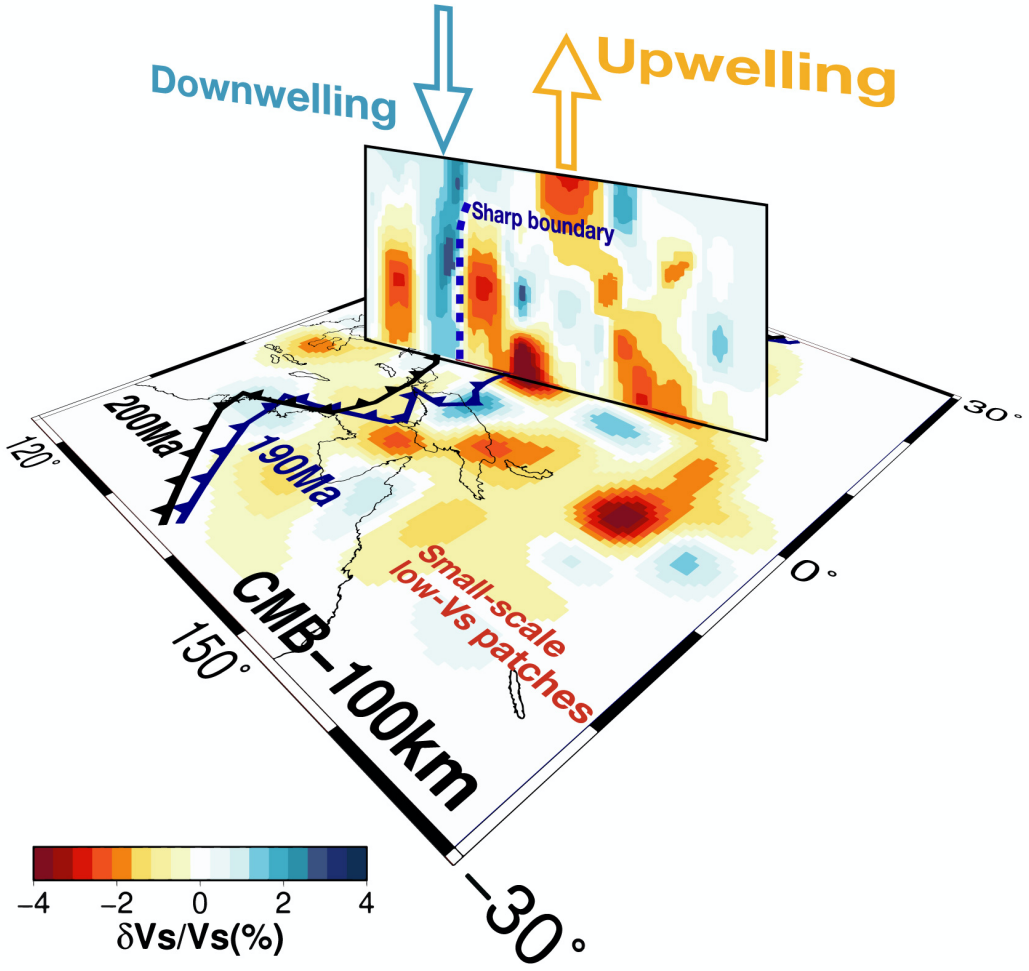

Figure 3.19 Schematic interpretation based on the S-velocity model obtained in this study. Small-scale low-velocity anomalies are inferred in the lowermost 200 km of the mantle. The high temperature material in the TBL is upwelling from the CMB in the eastern part of the study area. The Izanagi-plate boundary ~200 Ma (Young et al., 2019) is consistent with the location of the high-velocity anomaly beneath the Philippine Sea. Small-scale patch-like low-velocity anomalies could be interpreted as a cluster of upwelling thermal plumes, suggesting that the western Pacific LLSVP should be almost the same composition as in the lower mantle, taking into account previous geodynamical studies (Davies et al., 2012). Some upwelling plumes are continuous to 400 km above the CMB, and are continuous up to the surface as imaged in previous a whole mantle tomography model (French & Romanowicz, 2014). The sharp-sided boundary suggested by previous seismological studies (He et al., 2006; Takeuchi et al., 2008) could be produced by cold- (~450 K lower) material corresponding to the paleo-Izanagi-plate ~200 Ma. The cross-section A–A′ is shown in Fig. 3.3(b).

Geodynamical interpretation

A recent compilation of paleo-slab remnants found by seismic tomography and subduction histories has not identified the paleo-Izanagi slab at the lowermost mantle (van der Meer et al., 2017). However, geological evidence for subduction ~200 Ma at the eastern margin of Gondwana at the present western Pacific (Matthews et al., 2016; Müller et al, 2016; Young et al., 2019), together with recent seismological studies which found paleo-Izanagi slab in D″ beneath the northern Pacific (Suzuki et al., 2016), suggests that remnants of subducted paleoslabs could be found in the lowermost mantle beneath the Philippine Sea as well. The following features in our models suggest the presence of subducted paleoslabs in the lower mantle: (i) ~3 percent high-velocity anomalies just above the CMB, and (ii) the good agreement of the location of the former Izanagi plate boundary with the high-Vs anomaly beneath the Philippine Sea, while we found spatially separated high-Vs anomalies in the eastern part of our target region. As discussed above, since a high-Vs anomaly in D″ would be a low temperature anomaly, we interpret the high-Vs anomalies we found as subducted cold slab remnants. Thus, it is suggested that the subducted paleo-Izanagi plate sank into the lower mantle and could cool the outer core beneath the regions where the Izanagi-plate subducted on the surface ~160 to 200 Ma.

Our group's previous studies of D″ structure under the northern Pacific and central America (Suzuki et al., 2016; Borgeaud et al., 2017) also found distinct high-velocity anomalies above the CMB, which is in good agreement with the past location of subduction boundary of the Izanagi and Farallon plates, respectively. This thus implies that the subducted paleo-oceanic plate sank almost vertically in the lower mantle to the CMB beneath the circum-Pacific. Together with the fact that the low-velocity anomalies

continue almost vertically from the CMB in the lower mantle beneath the prominent hotspots (French & Romanowicz, 2014), vertical mantle flow is suggested to be dominant in the lower mantle.

The above discussion suggests that the style of convection in the lower mantle is controlled by plate tectonics on the surface. Based on the former plate motion reconstruction model (Young et al., 2019), ~70-Myr-old paleo-Farallon plate subducted ~180 Ma with ~10 cm/yr trench migration from east-to-west at present Central America, which would cause 'intermittent subduction' penetrating into the lower mantle (Borgeaud et al., 2017). At the present Aleutian, ~40-Myr-old paleo-Izanagi plate subducted ~200 Ma with at most ~4 cm/yr trench migration, which would cause avalanching stagnated slab ('sudden subduction') from the upper to lower mantle (Suzuki et al., 2016). At the present south-western Pacific ~100-Myr-old paleo-Izanagi plate subducted ~200 Ma with a maximum of ~2.0 cm/yr trench migration, which would cause constant penetration into the lower mantle (Goes et al., 2017; 'continuous subduction'). Such migration of the subduction region would affect the regional variation of the spatial distribution of slab remnants in D″. The volume of paleoslabs in D″ beneath Central America (Borgeaud et al., 2017) and beneath the northern Pacific (Suzuki et al., 2016) are ~1.4 and ~2.0 times the volume of the paleo-Izanagi slabs in D″ beneath the western Pacific inferred in this study (see Appendix C for volume estimation for the subducted slab in D″). Intermittent paleo-slab subduction such as beneath Central America could make the cooling rate of the outer core at the CMB both spatially and temporally heterogeneous. On the other hand, sudden subduction such as that beneath the northern Pacific could temporarily cool the relatively wide region of outer core, while continuous subduction such as beneath the western Pacific could locally and constantly cool the outer core.

The low-velocity anomalies found in this study (Fig. 3.3a) immediately above the CMB are smaller-scale, with a diameter of ~300 km, than those obtained by previous global tomography (see Fig. 3.4 for comparison with global tomography model). This suggests that the low-Vs region at the western Pacific LLSVP is an aggregate of smaller-scale low-Vs anomalies rather than a single large-scale one. The vertically continuous low-velocity anomalies to a height of at least 400 km above the CMB can be interpreted as upwelling flows from several spatially separated sources of hot material immediately above the CMB, called a 'plume cluster', rather than as a single large chemically distinct pile. Taking into account geodynamic studies (Davies et al., 2012) where plume clusters are produced mainly due to thermal effects rather than thermo-chemical effects (McNamara & Zhong, 2005), the western margin of the Pacific LLSVP would be explained by thermal effect. While there are various mantle convection studies have considered large-scale anomalies or present-day plume positions, to our knowledge there is no published their 3-D thermo-chemical mantle convection studies to compare results to high-resolution observations of LLSVP shape and plume position; we expect that future works could try to account for small-scale convection.

Plumes could be due to Rayleigh-Taylor instability in a thermal boundary layer of the type likely to occur in steady-state convection. Plume clusters are a common phenomenon in high Rayleigh number convection (Shubert et al., 2004), which suggests the existence of low viscosity material in the lowermost mantle beneath the western Pacific. This could be supported by the low viscosity layer suggested by Nakada et al., (2012) in the lowermost mantle based on an analysis of Chandler wobble and tidal deformation. Since a low viscosity in the lowermost mantle implies vigorous small-scale convection, material exchange between the core and mantle may be taking place.

Assuming that the whole Pacific LLSVP is almost chemically homogeneous, the Pacific LLSVP can be explained by primarily thermal effects. This implies that as the lowermost mantle would be chemically homogeneous, the geochemical reservoir could be the core rather than the lowermost mantle, as previous geochemical studies suggested that the core be a possible source of primordial material based on $^{3}He/^{4}He$ ratio (Porcelli & Halliday, 2001). However, there might be localized and smaller-scale chemical anomalies such as a ULVZ (ultra-low velocity zone; Yu et al., 2018).

Chapter 4 The 3-D S-velocity structure in D″ beneath the northern Pacific

4.1 Introduction

The D″ region is the lowermost several hundred km of the mantle immediately above the core–mantle boundary (CMB), and its base is in contact with the liquid iron alloy outer core. Since the D″ region is the thermal boundary layer (TBL) at the base of the Earth's mantle, and the solidus of its constituent materials is thought to be close to the mantle geotherm, vertical and lateral variations of temperature and chemical composition associated with the Earth's thermal evolution are expected (e.g., Garnero & McNamara, 2008; Kawai & Tsuchiya, 2009; Wysession et al., 1998). Previous studies have analyzed observed seismic waveforms and revealed lateral and vertical heterogeneity within D″ beneath Central America (e.g., Hutko et al., 2006; van der Hilst et al., 2007; Kawai et al., 2014), suggesting complex interaction between the paleo-subducted slab and the TBL beneath the subduction zone.

The D″ region, especially beneath subduction zones, provides clues for understanding the dynamics of the Earth's mantle, because thermally and chemically distinct slab materials can perturb the temperature and mantle flow. Hence, it is important to study the D″ region beneath subduction zones to investigate how slabs have subducted to the lowermost mantle. Lay & Helmberger (1983) and Young & Lay (1990) studied seismic structure in D″ in particular regions beneath the circum-Pacific, especially beneath the northern Pacific, and proposed 1-D S-velocity structure models, SLHO and SYLO, respectively, which have a positive velocity jump about 240 km above the CMB and a negative velocity gradient beneath the discontinuity. He et al. (2014) suggested an

850 km–thick low-velocity anomaly surrounded by a 210 km–thick high-velocity anomaly in D″ beneath Kamchatka on the basis of forward modeling of seismic waveforms. Sun et al. (2016) studied the lowermost mantle beneath Alaska using waveforms recorded at recently deployed USArray stations. They divided the study area into three subregions with lateral scales of ~15˚ (western, middle, and eastern parts). They reported that the western, middle, and eastern parts show a sharp D″ discontinuity with $V_S = 2.5$ percent, no clear evidence for a D″ discontinuity, and a gradual increase in δV_S, respectively. The number of earthquake sources used by the above studies is 10 for Lay and Helmberger (1983), 36 for Young and Lay (1990), 2 for He et al. (2014), and 3 for Sun et al. (2016), respectively, and waveform stacking, or waveform forward modeling were used.

It is desirable to infer the detailed S-velocity structure in a broad region beneath the northern Pacific by analyses using a large number of waveforms for many earthquakes and stations. Since USArray stations have finally moved to the easternmost part of the U.S.A. and earthquakes occur in a broad region in the western Pacific, waveform data which are relatively homogeneous in epicentral distance range and sample D″ over a long distance in the E–W direction (Fig. 4.1) are now available. This allows us to investigate S-velocity structure beneath the northern Pacific using a large amount of waveform data for western Pacific earthquakes recorded at North America stations (mainly the USArray).

Waveform inversion method are suitable for analysis of a dataset which consists of a large number of observed waveforms for many earthquakes. Waveform inversion can use not only S and ScS, but also later phases associated with a large velocity contrast in the D″ region (for example, Scd which has its turning point in D″; e.g.,

Borgeaud et al., 2016). Although these later phases are useful for studying structures in D″, they overlap with other phases at epicentral distances of more than ~80˚ and thus cannot be used by traveltime analysis.

4.2 Data and Methods

In the inversion for isotropic S-velocity structure using only transverse component, we apply the 3-D localized waveform inversion method to a dataset of ~19,000 records including overlapped phases that sample D″ well, and infer the isotropic Vs structure in the lowermost 400 km of the mantle beneath the northern Pacific. We invert the transverse component of broadband waveform data for 131 deep and intermediate earthquakes (orange stars in Fig. 4.1a, parameters in Table B2) with $5.5 \leq Mw \leq 7.3$ that occurred in western Pacific subduction zones using receivers in North America from the USArray and other networks (blue inverse triangles in Fig. 4.1a). The model determined by the inversion gives the 3-D S-velocity wave structure in the D″ region of the target area beneath the Northern Pacific and Alaska (Fig. 4.1b). The waveform data were downloaded from the Incorporated Research Institutions for Seismology (IRIS) data center. Fig. 4.1a shows event–receiver geometry with great circle ray paths used in this study. We deconvolve the instrument response, and apply a band-pass filter to the data, and construct a dataset for the passband from 0.005 to 0.08 Hz (i.e., for the period range 12.5 - 200 s). Note that the same filter is also applied to the synthetics and partial derivative waveforms. We then select records which include data for S, ScS, and other phases that arrive between them. Each record was corrected for the effect of the structure outside the target region by a time-shift that aligned the onset of the direct S

phase on the observed waveform with the onset of the direct S phase on the corresponding synthetic (Fuji et al., 2010). In this method, we pick the S-wave arrival and first peak for all synthetics and measure the time difference between them, Δt, to take the time window from $4\Delta t$ before the S-wave arrival to Δt after the S-wave arrival and compute the cross-correlation for this time window. The time of the peak of the cross-correlation is chosen as the time-shift for the static correction for each record. We discarded records for which the time-shift was greater than 10 s.

In contrast to inversion using only transverse component, the other dataset for anisotropic structure using both transverse and radial component and anisotropic Vs structure consists of ~9,000 transverse and ~9,000 radial component waveforms of ground velocity recorded at epicentral distances $70^\circ<\Delta<100^\circ$ from 131 deep- and intermediate-focus earthquakes that occurred around in the period from 2000 to 2015 (see Fig. 4.2 and Table B2 for details) to investigate the lowermost mantle structure beneath the northern Pacific. Note that we applied a Butterworth bandpass filter to the data and construct datasets of the inversion for the anisotropic structure for the passband 0.005 to 0.05 Hz (i.e., for the period range, 20-200 s). For the anisotropic structure, we use relatively longer period waveforms (down to 20 s), as a first step, compared to our group's recent work. Since we construct radial component dataset using same event-station pair as transverse component, we applied same time-shifts (Δt) for static correction (see section 2.2) as transverse component to radial component trace. We weighted the cut residual traces (observed trace minus synthetic trace) so that their maximum amplitudes were equal. We then applied a second weighting factor to the residuals to partially correct for the uneven azimuthal- and epicentral-distance distribution of the stations in our dataset (Fig. 4.2).

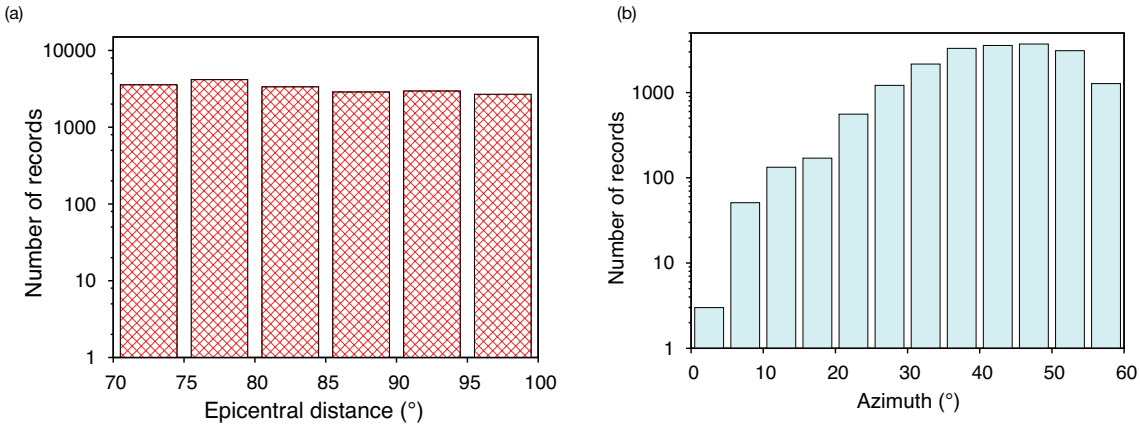

Figure 4.1 (a) The histogram of epicentral distance distribution for the data set used in this study. The vertical axis indicates the number of records and the horizontal axis indicates the epicentral distance in 5˚ segments. (b) The histogram of azimuthal distribution for the data set used in this study. The vertical axis indicates the number of records and the horizontal axis indicates the azimuth in 5˚ segments.

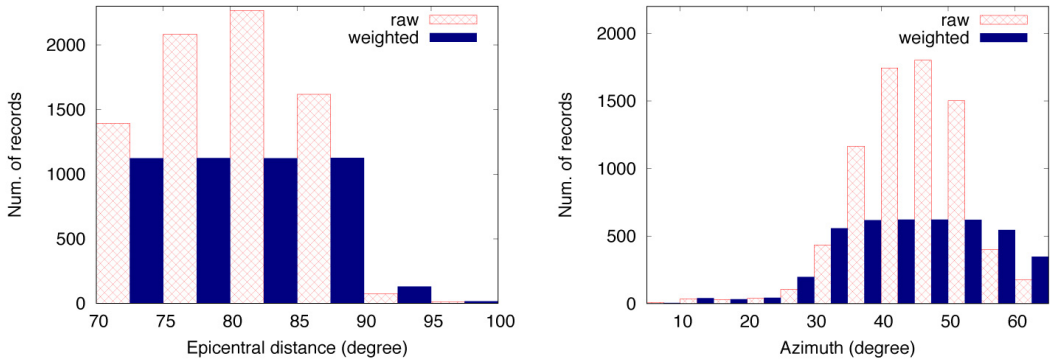

Figure 4.2 Distributions of azimuths (a) and epicentral distances (b) for the records used for the inversion. The original distribution is shown in red, and the weighted distribution is shown in blue. The records are weighted to homogenize the distribution of azimuths and epicentral distances.

4.3 Isotropic S-velocity structure

The target region for inversion for isotropic Vs structure is at latitudes between ~35˚ and 85˚ and longitudes between ~130˚ and 290˚ (Fig. 4.3), and depths from 0 to 400 km above the CMB. We divide the target region (studied volume) into 150 km x 150 km x 50 km voxels; there are thus 3,576 unknown model parameters. We conduct inversion using the first *n* basis vectors obtained by the CG method.

We choose the value of *n* that minimizes AIC. Table 4.1 show the variance and AIC value for each model. When we calculate AIC values, we define the empirical redundancy parameter α (see Appendix A of Kawai et al., 2014, for details and definitions). In this study the AIC value for α = 2500 is used. The total number of data points at 1 Hz sampling is 1,576,927. The AIC values in Table 4.1 are thus obtained using the number of independent data, ND = 1,576,927 / (2500 x 12.5).

Defining the variance of the data to be 100 percent, the variance (data minus synthetics) for the PREM synthetics without time shift is 133.4 percent. A further variance reduction to 76.2 percent is achieved by making the static corrections. The variance for model CG6, the model obtained for *n*=6, which minimizes AIC, is 70.9 percent, as shown in Table 4.1. The final model (CG6) achieved more than 25 percent variance reduction in the 'improvement window' (see section 2.3.3) which is the part of the seismogram that is most sensitive to the structure in D″

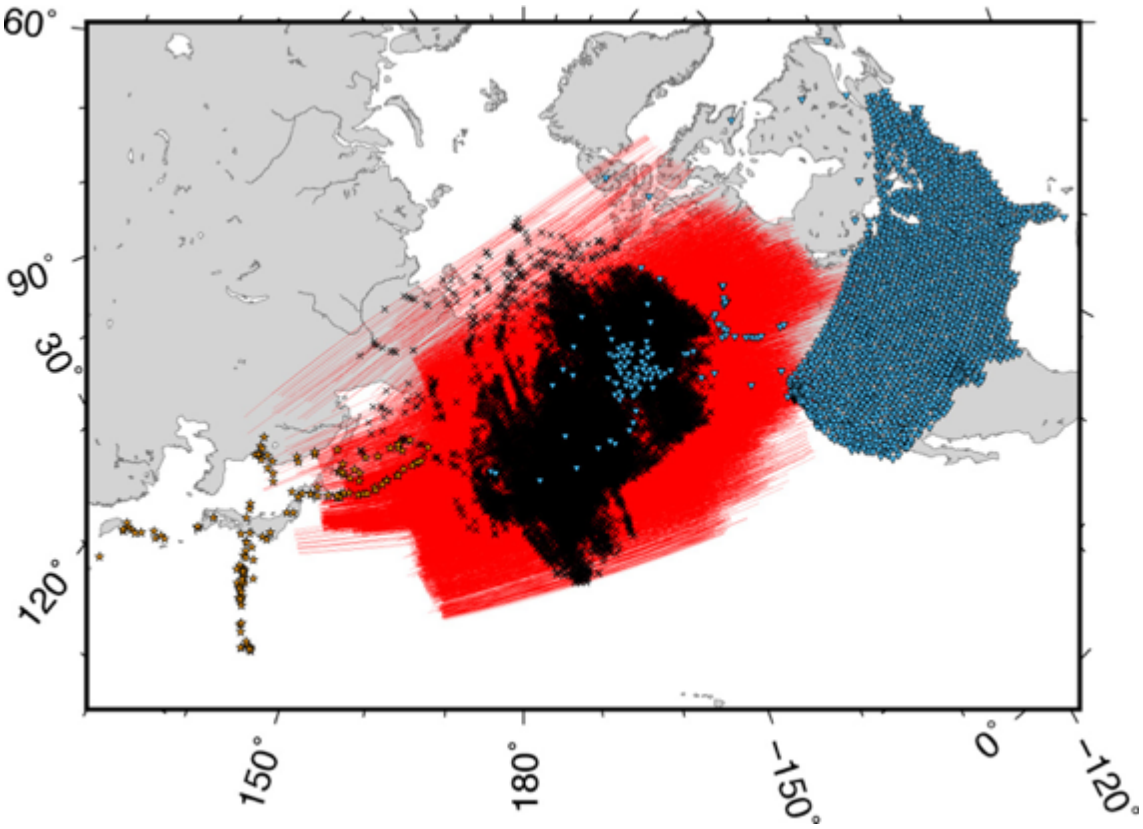

Figure 4.3 Event-receiver geometry for the data used in this study. The great circle paths which sample the D″ layer are shown in red, and crosses indicate the turning points at the CMB. Orange stars and blue reversed triangles show the stations in North America, and the 131 intermediate and deep earthquakes (Table B2), respectively.

Model	Variance (percent)	Variance for 'improvement window'	AIC (α=2500)
PREM	133.4		—
PREM with time shift	76.2	81.5	1620.3
CG6	70.9	56.2	1585.6

Table 4.1 Variance, variance for 'improvement window' and AIC for each model for the isotropic Vs structure using only transverse component.

Model CG6 is shown in Fig. 4.4. To examine the ability of our method to resolve the structure, we conduct synthetic resolution ('checkerboard') tests (Fig. 4.5). We confirm that for an ideal noise-free case the waveform inversion method and dataset used in this study can resolve the lateral heterogeneity well in all the depth ranges for the target region of this study. Compared to our group's previous studies (e.g., Kawai et al., 2014, Konishi et al., 2014), our present dataset allows us to resolve structure in D″ over a wider horizontal region (about 3,000 km in this study, as compared to about 1,000 km for Kawai et al., 2014). This facilitates an investigation of how the subducted slabs interact with ambient material in the lowermost mantle beneath the subduction zone.

The S-velocity model obtained by our inversion shows three types of features (Fig. 4.4):

(i) lateral high-velocity anomalies up to ~3 percent faster than PREM with a thickness of ~200 km whose lower boundary is ~150 km above the CMB. We can see a prominent sheet-like high-velocity anomaly labeled 'E' in Fig. 4.4 extending in the east-

west direction to the south of the Aleutian islands at 250-400 km above the CMB, and an arc-like high-velocity anomaly labeled ‘F’ in Figs. 4.4 and 4.16 from the southwest of the Aleutian islands through the east of the Kamchatka peninsula to Chukchi, the eastern tip of Siberia, at 150-250 km above the CMB. We also see two distinct high-velocity regions, labeled F′ and F″ respectively, from 250-400 km above the CMB, located directly above ‘F’. There is also a sheet-like high-velocity anomaly labeled ‘G’ in Figs. 4.4 and 4.16 beneath southern Alaska at 150-250 km above the CMB.

(ii) Prominent low-velocity anomalies ~2.5 percent slower than PREM labeled ‘H’ in Figs. 4.4 and 4.16 are located to the east of the Kamchatka peninsula with a thickness of ~100 km immediately above the CMB beneath the above-mentioned high-velocity anomalies.

(iii) A relatively thin (~300 km) weak low-velocity anomaly labeled ‘I’ in Figs. 4.4 and 4.16c which is continuous from the low-velocity anomalies beneath the east of Kamchatka peninsula immediately above the CMB to the far east of the Kuril Islands to at least 400 km above the CMB.

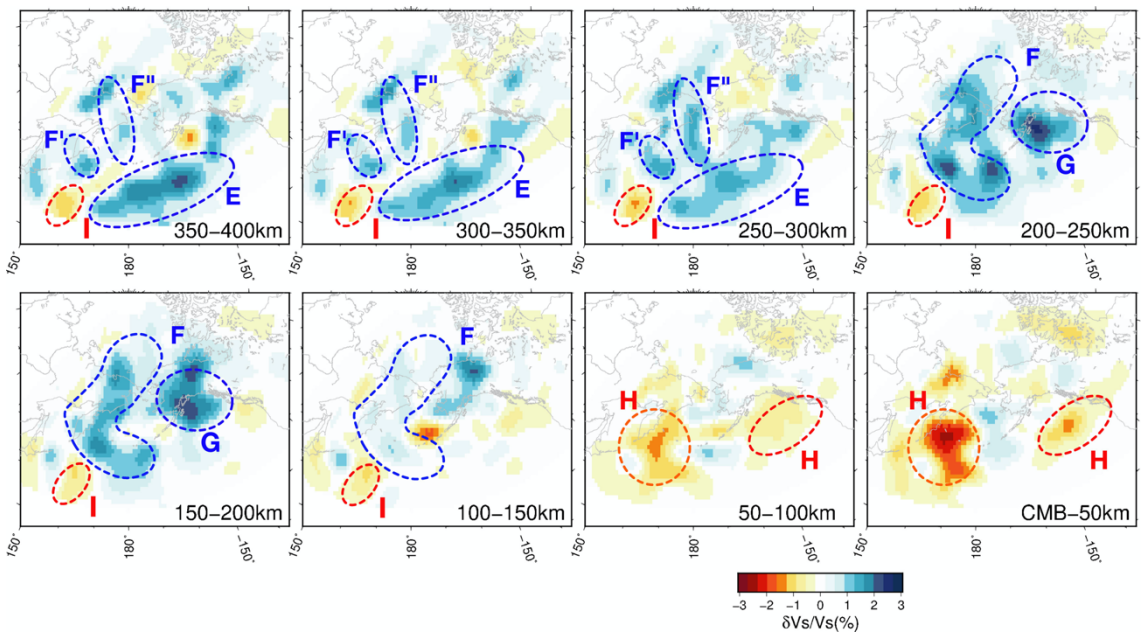

Figure 4.4 Results of the inversion (CG6) for the 3-D S-wave velocity structure in the lowermost 400 km of the mantle beneath the Northern Pacific and Alaska for each 50 km depth slice. PREM is used as the reference model.

4.3.1 Resolution and validation check

In our inversion process, the target region is only in the lowermost 400 km of the mantle and the structure for shallow regions is assumed to be the anisotropic PREM model (Dziewonski & Anderson 1981). In order to examine the possible effects of shallow structure, such as the subducting Pacific and Philippine Sea slabs, on the inversion results, we also checked the independence of the partial derivatives for perturbations in such regions from those in the target region in the lowermost mantle (Fig. 4.6). This indicates that if we had only one station and one record then it would be impossible to resolve the tradeoff, but with a total of thousands of records (many stations for many events) the inversion algorithm can resolve the tradeoff with only a small

uncertainty. As shown in Fig. 4.6, the dataset in this study is large enough to effectively eliminate the trade-off between shallow structure and structure in the target region when all seismograms and all stations are used.

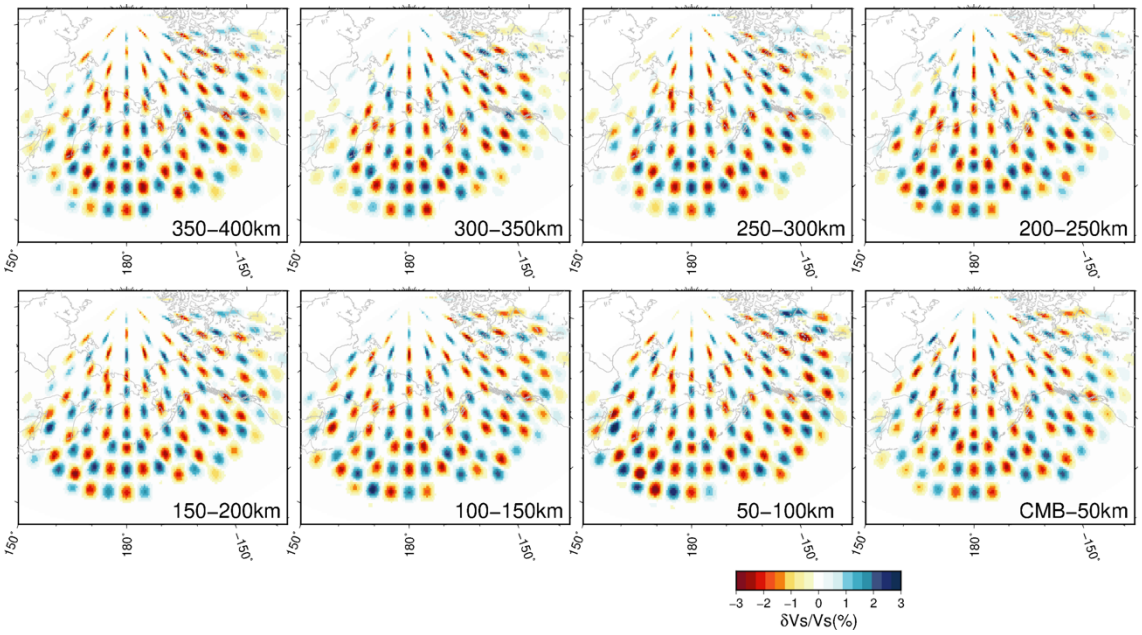

Figure 4.5 Checkerboard test. (a) The input synthetic model. (b) Recovered models for checkerboard patterns of the heterogeneities for each depth.

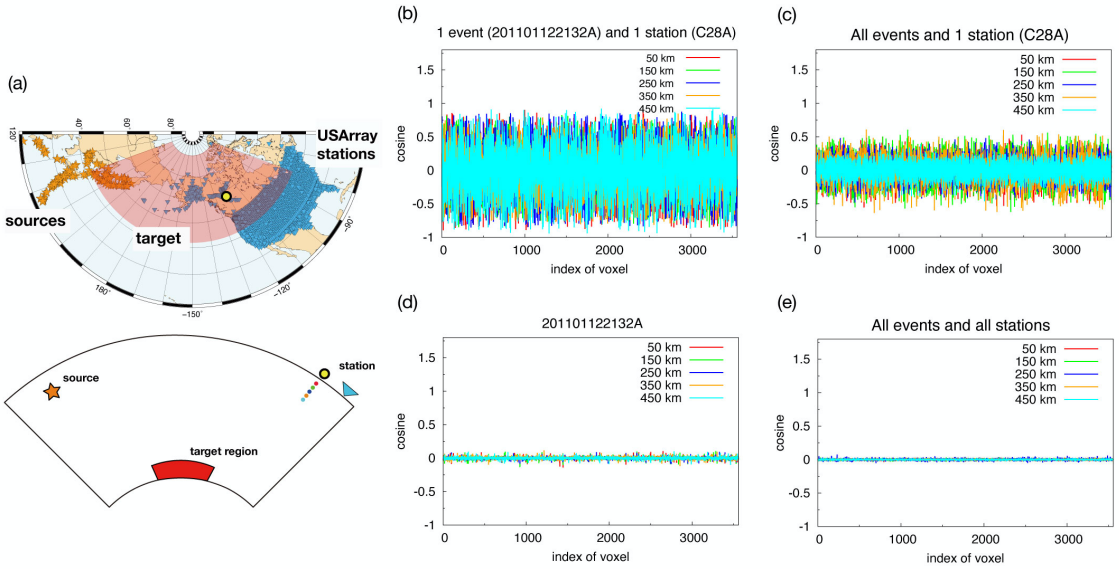

Figure 4.6 Panels showing the value of the cosine of the angle between the vector of partial derivatives for the *i*-th point in the target region and the vector of partial derivatives for the depth shown by each colored region at shallow depth. Panel (a) shows the geometry. Panel (b) is for one waveform for one event, panel (c) is for all waveforms for one event but one station, panel (d) is for one event for all stations, and panel (e) is for all events for all stations. The number of waveforms used in the four panels is 1, 7, 576, and 19,942, respectively.

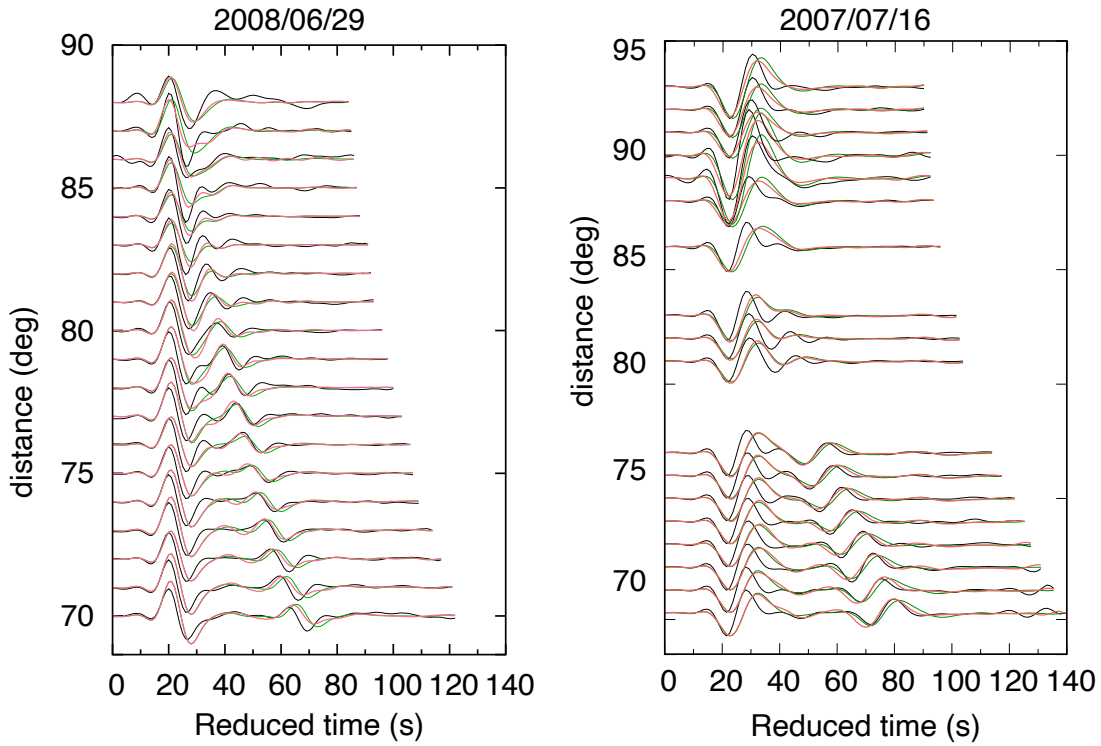

Figure 4.7 Quality control stacks. Record sections for the two events #35 and #49 in Table B2. The traces are stacked every 1˚ of epicentral distance (the time-shifts used in the inversion are applied to the observed data). Observed traces are shown in black. The top row shows synthetics for the initial models PREM (green), and final model (pink).

4.4 Isotropic S-velocity structure using two horizontal components

As a second step, we conduct waveform inversion using both the transverse and radial components to infer the more detailed isotropic shear velocity structure in the lowermost mantle beneath the northern Pacific. The azimuthal- and epicentral- distance distribution of the stations is shown in Fig. 4.2. The data are filtered in the period range of 12.5 to 200 s using a Butterworth bandpass filter. We conducted inversions with respect to PREM except for topmost 300 km of the outer core. We use the KHOMC model (Kaneshima & Helffrich, 2013) as the initial 1-D model for the

topmost 300 km of the outer core.

Model CG6 is shown in Fig. 4.8. Our obtained model is generally consistent with inversion result using only transverse component (Fig. 4.4). This is because our dataset consists of a large amount of seismic waveform data whose incidence angles in D″ cover a wide range (Fig. 4.10). We use waveform data which are relatively homogeneous in the epicentral distance range 70–100˚ (Fig. 4.1). As shown in Eqs. A.23, A.24, A.43, and A.44, the group velocities of SH and SV propagating in anisotropic media show dependence on the incidence angle. In this study, we infer the 3-D structure of the effective shear moduli.

The synthetic resolution check (Fig. 4.5) shows improvement from using radial component. The checkerboard pattern at the west and east edge of the target region were improved from recovered model using only transverse component. This improvement is contribution from SKS phase, which piercing points to the CMB are mostly at the rim of the target region.

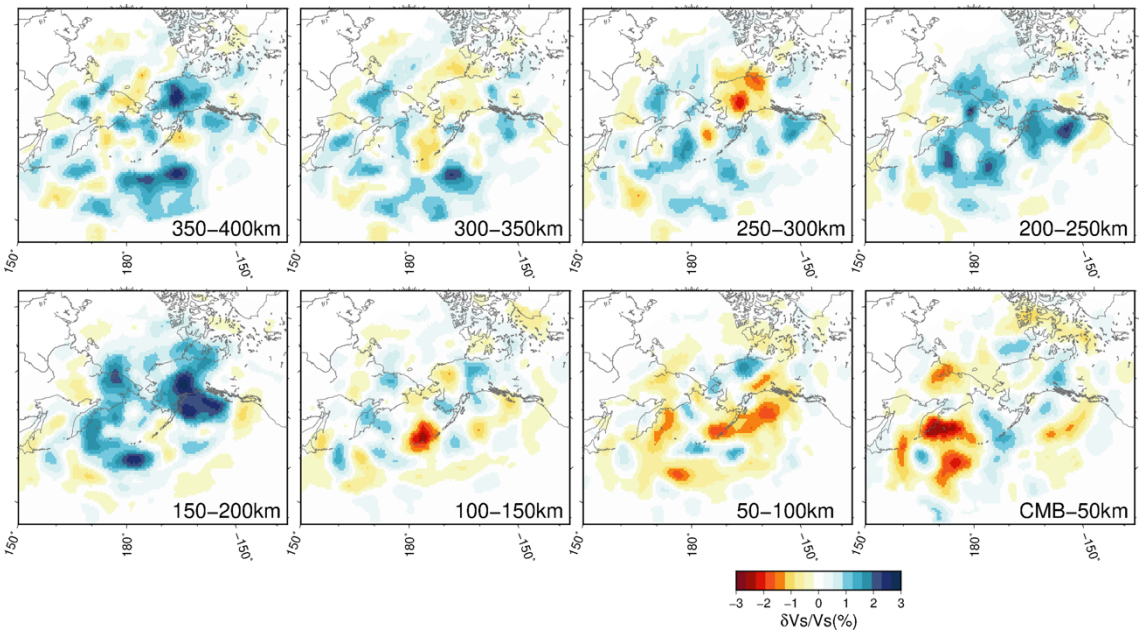

Figure 4.8 Results of the inversion (CG6) for the 3-D S-wave velocity structure in the lowermost 400 km of the mantle beneath the Northern Pacific and Alaska for each 50 km depth slice. Same as Fig. 4.4 except that we used not only transverse component but radial component.

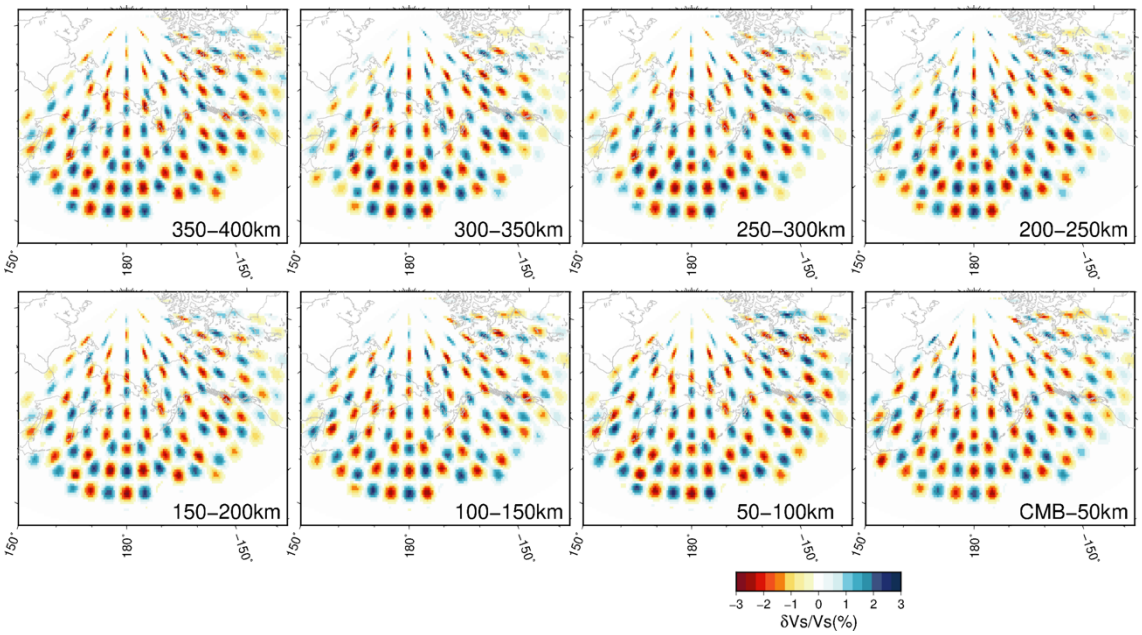

Figure 4.9 Recovered models for checkerboard patterns of the heterogeneities for each depth. The input synthetic model is shown in the left panels.

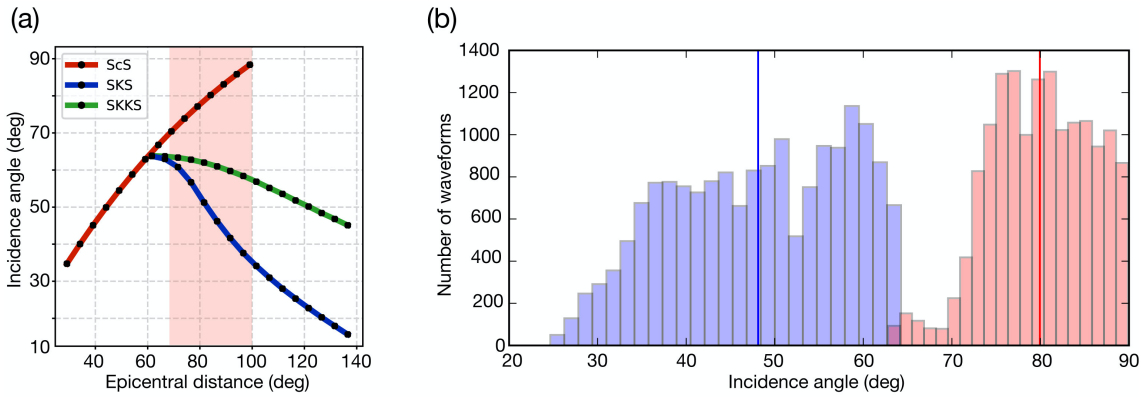

Figure 4.10 Incidence angle in D″. Left panel (a) shows the incidence angle computed for a given epicentral distance for ScS, SKS, and SKKS phases. The source depth is 500 km. The pink area indicates the epicentral distance range of our dataset. Right panel (b) shows the histogram of incidence angle for ScS and SKS phases for our dataset. Red and blue lines show the average incidence angles of the ScS and SKS phases of our dataset.

4.5 Anisotropic structure

Anisotropy is considered to be present where there is shear stress and/or laminar structure at thermal boundaries of mantle convection such as the top and bottom of the mantle and the mantle transition zone (e.g., Karato, 1998; Montagner, 1999). Taking into account rheology of mantle rocks, geodynamical mantle convection models predict the seismic anisotropic structure associated with deformation-induced CPO (crystallographic preferred orientation) under high shear stress due to the collision of subducted slabs with the CMB (Karato, 1998; Maupin & Park, 2008; McNamara et al., 2005). It is important to illuminate anisotropic structures in the D″ region from seismic observations as well as average (isotropic) velocity structures since it could provide information on changes in mantle flow mechanisms and/or flow direction as well as variations in temperature.

Several approaches have been used to infer the anisotropic structure in the lowermost mantle. Studies of the Earth's free oscillations have suggested the existence of anisotropy ($\delta\xi > 0$) in the lowermost mantle as well as the upper mantle and the mantle transition zone (Montagner & Kennett, 1996), which suggested that horizontal flow is dominant. Waveform inversion of long-period shear waves (Panning & Romanowicz, 2004, 2006) or travel-time tomography (Kustowski et al., 2008) showed for global (more than 2000 km) scale transversely isotropic (TI) structure in the lowermost mantle, which implies the variation of large-scale mantle flow. Most studies on the seismic anisotropy in D″ have considered the apparent travel-time differences between radial (SV) and transverse (SH) components (shear wave splitting; SWS) or conducted forward modeling of radial and transverse waveforms for anisotropic structure. Several previous studies on SWS have reported that the SH velocity is faster than the SV velocity in the D″ region underneath circum-Pacific (see Nowacki et al., 2011; Romanowicz & Wenk, 2018, for a review), which was interpreted as horizontal flow.

Kawai & Geller (2010) showed that, due to the boundary condition of zero tangential traction at the CMB, resolution of the anisotropy (i.e., of the values of the TI elastic constants L and N) within about one wavelength of the CMB is effectively impossible. Their result pointed the limitations of ray theory, which is an infinitely high-frequency approximation. Hence, it is desirable to investigate the structure of the lowermost mantle using full-waveform analysis with large dataset consist of numerous waveforms from multiple sources and receivers.

Recently, dense seismic arrays such as the USArray, which includes many portable seismic stations that have steadily been moved eastward to cover the entire contiguous area of the United States, provides high enough quality data for densely

sampling localized regions in D″. Hence, it is to be desired that regionally detailed seismic tomography using full USArray data is developed to obtain better resolution on the anisotropic structure in D″.

The D″ region under the Northern Pacific (NP) is of particular geodynamical interest, because the paleo- and present Pacific plates have been subducting beneath the northwestern margin of Laurentia since at least ~250 million years ago (Müller et al., 2016), which implies that paleoslabs could have reached the D″ region. Suzuki et al. (2016) inferred the detailed three-dimensional (3-D) isotropic S-velocity structure in the lowermost 400 km of the mantle analyzing full USArray data and suggested possible evidence for the interaction between subducted cold slab and hot TBL. They showed a prominent laterally wide (~1000 km scale) ~100 km thick high-Vs, interpreted as paleoslabs and prominent low-Vs anomaly blocks (<500 km horizontally and >100 km vertically) adjacent to the paleoslabs, interpreted as hot material of developed TBL. Thus, it is essential to resolve 3-D anisotropic structure with ~500 km horizontal scale and ~100 km vertical scale in order to put additional constraints on geodynamical models.

Here, we performed waveform inversion to infer the 3-D variation of the values of the TI elastic constants such as isotropic Vs and ξ ($\equiv L/N$) straightforwardly, using the full USArray data to obtain dense coverage of the D″ region beneath the NP. Inversion of waveforms recorded by USArray directly for TI elastic constants such as L and N at a given location enables direct comparison with those predicted by mineral physics studies, while the SWS is observed as the integral along the path with ray approximation. Also, when the SWS is interpreted, the effects of the difference of incident angle of shear waves at the CMB are usually neglected under the

assumption where the shear waves propagate horizontally in the lower mantle. The use of relatively short-period (20–200 s) radial and transverse components data for the S/ScS time window which is sensitive to the D″ structure makes it possible to image smaller-scale structure with finer resolution than previous tomography or global waveform inversion studies.

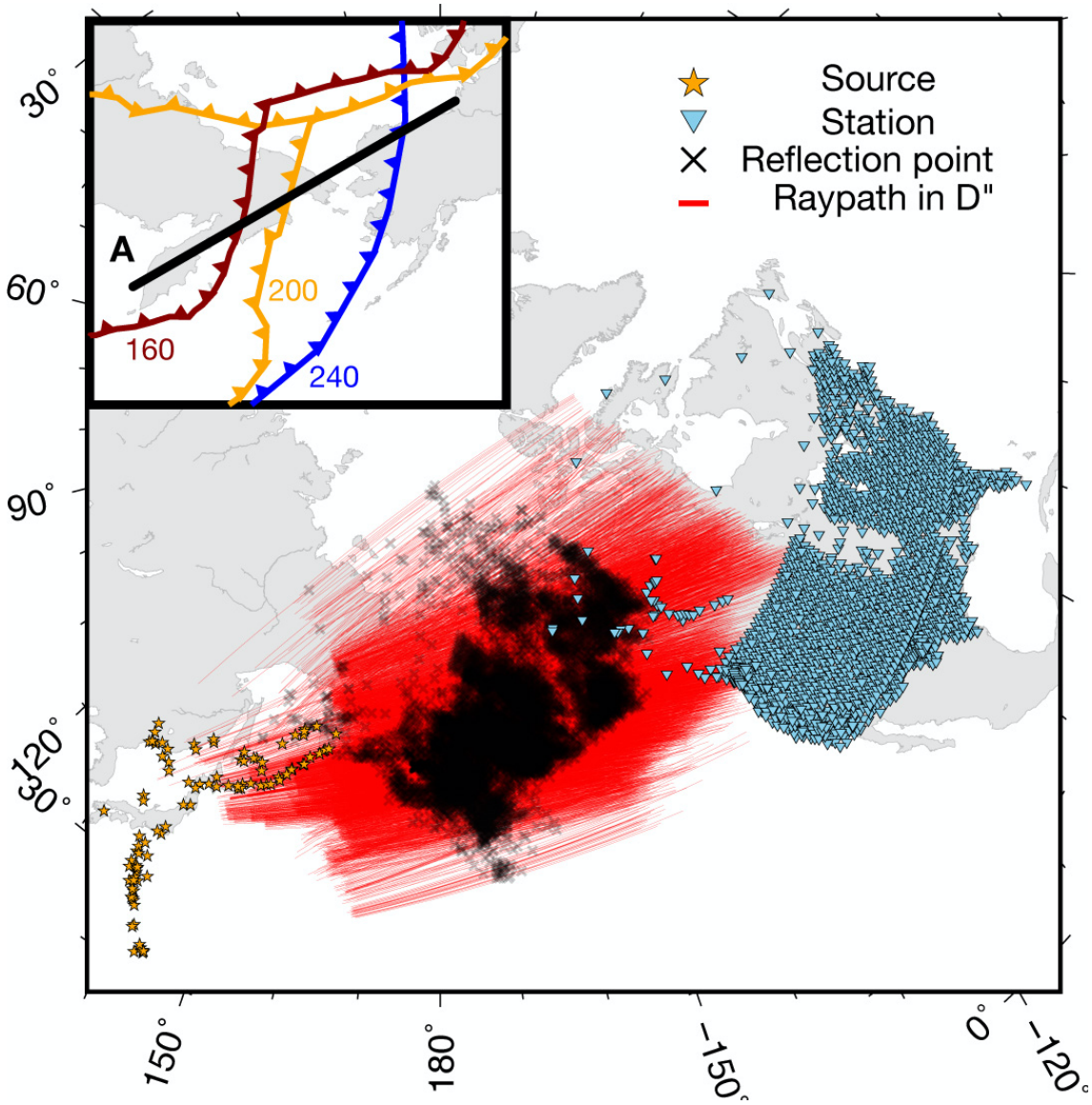

Figure 4.11 The great circle paths which sample the D″ layer are shown in red, and black crosses indicate the reflection points of ScS phase at the CMB. Light blue reversed triangles and orange stars show the stations of the USArray, CNSN, CANOE, and other seismic networks in North America, and the 134 intermediate and deep earthquakes in and around Japan (Table B2), respectively. The inset shows the location of the cross sections presented in Fig. 4.18 and the location of the plate boundary at 260 to 160 Ma from paleo-plate reconstruction model (Young et al., 2018).

4.5.1 Obtained 3-D TI structure

The obtained final models for isotropic V_S and ξ are shown in Fig. 4.12. As discussed above, ξ in the lowermost ~100 km of the mantle is hard to be resolved due to the solid-liquid boundary conditions at the CMB. To indicate this uncertainty the lowermost 100 km of the mantle are shaded in Fig. 4.12 (b). The perturbation pattern of obtained final model for isotropic *Vs* is generally consistent with our previous isotropic S-velocity model inferred only using the transverse component. We also conduct several validations and confirm the resolution of our models presented in the section 4.6.

The 3-D obtained anisotropic ($\delta\xi$) structure in Fig. 4.12(b) shows following 3 key features: (1) We found negative anisotropy ($\delta\xi < 0$) region which has around 500 km horizontal scale at 300-400 km above the CMB beneath Alaska. (2) Laterally wide (~1000 km scale) positive anisotropy ($\delta\xi > 0$) regions are dominant at 100-300 km above the CMB. (3) Observed magnitude of positive anisotropy ($\delta\xi > 0$) grows with depth (~2 percent at 300-400 km above the CMB to ~4 percent at 100-200 km above the CMB).

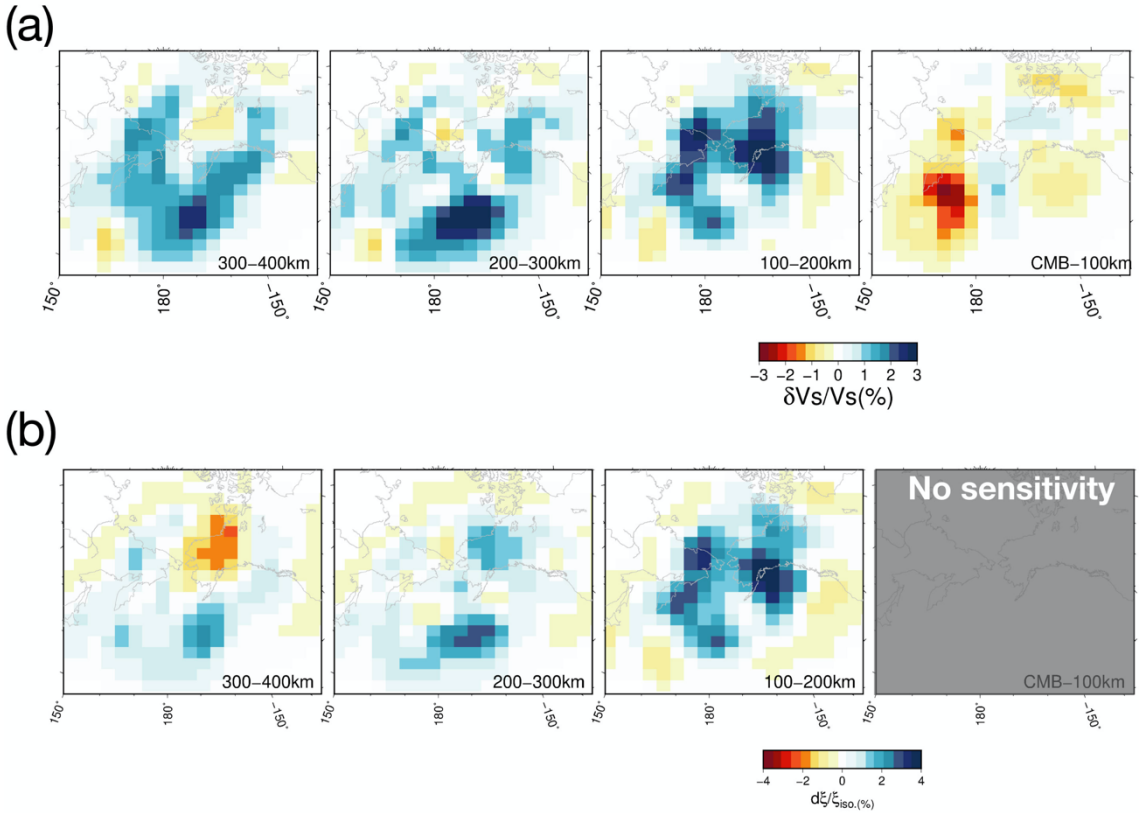

Figure 4.12 Results of the inversion (CG6) for the 3-D (a) isotropic S-velocity and (b) anisotropic structure. (a) The for panels show the results of the inversion of the isotropic S-velocity parameter *Vs* for the four depth layers from 400 km above the CMB to the CMB, with the lateral average of the 3D perturbation set to zero in each layer. The perturbation is relative to the initial 1D model PREM. (b) Same as (a), except that the obtained model of the anisotropic parameter ξ. Perturbation to ξ ($\delta\xi$) for the larger from 100 km above the CMB to the CMB (gray area) was not inferred because of the lack of spatial resolution due to the boundary condition where tangential tractions are zero at the CMB between the solid mantle and the fluid outer core (see Kawai & Geller, 2010 for details).

4.5.2 Validation of inferred model

To examine the ability of our method to resolve the structure in the target region, we conduct synthetic resolution ('checkerboard') tests (Fig. 4.13). We confirm that for an ideal noise-free case the waveform inversion method and dataset used in this study can resolve the lateral heterogeneity for the anisotropic (TI) structure well in all the depth ranges for the target region of this study. As an additional test of the validity of the Born approximation for inversion for S-velocity in D″, we show a "nonlinear checkerboard test" in Fig. 4.15. The input model is the same as for the linear case. Synthetic seismograms for this model were computed using full 3-D waveform calculation (SPECFEM3D_GLOBE; Komatitsch & Tromp, 2002a, b; Komatitsch et al., 2015). Because of heavy computational requirements with increasing maximum frequency, we computed synthetics down to ~13 s and filtered them with a bandpass filter between 20 and 200 s. The result (Fig. 4.15) shows that the inversion using the Born approximation underestimated the absolute amplitude of the perturbations by about 20 percent (~2.5 percent for the inversion result, compared to the 3 percent perturbation of the input pattern) but that the pattern of high- and low-velocity anomalies was reasonably well recovered. To verify the static corrections used to remove the effects from outside the target region, we conduct the two tests shown in Figs. 4.15 and 4.16, respectively. Fig. 4.15 shows that the partial derivative kernel for the structure in the target region is nearly completely independent from that for the structure in the shallow mantle. In Figs. 4.16 and 4.17, we present the inversion result obtained using isotropic PREM, and anisotropic PREM with the low-Vp layer at the topmost 300 km of the outer core as the starting model, respectively. This result appears to be consistent with the inversion result obtained using anisotropic PREM as the starting model shown in Fig. 4.12 and this suggests that

the starting model outside the target region has a relatively small effect on the results of the inversion, although the absolute amplitudes of the velocities differ somewhat. In the near future, we will perform static correction using 3-D mantle tomography model including anisotropic structure such as SEMUCB (French & Romanowicz, 2014) to evaluate quantitatively the effects from regional upper mantle anisotropy structure. The simultaneous inversion for the 3-D anisotropic structure in D″ (0—400 km above the CMB) and in the upper mantle is also a topic for future studies.

Model	Variance (percent)	Variance for 'improvement window'	AIC (α=1000)
PREM	152.1		—
PREM with time shift	86.2	90.1	3040.5
CG6	80.9	58.8	2896.3

Table 4.2. Variance and AIC for each model. Table 4.2 shows the improvement in the fit of the 3-D synthetics to the data, and AIC obtained using our 3-D models. For the initial model PREM, the fit of the initial synthetics to the data (152.1 percent) is reduced to 86.2 percent after time-shifting the data to correct for 3-D structures above the target region in D″. Inversion of the corrected data yields synthetics for the final 3-D model with a fit of 80.9 percent, an improvement of 5.3 percent over the fit of the initial synthetics for PREM with time-shifts. We also compute the variance for 'improvement window' which is the time window where waves sensitive to structure in D″, and variance reduction for 'improvement window' is 31.3 percent.

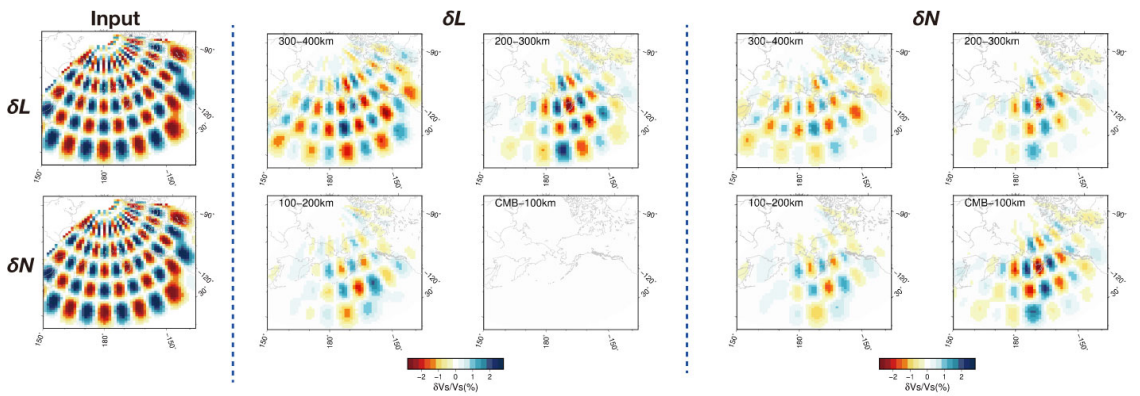

Figure 4.13 Linear checkerboard test. The input pattern for the layer 400-350 km above the CMB is shown on the left. Input patterns for the next layer (350-300 km) has the sign of all the anomalies reversed, and so on for each successive layer. The dataset and the number of CG vectors for the checkerboard test is the same as for the actual inversion (i.e., CG6). This result shows that we can nominally resolve almost all the voxels in the target region.

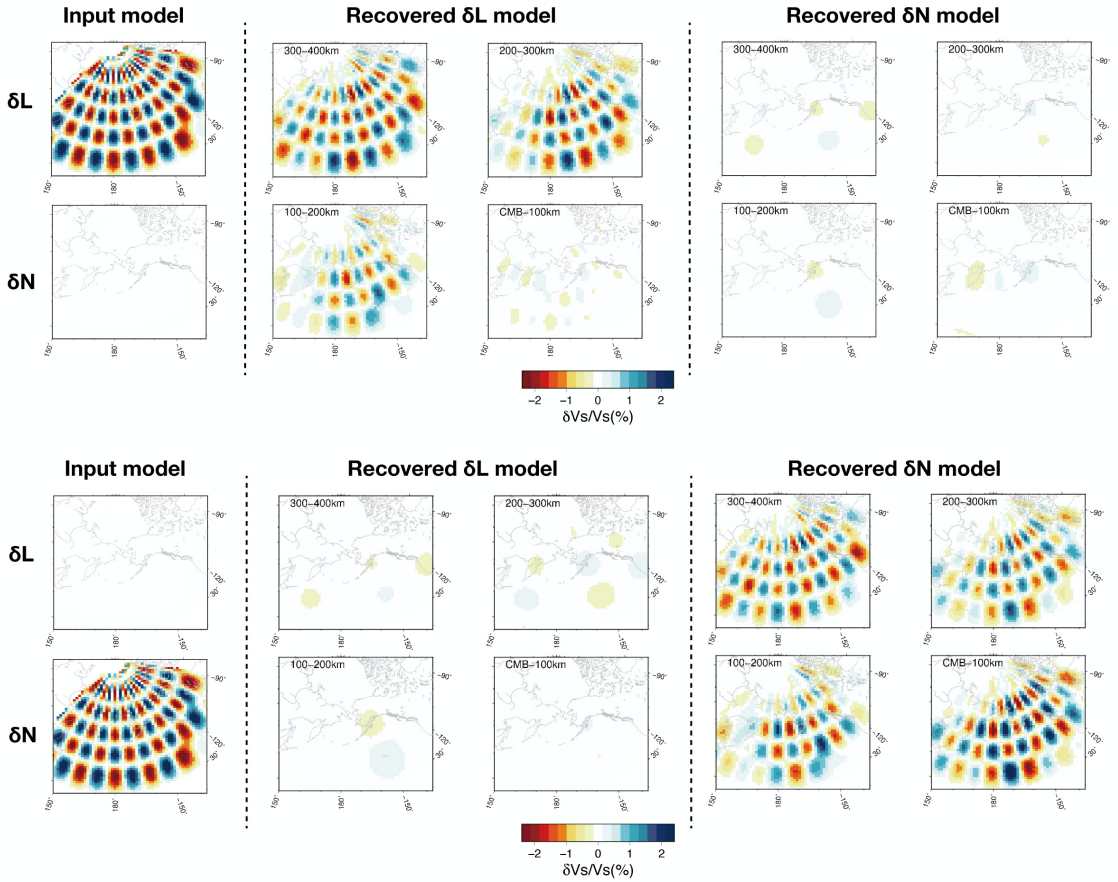

Figure 4.14 Tradeoff between *L* and *N*. The input pattern for the layer 400-350 km above the CMB is shown on the left. Input patterns for the next layer (350-300 km) has the sign of all the anomalies reversed, and so on for each successive layer. The dataset and the number of CG vectors for the checkerboard test is the same as for the actual inversion. This result show that we can nominally resolve almost all the voxels in the target region with less tradeoff.

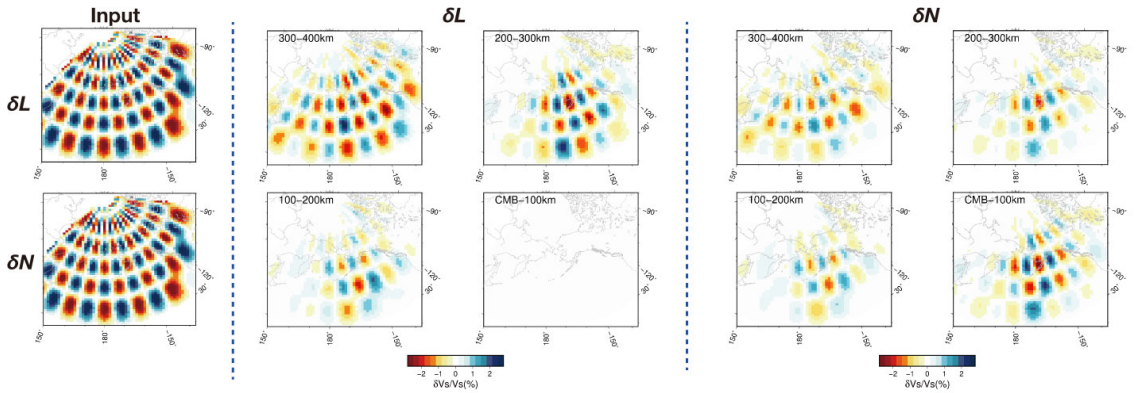

Figure 4.15 Nonlinear checkerboard test. In order to investigate the validity of the Born approximation used in our inversion, we conduct a "nonlinear checkerboard test" by using input synthetics computed using full 3-D wave calculation (SPECFEM3D_GLOBE; Komatitsch and Tromp, 2002a; Komatitsch and Tromp, 2002b; Komatitsch et al., 2015). (a) Input checkerboard pattern used for the full 3-D wave calculation, with 3 percent heterogeneities of dimension 10˚ x 10˚ laterally x 100 km vertically. The synthetics for this input pattern are accurate down to a period of ~13 s, and filtered with a Butterworth bandpass filter between 20-200 s. (b) Recovered pattern after inversion using the partial derivatives computed using the Born approximation. Note that the maximum amplitude shown by the color scale in panel (a) (3 percent) differs from that in panel (b) (2 percent). Fig. 4.14 shows that inversion using the Born approximation recovers reasonably well the pattern of high- and low-velocity anomalies, although the amplitude of perturbations is subject to some uncertainties.

In order to examine the possible effects of shallow structure, such as the slab beneath North America, on the inversion results, we also checked the independence of the partial derivatives for perturbations in such regions from those in the target region in the lowermost mantle (Fig. 4.16). As shown in Fig. 4.2, the dataset in this study is large enough to effectively eliminate the trade-off between shallow structure and structure in the target region when all seismograms and all stations are used.

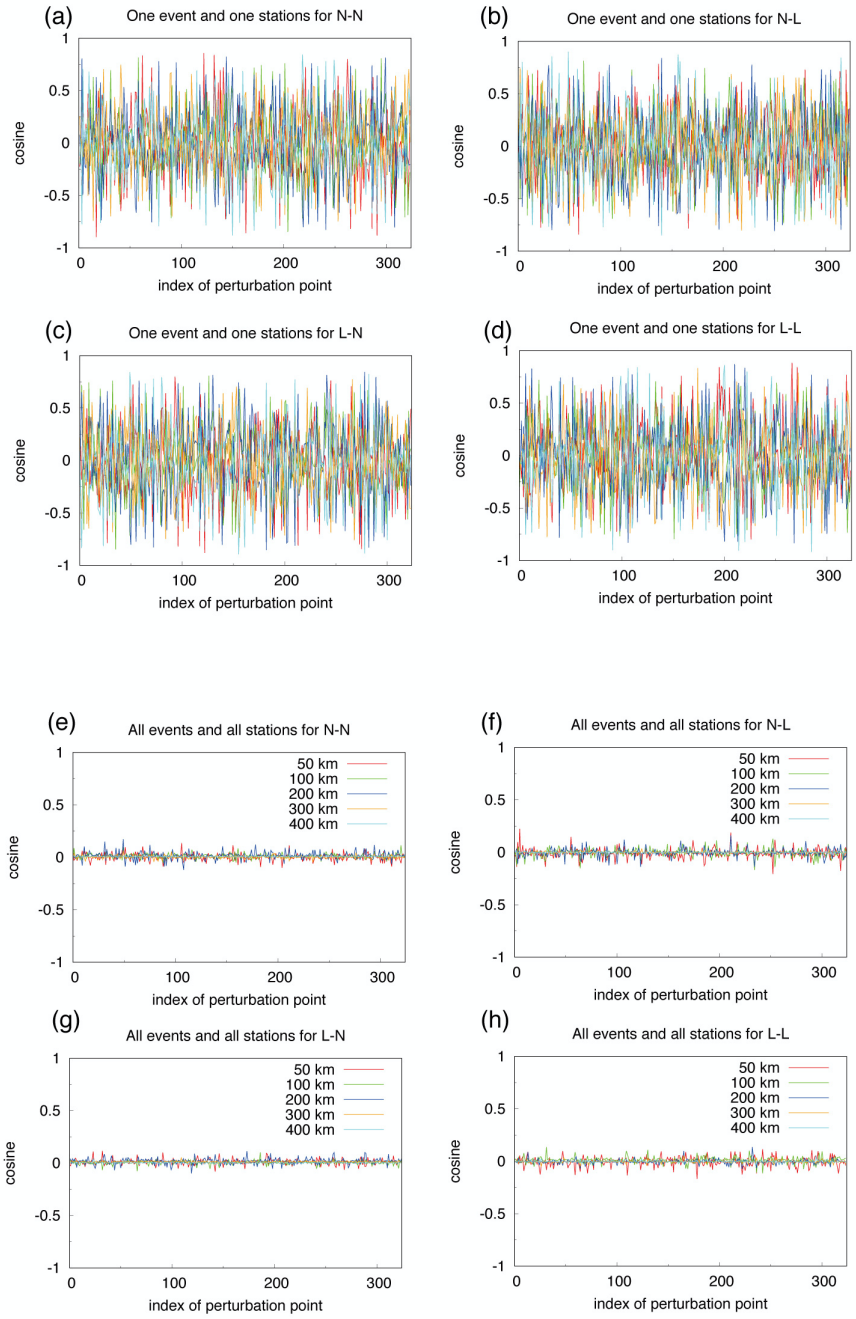

Figure 4.16 Tradeoff with shallow structure. Cosine of the angle between the vector of partial derivatives for each of the 624 voxels in the target region (D″) and the vector of partial derivatives for each of the 5 voxels in the upper mantle at 30˚N, 110˚W and 50-450 km depth. The legend for each panel is the same as the one shown in panel d). The four panels indicate an increasing number of records in the partial derivative vectors: a) one station, one event (1 record); b) one station, all events (4 records); c) all stations, one event (381 records); d) all stations, all events (19,800 records).

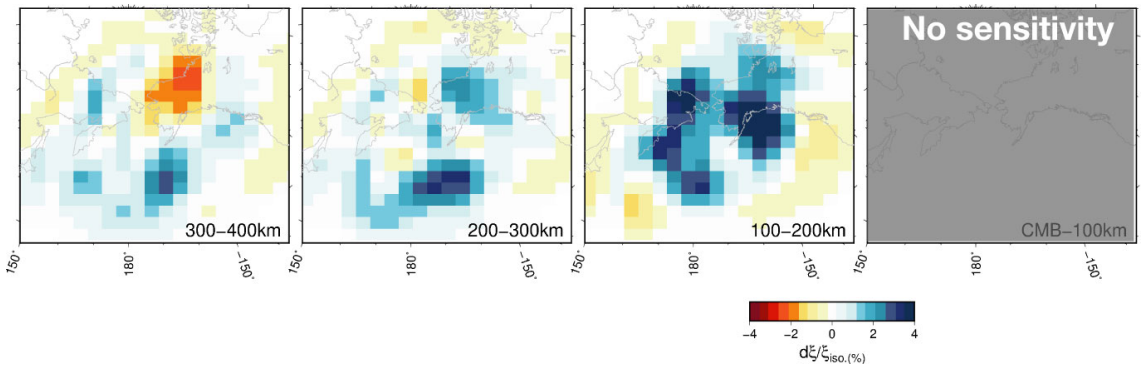

Figure 4.17 Same as Fig. 4.12 except that the initial model is isotropic PREM.

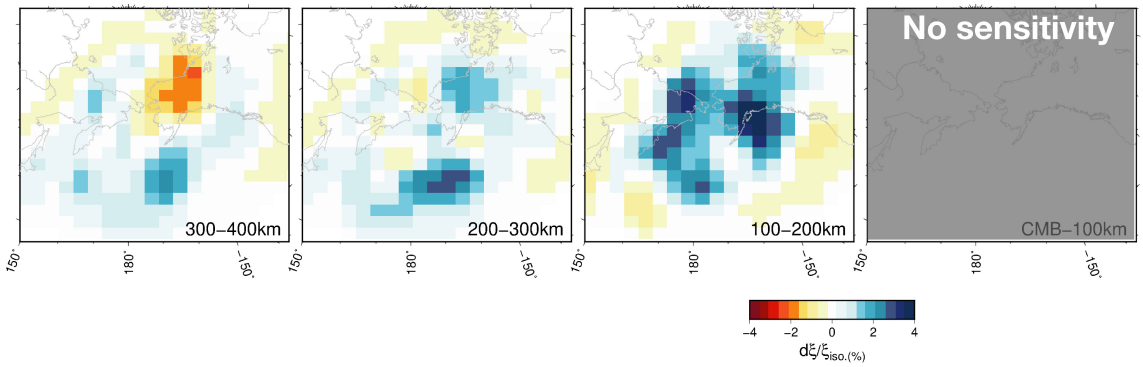

Figure 4.18 Same as Fig. 4.12 except that the initial model is anisotropic PREM with the low-velocity layer at the top of 300 km of the outer core (Kaneshima & Helffrich, 2013).

4.6 Discussions and geophysical implications

4.6.1 Isotropic S-velocity structure

Our isotropic *Vs* model (Fig. 4.4) generally agrees with global tomographic models (e.g., French & Romanowicz, 2014, 2015), but has finer resolution. Recent waveform forward modeling studies (He et al., 2014; Sun et al., 2016) estimated depths of the D″ discontinuity of ~200 km and ~250 km above the CMB beneath Kamchatka and the Northern Pacific, respectively, which are consistent with the depth of the significant high-velocity anomalies between 200–300 km above the CMB in our model (Fig. 4.4). Since the S-velocity anomalies can be primarily attributed to effects of temperature, the high- and low-velocity anomalies indicate colder and hotter than average temperature at each respective depth. Cross-section C–C′ in our model shows that high-velocity anomalies (i.e., relatively cold material) lie at ~250 km above the CMB and that low-velocity anomalies (i.e., relatively hot material) are below the high-velocity anomalies immediately above the CMB. These high-velocity anomalies may be enhanced by the Mg-Pv to Mg-pPv phase transition, because a cold geotherm makes the positive velocity jump associated with the phase transition clearer (Kawai and Tsuchiya, 2009).

It has been suggested that some slabs accumulate and stagnate at the mantle transition zone beneath the subduction region. The stagnant slab beneath the Aleutian subduction zone, a part of the target region of this study, was found to be stagnant at the bottom of the transition zone (Gorbatov et al., 2000). If subducted slabs were stagnant in the transition zone, paleosubducted and stagnant slabs would have begun to avalanche and descend into the lower mantle in about 10 million years (Pysklywec & Ishii, 2005), and would have finally reached the CMB. Whether they stagnate or penetrate the 660 km discontinuity, subducted slab materials would descend to the lower mantle

and reach the CMB. Hence, the high-velocity anomalies shown in our model could be interpreted as the paleo-subducted cold slab. If the subduction rate is about ~1.2 cm/year in the lower mantle, it would take about 200 million years for slabs to descend from the surface to the CMB in this region. Taking this into account, the sharp high-velocity anomalies in D″ found in our model could be remnants of the paleo-subducted Izanagi plate slab (e.g., Müller et al., 2016). The velocity contrast may be enhanced by the Mg-Pv to Mg-pPv phase transition, due to the low temperature. Two high-velocity anomalies (labeled F′ and F″, respectively) continuous from the slab remnants to 400 km above the CMB are found in cross-section C–C′ in our model.

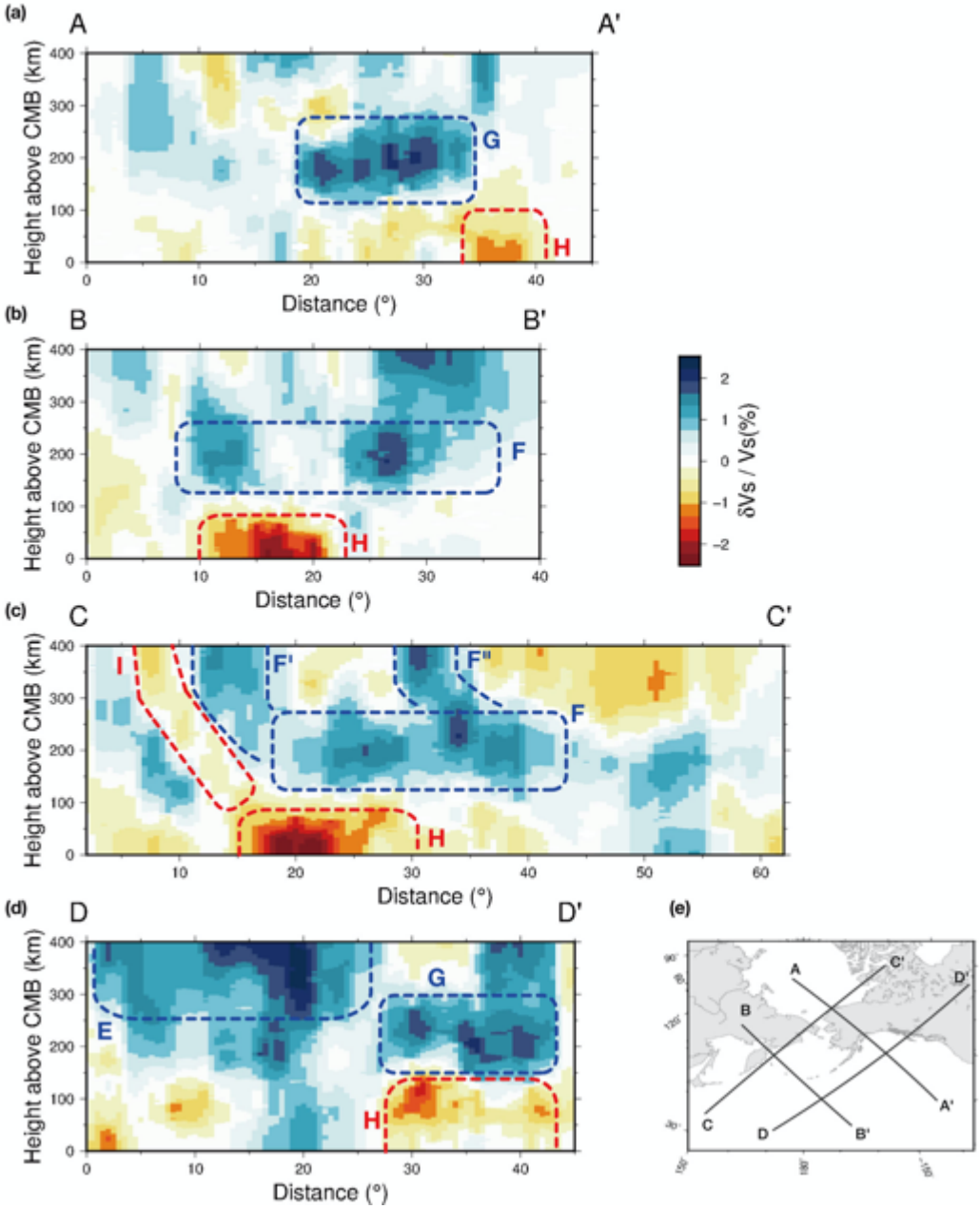

Figure 4.19 Cross-section of the inversion for the 3-D shear wave velocity structure (CG6) for cross-sections A-A′, B-B′, C-C′ and D-D′, which are shown in (e).

Strong low-velocity anomalies with a thickness of ~100 km exist immediately above the CMB below the cold slab remnants (Fig. 4.18). These strong low-velocity anomalies can be attributed to the TBL caused by the blanketing effect of the horizontally lying cold slab (Tan et al., 2002). Our model also shows a low-velocity anomaly continuous from the CMB to at least 400 km above the CMB (Fig. 4.18); this could be an upwelling plume that is deflected around the descending cold slab material. Previous numerical mantle convection studies are supportive of the hypothesis that the subducted slab causes plume-like upwelling (Tan et al., 2002; Tackley, 2011; Bower et al., 2013). On the other hand, this study suggests that the hot materials in the TBL developed beneath the cold slab remnants might produce upwelling (a passive plume) along the subducted slab. Our results are generally consistent with previous studies in terms of the location of the low-velocity anomaly. For example, the models of He et al. (2014) and French & Romanowicz (2014, 2015) show a low-velocity anomaly beneath Kamchatka continuous from the CMB to 850 km, and to about 500 km above the CMB, respectively.

4.6.2 Anisotropic (TI) structure

We conduct waveform inversion for the detailed 3-D anisotropic (TI) structure of the lowermost 400 km of the mantle beneath the northern Pacific using ~9,000 transverse and ~9,000 radial components records (Fig. 4.11). We interpret inferred 3-D D″ anisotropy structure based on recent knowledge from both theoretical and experimental mineral physics studies. Here, we assume that it is likely constituted by a rock assemblage in the lowermost mantle is dominated by a (Mg, Fe)SiO_3 bridgemanite

and by (Mg, Fe)O ferro-periclase (Fp). We consider the possible mineralogical mechanisms for anisotropy for each mineral (see Table 4.3), namely CPO of Mg-Pv, Fp, and post-perovskite phase of Mg-Pv. In this study, we used single-crystal elastic constant for Mg-Pv, Mg-pPv, and Fp from theoretical ab initio high *P*-*T* simulation studies (Wentzcovich et al. (2006) for Mg-Pv and -pPv and Karki (1999) for Fp).

	Mg-Pv[a]	Mg-pPv[a]	Fp[b]
Vertical flow	$\delta\xi<0$	$\delta\xi\approx0$	$\delta\xi<0$
Horizontal flow	$\delta\xi>0$	$\delta\xi<0$	$\delta\xi>0$

Table 4.3 Summary for anisotropy in each possible mineral in the lowermost mantle (Mg-Pv, Mg-pPv, and Fp) from mineral physics experiment and theoretical calculation to compute elastic moduli. We assumed that the horizontal and vertical flows produced their deviatoric stress inducing the associated CPO related to the vertical transverse isotropy (Yamazaki & Karato, 2006). Recent experimental studies determined the glide system of each minerals (Tsujino et al. (2016) for Pv, Yamazaki et al. (2006) for $CaIrO_3$ which is analogue material of Mg-pPv and Yamazaki & Karato (2002) for Fp). We used single-crystal elastic constant for Mg-Pv, Mg-pPv, and Fp from theoretical ab initio high-*P*-*T* simulation studies ([a] Wentzcovich et al. (2006) for Mg-Pv and -pPv and [b] Karki (1999) for Fp)

In order to relate the mantle flow geometry to the anisotropic geometry, the dominant glide systems for each material is needed. It is still controversial which mineral phase(s) contribute to the CPO. However, in order to interpret the inferred anisotropic structure we chose the following glide system examined by recent experimental and modeling results. For Mg-Pv, we consider a possible dominant glide

system, [001](100) suggested by recent experiment of Mg-Pv at 25 GPa (Tsujino et al., 2016). However, the glide system of pPv-$MgSiO_3$ has not yet been well determined. The dominant glide system of pPv-$CaIrO_3$ which is analogue material of Mg-pPv was determined as [100](010) from shear deformation experiments (Yamazaki et al., 2006), while that of Mg-pPv at 120 GPa was determined as [100](010) from numerical calculation (Goryaeve et al., 2016). In addition, we consider another possible dominant glide systems: [100](001) or [010](001), and [001](010) as suggested by high-pressure experiment at the lowermost mantle pressure condition (Miyagi et al., 2010; Merkel et al., 2007). Moreover, although the texture development during Pv to pPv transition in $MgSiO_3$ has not yet been clarified, also consider the c-axis [001] vertical alignment of Mg-pPv immediately after the phase transition from Pv-$MgSiO_3$ from analogy with the case for $MgGeO_3$ (Miyagi et al., 2011). As for Fp, dominant glide system is interpreted to be [110](100) (Yamazaki & Karato, 2002).

Let us consider the CPO of each mineral based on the above mineral physical knowledge in TI (i.e., radial anisotropy) case. Because the sign of the inferred ξ is more reliable them their amplitude, here, we assume two dominant mantle flow geometries such as vertical and horizontal flow, and classify anisotropic type using anisotropic parameter ξ, following Yamazaki & Karato (2002). For horizontal flow case, Mg-Pv and Fp, whose *a*-axis is vertically aligning, and will produce $\delta\xi > 0$, while Mg-pPv, whose *b*-axis is vertically aligning, and will produce $\delta\xi < 0$. For vertical flow case, Mg-Pv, whose *c*-axis is vertical, and will produce $\delta\xi < 0$; Fp, whose [110] is vertical, and will produce $\delta\xi < 0$; Mg-pPv, whose a-axis is vertical, and will produce $\delta\xi \approx 0$ (summarized in Table 4.3). Taking into account these relation between flow geometry and the sign of $\delta\xi$, we find three features to possibly explain the inferred anisotropic structure:

(1) $\delta\xi < 0$ region beneath Alaska at 300–400 km above the CMB, which corresponds to CPO of Pv and/or Fp induced by vertical flow. (2) $\delta\xi > 0$ region surrounding $\delta\xi < 0$ region, which corresponds to CPO of Pv and/or Fp induced by horizontal flow at 300–400 km above the CMB. (3) Dominant $\delta\xi > 0$ region at 100–300 km above the CMB, which also corresponds to CPO of Pv and/or Fp possibly as well as Mg-pPv induced by horizontal flow as discussed below.

First, we consider the case where the CPO of Mg-Pv and Mg-PPv produces anisotropic structure in D″. Based on above three points, the inferred observed anisotropy suggests following three possible situations: (a) Mg-pPv makes less contribution to anisotropy in the lowermost mantle. (b) Predominantly Mg-pPv contributes to anisotropy in the lowermost mantle. As we mentioned above, recent high *P-T* experiments suggested Mg-pPv can inherit texture from the Mg-Pv phase (Miyagi et al., 2011; Dobson et al., 2013), and dominant glide plane is (001) during Mg-Pv to Mg-pPv transition. (c) As there is no pure Mg-pPv phase but a mixture of Mg-Pv and Mg-pPv in the lowermost mantle due to broad coexisting field such as for the basaltic composition beneath the NP, and only Mg-Pv phase contributes to anisotropy. Although there is reported to be an uncertainty in the Mg-Pv to Mg-pPv transition thickness between Mg-Pv and Mg-pPv in the MORB composition, ranging from 5 GPa at 2500 K in Ohta et al. (2008) to 26 GPa in Sun et al. (2018) at 2200 K, the transition thickness in the MORB composition is much broader than that in the typical mantle composition such as pyrolite. Since MORB composition produces a wide two-phase coexistence region, and Mg-Pv phase in MORB subducted included with the oceanic plates could make contribution to anisotropy in this region.

Next, we consider the case where Mg-Pv and Mg-pPv do not make any

contribution to anisotropy in the lowermost mantle. In this case, Fp could produce most of the observed anisotropy, while the volume ratio between Mg silicate and Fp is more than double for the lower mantle (Jackson 1998). The high *P-T* deformation experiment and computation (Yamazaki et al., 2009; Madi et al., 2005) suggested that since Fp is plastically ~3 orders of magnitude softer than Mg silicate (Yamazaki & Karato, 2001), Fp could forms the 3-D network structure and will accommodate most of the strain in pyrolitic lower mantle. Remarkably, this means that our observed anisotropy in D″ can be explained by CPO only of Fp, not of Mg-Pv or Mg-pPv. This is also consistent with observed, gradual increase of positive anisotropy with depth.

In both above two cases (Mg-Pv and Mg-pPv carry the anisotropy in D″, and only Fp contribution to anisotropy) $\delta\xi < 0$ and $\delta\xi > 0$ can be interpreted as the vertical and horizontal flow, respectively. In Fig. 4.19(a, b), we compare cross-section of our obtained model in $\delta\xi$ and isotropic S-velocity model. Since the S-velocity anomalies can be primarily attributed to temperature anomaly, the high- and low-velocity anomalies indicate colder and hotter than average temperatures at each respective depth. Since the location of vertical flow region ($\delta\xi < 0$) at 200–400 km heights generally corresponding to high temperature region ($\delta Vs < 0$), the vertical flow should be upwelling. Together with the results of global tomographies that the low-Vs anomalies intermittently continue almost vertically to the surface (e.g., French & Romanowicz, 2015), this vertical flow could affect magmatism on the surface around Alaska (e.g., Bowie hotspot).

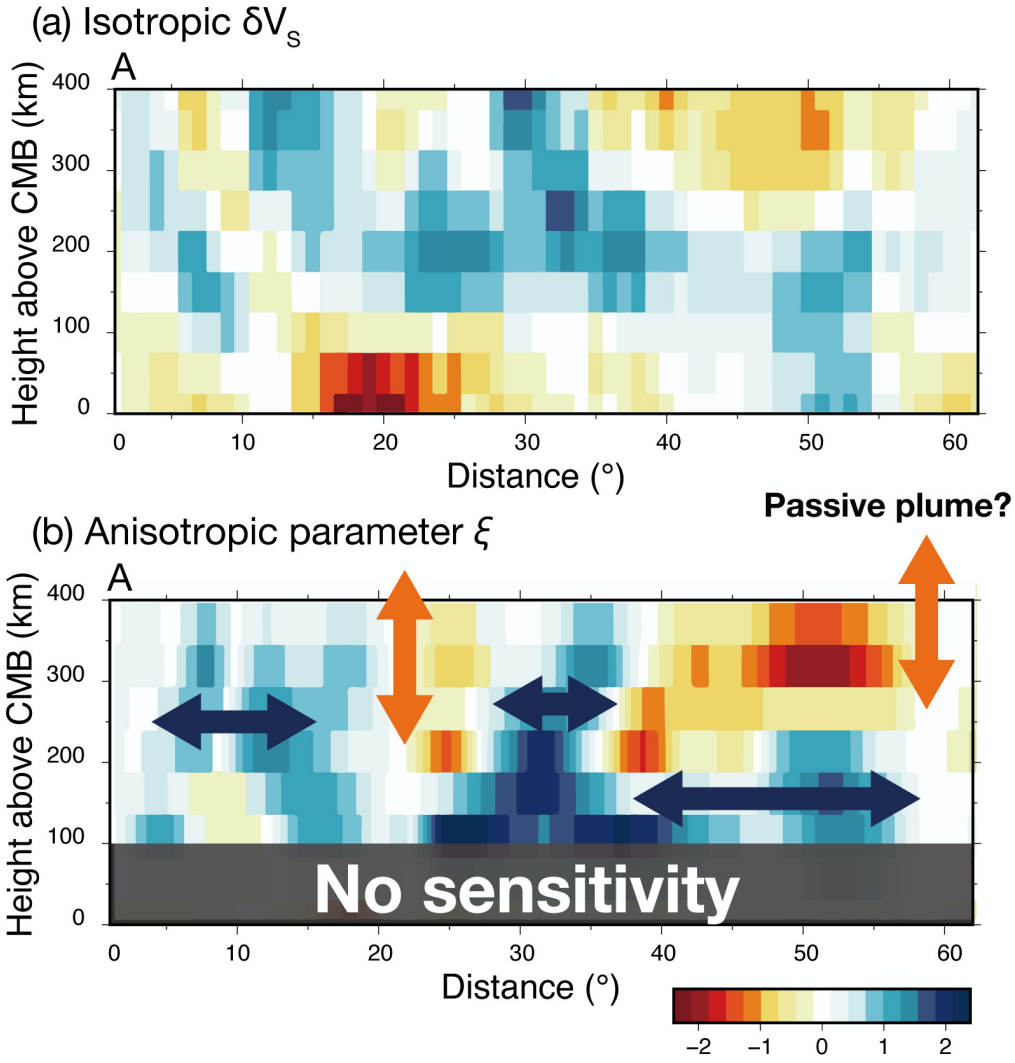

Figure 4.20 Cross-sections of the inversion for the 3-D (a) isotropic S-velocity and (b) anisotropic structure (CG6) for cross-sections A in inset of Fig. 4.11. Color contour shows $\delta\xi/\xi_{isotropic} = (\xi - \xi_{isotropic}) / \xi_{isotropic} = (\xi - 1) / \xi_{isotropic}$. Note that $\xi_{isotropic} = 1$.

On the other hand, the location of horizontal flow region ($\delta\xi > 0$) generally corresponds to low temperature region ($\delta Vs > 0$). Our model thus suggests the subduction of cold paleo-slabs with a low dip angle to D″. Of the ~2.5 percent of the high-velocity anomalies in our obtained 3-D S-velocity structure model, ~1.5 percent can be

explained by the MgPv to Mg-pPv phase transition. The remaining +1.0 percent anomaly can be explained by a 250 K decline in temperature, using the temperature derivative for Mg-pPv under lowermost mantle *P-T* conditions (Wentzcovitch et al., 2006). Geological evidence for subduction ~250 million years ago beneath the southern margin of Laurentia, together with an average subduction rate of ~1.2 cm/yr in the lower mantle, suggests that remnants of past subduction should be found at the CMB beneath the NP (Young et al., 2018). The following features of our models suggest the presence of paleoslabs: (i) ~3 percent high-Vs anomalies just above the CMB, (ii) vertically continuous low-Vs structures at the edge of the inferred high-Vs, (iii) the good agreement between the location of the past Izanagi plate boundary and the high-Vs anomaly.

Our obtained anisotropic structure shows growth of magnitude of positive anisotropy ($\delta\xi > 0$) with depth, and this suggests that degree of orientation of each mineral increase with depth. This is consistent with the results from geodynamical simulation which is showing that development of finite strain in the lowermost mantle in slab-subducting regions (McNamara et al., 2003). Our model also suggests that subducted cold slab impinge and lie not on the CMB but ~100 km above the CMB, possible dynamical boundary.

We summarize that: in the D″ region under the NP, observed anisotropy could be attributed to the deformation-induced CPO of Mg-Pv, Fp and Mg-pPv, whereas our obtained $\delta\xi$ models showing gradual increase of magnitude of anisotropy with depth prefer the CPO of Fp. Observed positive and negative anisotropy could be the evidence for paleo-Izanagi plate subduction with a low dip angle ~250 Ma and induced vertical upwelling flow by slab sinking. This suggests that the modality of convection in the lower mantle is controlled by plate tectonics on the surface ~250 Ma. Subduction beneath the

NP could temporarily cool the wide region of outer core, and upwelling plume induced by slab sinking may affect smaller scale convection modality and magmatism on the surface.

Chapter 5 Discussion and conclusions

5.1 Topics for further research

In this thesis we use the first order Born approximation with respect to a 1-D starting model to perform the inversion. It has been pointed out (Panning et al., 2009) that this approximation can lead to errors in the calculation of individual waveforms for a finite perturbation to the starting model. On the other hand, "non-linear" checkerboard tests show that when SPECFEM3D_GLOBE is used to calculate the synthetic waveforms and then the inversion is performed using the Born approximation satisfactory results are obtained (Borgeaud et al., 2017; 2019; this thesis Figs. 3.8 and 4.14). This suggests that the 3-D models obtained by the inversions in this thesis are likely to be reasonable, but that there may be some errors in the amplitude of the inferred velocity anomalies. The following are important topics for further research: 1) developing methods for making quantitative estimates of the errors due to using the first order Born approximation; 2) developing computationally feasible methods for performing iterative inversion with respect to a 3-D starting model.

The CMB topographic structure is another interesting topic for future studies, since CMB topographic structures provide additional constraints on the presence of temperature or chemical anomalies and are also related to the viscosity structure (Deschamps et al., 2018). In this dissertation, we utilize relatively longer period range (12.5—200 s) data and neglect the CMB topography structure. Since variations of the CMB topography affect high-frequency waveforms (Colombi et al., 2014), waveform inversion would provide further constraint of the CMB topography in future studies.

5.2 Geochemical reservoir

Our inferred structure within LLSVP suggests that western Pacific LLSVP consists of a cluster of small-scale low velocity anomalies with a diameter of ~300 km. We considered if the chemical anomaly can explain seismic low velocity anomalies. About 2 or 3 percent low-Vs anomalies could be due to chemical compositional impurities such as Fe and Al (Tsuchiya & Tsuchiya 2006; Zhang et al., 2006). Such chemical heterogeneity, resulting from core and mantle interaction, partial melting in the TBL, basaltic material entrained to the base of the mantle by past subduction, or as long-lived remnants of chemical differentiation in the early Earth, is expected immediately above the CMB (Garnero & McNamara, 2008; Garnero et al., 2016). Such chemical anomalies with an impurity content of 5–6 percent produce ~2 or ~3 percent low-Vs anomalies (Wentzcovitch et al., 2006; Tsuchiya & Tsuchiya, 2006).

An alternative interpretation for the low-velocity anomalies could be the presence of chemical anomalies with S-velocity lower than pyrolite. One possibility is that basaltic material might accumulate and form structures similar to LLSVP. However, if LLSVPs were formed purely from basaltic crust, unrealistically high temperatures would be required to explain the low-velocity anomalies (Deschamps et al., 2011). Another possible chemical anomaly is the crystallization of a past basal magma ocean from the mid-lower mantle and the remnant underlying lowermost mantle dense melts (Labrosse et al., 2007).

Since material with an impurity content of ~2 percent is at most ~1 percent denser than the surrounding mantle (Wentzcovitch et al., 2006; Tsuchiya & Tsuchiya, 2006), however, it is unlikely that it could survive in the lowermost mantle throughout geological time (~4 Gyr) and become the primordial geochemical reservoir,

as has been suggested by previous geodynamical studies (e.g., Nakagawa & Tackley, 2014). Therefore, it is unlikely that a cluster of low velocity anomalies at the western margin of the Pacific LLSVP inferred in this dissertation is due to the long-lived chemical heterogeneity such as the primordial mantle and geochemical reservoir.

Assuming that the whole Pacific LLSVP is almost chemically homogeneous, the Pacific LLSVP can be a cluster of the small-scale upwelling plume suggested by Davies et al. (2012). This implies that as the LLSVPs which are considered as the geochemical reservoir (Kellog et al., 1999) are chemically homogeneous, the geochemical reservoir could be the core rather than the lowermost mantle. This is consistent with previous geochemical studies suggested that the core be a possible source of primordial material based on $^{3}He/^{4}He$ ratio (Porcelli & Halliday, 2001). However, there might be localized and smaller-scale chemical anomalies such as a ULVZ (ultra-low velocity zone; Yu et al., 2018).

5.3 Chemical differentiation at the present lowermost mantle beneath the northern Pacific

The strong velocity contrast (~5 percent peak-to-peak over less than 100 km vertically and 300 km laterally) that we observe in the lowermost 100 km of the mantle seems too strong and sharp to be explained by only temperature variations; an about 5 percent velocity anomaly would require ~1500 K temperature variation. Chemical heterogeneities with enriched Fe content (i.e., basaltic composition) have a lower seismic velocity than pyrolite and can explain strong negative anomalies (Tsuchiya, 2011; Stixrude & Lithgow-Bertelloni, 2011). They are also denser than pyrolite and thus could remain at the CMB. Our model shows that strong low-velocity anomalies are concentrated in the lowermost 100 km of the mantle. Chemical anomalies at the CMB

provide the most reasonable explanation for the strong velocity gradient that we observe within 100 km of the CMB. Furthermore, geodynamical simulations of a slab sinking to the CMB show that in the case where a thin basaltic layer is present just above the CMB, the center of the slab reaches the CMB, but its edges are lying on a dense basaltic layer (Tackley, 2011). This is consistent with our results (Fig. 4.19) that suggest that the northwestern edge of the Izanagi paleoslab is lying on a strong low-velocity anomaly.

The global average sinking rate of slabs in the lower mantle based on seismic tomography is estimated to be from 1.1 cm/yr to 1.9 cm/yr (van der Meer et al., 2010; Domeier et al., 2016). Material subducted older than 160-260 Ma might thus have reached the CMB. Slabs at the CMB are strongly heated and probably disintegrate in ~100 million years (Tackley, 2011); thus material subducted before ~260-360 Ma is unlikely to cause high-velocity anomalies at the CMB. Geodynamical simulations of a slab sinking to the CMB show that in the case where slabs sunk with a low dip angle enhance segregation of the basalt in oceanic crustal material from depleted material, since the harzburgite is strongly heated and viscous (Tackley, 2011).

Our inferred high-Vs structure beneath the northern Pacific (Fig. 4.19a) which corresponds to the positive anisotropy ($\delta\xi > 0$; Fig. 4.19b) could be subducted Izanagi slab with a low dip angle. Since significant downwelling flow is expected in the lowermost mantle beneath the long-lived subduction zone such as northern Pacific, self-generated heat in subducted basaltic material is likely to be in the lowermost mantle (Tackley et al., 2012). Our obtained isotropic and anisotropic structure are consistent with the possibility that subducted material including large amount of radiogenic elements accumulated at the lowermost mantle produces concentrations of iron-rich material due to chemical differentiation which becomes the origin of upwelling flow from this iron-

rich material at the CMB due to the radiogenic heating.

5.4 Conclusion

In this dissertation, we conducted waveform inversion; (i) to infer the detailed Vs structure within the Pacific LLSVP using new dataset including recently deployed TSAR which provides a dataset with wide azimuthal coverage at the western Pacific LLSVP; (ii) to infer the detailed both isotropic and anisotropic *Vs* structure in D″ beneath the northern Pacific, beneath long-lived subduction zone, using a large number of waveforms taken from the recent full deployment of the USArray in the US (2004–2015) to improve the resolution of tomographic model in this region. We showed that:

1) recently deployed a seismic array in Thailand (TSAR) which provides a dataset with wide azimuthal coverage at the western edge of the Pacific LLSVP. We analyze the new dataset including this TSAR data using localized waveform inversion, which has better resolution, especially for low-velocity anomalies, than travel-time tomography. We found a high-velocity anomaly extending vertically to a height of at least 400 km above the CMB beneath the Philippine Sea and small-scale low-velocity anomalies immediately above the CMB beneath New Guinea. The location of the high-velocity anomaly is generally consistent with the Izanagi plate subduction boundary ~200 Ma, and the small-scale low-velocity patches with a diameter of ~300 km are consistent with the picture of a small-scale thermal plume clusters suggested by geodynamic studies which is relatively chemically homogeneous, rather than a part of a thermo-chemical pile. Hence, we conclude that the S-velocity structure at the western margin of the Pacific LLSVP and its sharp boundary can be explained by a cluster of thermal

plumes and significant lateral variation due to the existence of a cold paleoslab, respectively. This suggests that the LLSVP is relatively chemically homogeneous, and that the primordial geochemical reservoir could thus be the core rather than the base of the mantle.

2) high-resolution isotropic S-velocity model in D″ beneath the Northern Pacific. Our obtained S-velocity model showed three features. (i) There are prominent sheet-like lateral high-velocity anomalies up to ~3 percent faster than PREM with a thickness of ~200 km whose lower boundary is ~150 km above the CMB. There are also high-velocity anomalies extending in the east-west direction in the south of the Aleutian Islands at 300-400 km above the CMB and south of Alaska at 150-250 km above the CMB, respectively. There is an arc-like high-velocity anomaly from southwest of the Aleutian Islands through the east of the Kamchatka peninsula to Chukchi, the eastern tip of Siberia, at 150-200 km above the CMB. (ii) A prominent low-velocity anomaly, which is ~2.5 percent slower than PREM, is located to the west of the Kamchatka peninsula, immediately above the CMB beneath the high-velocity anomalies. (iii) There is a relatively thin (~300 km) low-velocity structure continuous from the low-velocity anomaly "ii" to at least 400 km above the CMB. We also detected a continuous low-velocity anomaly from the east of Kamchatka peninsula at 50 km above the CMB to the far east of the Kuril Islands at 400 km above the CMB. Assuming the velocity anomalies are due primarily to the effects of temperature, we interpret the above features as follows. (i) There are remnants of subducted slab materials which are stagnant ~150 km above the CMB. Furthermore, the Mg-Pv to Mg-pPv phase transition could enhance high-velocity anomalies in the slab due to the cold geotherm; (ii) hot and less dense material develops beneath the subducted cold

slab remnants; (iii) the hot and less dense material ascends along subducted cold slab remnants and forms a passive plume.

3) higher resolution anisotropic (TI) structure in D″ beneath the Northern Pacific. We performed waveform inversion to illuminate the high resolution (~450 km laterally, 100 km radially; this is 5^3 times finer than previous global anisotropic model proposed by Panning & Romanowicz (2006)) anisotropic structure related to mantle flow and/or deformation, using two horizontal components of waveforms mainly recorded by the USArray. The observed anisotropy would be interpreted as due to the deformation-induced alignment of ferropericlase and/or bridgmanite caused by mantle flow, horizontal and vertical flow related to the subducted paleo-Izanagi plate and the upwelling flow of hot material, respectively. Since the plume possibly induced by slab sinking, the modality of convection in the lowermost mantle could be controlled by Earth's surface tectonics since the initiation of subduction of paleo-Izanagi plate ~240 million years ago.
4) the slab sinks into the lowermost mantle beneath the northern Pacific with a low dip angle (i.e., almost horizontal flow). This implies that segregation of basalt from depleted material possibly occur in this ~100 Myr (Tackley, 2011), suggesting that the lowermost mantle beneath the northern Pacific subduction zone could be chemically distinct due to the accumulation of the basaltic materials enriched in the incompatible elements and radiogenic elements transported by significant downwelling from the Earth's surface via subduction of the oceanic plates.

References

Akaike, H. (1977). An extension of the method of maximum likelihood and the stein's problem. *Annals of the Insitute of Statistical Mathematics*, *29*, 153-164.

Aki, K., Christoffersson, A., & Husebye, E. S. (1977). Determination of the three-dimensional seismic structure of the lithosphere. *Journal of Geophysical Research*, *82*, 277-296.

Amaru, M. L. (2007). Global travel time tomography with 3-D reference models, *Geologica Ultraiectina*, *274*.

Borgeaud, A. F. E., Konishi, K., Kawai, K., & Geller, R. J. (2016). Finite frequency effects on apparent S-wave splitting in the D″ layer: comparison between ray theory and full-wave synthetics. *Geophysical Journal International*, *207*, 12-28.

Borgeaud, A. F. E., Konishi, K., Kawai, K., & Geller, R. J. (2017). Imaging paleoslabs in the D″ layer beneath Central America and the Caribbean using seismic waveform inversion. *Science Advances, 3*(11), e1602700. https://doi.org/10.1126/sciadv.1602700

Borgeaud, A. F. E., Kawai, K., & Geller, R. J. (2019). 3-D S-velocity structure of the mantle transition zone beneath Central America and the Gulf of Mexico using waveform inversion. *Journal of Geophysical Research: Solid Earth*, *124*. https://doi.org/10.1029/ 2018JB016924

Boschi, L. & Dziewonski, A. M. (2000). Whole Earth tomography from delay times of P, PcP, and PKP phases: lateral heterogeneities in the outer core or radial anisotropy in the mantle? *Journal of Geophysical Research: Solid Earth*, *105*, 13675–13696. https://doi.org/10.1029/2000JB900059

Bower, D. J., Gurnis, M. & Sun, D. (2013). Dynamic origins of seismic wave speed variation in D″. *Physics of the Earth and Planetary Interiors*, *214*, 74-86. https://doi.org/10.1016/j.pepi.2012.10.004

Bozdağ, E., Peter, D., Lefebvre, M., Komatitsch, D., Tromp, J., Hill, J., Podhorszki, N., & Pugmire, D. (2016). Global adjoint tomography: First-generation model. *Geophysical Journal International, 207*, 1739-1766. https://doi.org/10.1093/gji/ggw356

Brown, J. M., & Shankland, T. J. (1981). Thermodynamic parameters in the Earth as determined from seismic profiles. *Geophysical Journal of the Royal*

Astronomical Society, 66, 579-596. https://doi.org/10.1111/j.1365-246X.1981.tb04891.x

Bull, A. L., McNamara, A. K., & Ritsema, J. (2009). Synthetic tomography of plume clusters and thermochemical piles. *Earth and Planetary Science Letters, 278*, 152-162. https://doi.org/10.1016/j.epsl.2008.11.018

Bullen, K. E. (1949). Compressibility-pressure hypothesis and the Earth's interior. *Geophysical Journal International*, *5*, 335-368.

Bunge, H.-P., Richards, M. A., Lithgow-Bertelloni, C., Baumgardner, J. R., Grand, S. P., & Romanowicz, B. A. (1998). Time scales and heterogeneous structure in geodynamic Earth models. *Science, 280*, 91-95. https://doi.org/10.1126/science.280.5360.91

Chiao, L. Y., & Kuo, B. Y. (2001). Multiscale seismic tomography. *Geophysical Journal International*, *145*, 517-527. https://doi.org/10.1046/j.0956-540x.2001.01403.x

Chen, P., Zhao, L., & Jordan, T. H. (2007). Full 3D tomography for the crustal structure of the Los Angeles region. *Bulletin of the Seismological Society of America*, *97*, 1094-1120. https://doi.org/10.1785/0120060222

Colombi, A., Nissen-meyer, T., Boschi, L., & Giardini, D. (2014). Seismic waveform inversion for core–mantle boundary topography. *Geophysical Journal International*, *198*, 55-71. https://doi.org/10.1093/gji/ggu112

Cottaar, S., & Romanowicz, B. (2013). Observations of changing anisotropy across the southern margin of the African LLSVP. *Geophysical Journal International, 195*, 1184-1195. https://doi.org/10.1093/gji/ggt285

Cottaar, S., Heister, T., Rose, I., & Unterborn, C. (2014). BurnMan: A lower mantle mineral physics toolkit. *Geochemistry, Geophysics, Geosystems*, *15*, 1164-1179. https://doi.org/10.4088/JCP .11m07343

Cummins, P. R., Geller, R. J., Hatori, T. & Takeuchi, N. (1994a). DSM complete synthetic seismograms: SH, spherically symmetric, case. *Geophysical Research Letters*, *21*, 533-536. https://doi.org/10.1029/GL021i007p00533

Cummins, P. R., Geller, R. J. & Takeuchi, N. (1994b). DSM complete synthetic seismograms: P-SV, spherically symmetric, case. *Geophysical Research Letters*, *21*, 1663-1666. https://doi.org/10.1029/94GL01281

Cummins, P. R., Takeuchi, N. & Geller, R. J. (1997). Computation of complete synthetic seismograms for laterally heterogeneous models using the Direct Solution Method. *Geophysical Journal International*, *130*, 1-16. https://doi.org/10.1111/j.1365-246X.1997.tb00983.x

Dahlen, F. A. & Tromp, J. (1998). *Theoretical Global Seismology*, Princeton Univ. Press.

Davies, D. R., Goes, S., Schuberth, B. S. A., Bunge, H. P., & Ritsema, J. (2012). Reconciling dynamic and seismic models of Earth's lower mantle: the dominant role of thermal heterogeneity. *Earth and Planetary Science Letters, 353-354*, 253-269. https://doi.org/10.1016/j.epsl.2012.08.016

Deschamps, F., Kaminski, E. & Tackley, P. (2011). A deep mantle origin for the primitive signature of ocean island basalt. *Nature Geoscience*, *4*, 879-882. https://doi.org/10.1038/ngeo1295

Dobson, D. P., Miyajima, N., Nestola, F., Alvaro, M., Casati, N., Liebske, C., Wood, I. G., & Walker, A. M. (2013). Strong inheritance of texture between perovskite and post-perovskite in the D″ layer. *Nature Geoscience*, *6*, 575-578. http://dx.doi.org/10.1038/NGEO1844.

Domeier, M., Doubrovine, P. V., Torsvik, T. H., Spakman, W., & Bull, A. L. (2016). Global correlation of lower mantle structure and past subduction. *Geophysical Research Letters*, *43*, 4945-4953. https://doi.org/10.1002/2016GL068827

Dziewonski, A. M. (1984). Mapping the lower mantle, Determination of lateral heterogeneity in P velocity up to degree and order 6. *Journal of Geophysical Research*, *89*, 5929-5952. https://doi.org/10.1029/JB089iB07p05929

Dziewonski, A. M., & Anderson, D. L. (1981). Preliminary reference Earth model. *Physics of the Earth and Planetary Interiors*, *25*, 297-356. https://doi.org/10.1016/0031-9201(81)90046-7

Dziewonski, A. M., Hager, B. H., & O'Connell, R. J. (1977). Large-scale heterogeneities in the lower mantle. *Journal of Geophysical Research*, *82*, 239-255.

Fichtner, A., Kennett, B. L. N., Igel, H., & Bunge, H.-P. (2008). Theoretical background for continental and global scale full-waveform inversion in the time-frequency domain. *Geophysical Journal International*, *175*, 665-685.

Fichtner, A., Kennett, B. L. N., Igel, H., & Bunge, H.-P. (2009). Full waveform tomography for upper-mantle structure in the Australasian region using adjoint methods. *Geophysical Journal International*, *179*, 1703-1725.

Fichtner, A., Kennett, B. L. N., Igel, H., & Bunge, H.-P. (2010). Full waveform tomography for radially anisotropic structure: new insights into present and past states of the Australasian upper mantle. *Earth and Planetary Science Letters*, *290*, 270-280.

French, S. W., & Romanowicz, B. A. (2014). Whole-mantle radially anisotropic S-velocity structure from spectral-element waveform tomography. *Geophysical Journal International*, *199*, 1303-1327. https://doi.org/10.1093/gji/ggu334

French, S. W., & Romanowicz, B. A. (2015). Broad plumes rooted at the base of the Earth's mantle beneath major hotspots, *Nature*, *525*, 95-99. https://doi.org/10.1038/nature14876

Fuji N., Kawai K., & Geller R. J. (2010). A methodology for inversion of broadband seismic waveforms for elastic and anelastic structure and its application to the mantle transition zone beneath the northwestern pacific. *Physics of the Earth and Planetary Interiors*, *180*, 118-137. https://doi.org/10.1016/j.pepi.2009.10.004

Fukao, Y., Obayashi, M., Inoue, H., & Nenbai, M. (1992). Subducting slabs stagnant in the mantle transition zone. *Journal of Geophysical Research*, *97*, 4809–4822. https://doi.org/10.1029/91JB02749

Fukao, Y., Widiyantoro S. & Obayashi M. (2001). Stagnant slabs in the upper and lower mantle transition region. *Reviews of Geophysics*, *39*, 291-323. https://doi.org/10.1029/1999RG000068

Garnero, E. J. (2000). Heterogeneity of the lowermost mantle. *Annual Review of the Earth and Planetary Sciences*, *28*, 509-537. https://doi.org/10.1146/annurev.earth.28.1.509

Garnero, E. J., Lay, T., & McNamara, A. (2007). Implications of lower mantle structural heterogeneity for existence and nature of whole mantle plumes, In: *The Origin of Melting Anomalies: Plates, Plumes and Planetary Processes*, Foulger, G. R. & Jurdy, D. M. (eds.), The Geological Society of America Special Paper, 430, p79-101, doi:10.1130/2007.2430(05)

Garnero, E. J., Maupin, V., Lay, T., & Fouch, M. J. (2004). Variable azimuthal anisotropy in Earth's lowermost mantle, *Science*, *306*, 259-261. https://doi.org/10.1126/science.1103411

Garnero, E. J., & McNamara, A. K. (2008). Structure and dynamics of Earth's lower mantle. *Science*, *320*, 626-628. https://doi.org/10.1126/science.1148028

Garnero, E. J., McNamara, A. K., & Shim, S.-H. (2016). Continent-sized anomalous zones with low seismic velocity at the base of Earth's mantle. *Nature Geosci*ence, *9*, 481-489. https://doi.org/10.1038/ngeo2733

Geller, R. J., & Hara, T., (1993). Two efficient algorithms for iterative linearized inversion of seismic waveform data. *Geophysical Journal International*, *115*, 699-710. https://doi.org/10.1111/j.1365-246X.1993.tb01488.x

Geller, R. J., & Ohminato, T. (1994). Computation of synthetic seismograms and their partial derivatives for heterogeneous media with arbitrary natural boundary conditions using the direct solution method. *Geophysical Journal International*, *116*, 421-446. https://doi.org/10.1111/j.1365-246X.1994.tb01807.x

Geller, R. J., & Takeuchi, N. (1995). A new method for computing highly accurate DSM synthetic seismograms. *Geophysical Journal International*, *123*, 449-470.

Geller, R. J., & Takeuchi, N. (1998). Optimally accurate second order time domain finite difference scheme for the elastic equation of motion. *Geophysical Journal International*, *135*, 48-62.

Geller, R. J., Mizutani, H., Hirabayashi, N., & Takeuchi, N. (2013a). Method for synthesizing numerical operators, system for synthesizing operators, and simulation device, U.S. Patent 8423332.

Geller, R. J., Mizutani, H., Hirabayashi, N., & Takeuchi, N. (2013b). Method for synthesizing numerical operators, system for synthesizing operators, and simulation device: Japan Patent 5,279,016.

Goes, S., Agrusta, R., van Hunen, J., & Garel, F. (2017). Subduction-transition zone interaction: A review. *Geosphere*, *13*, 644-664. https://doi.org/10.1130/GES01476.1

Gorbatov A., Widiyantoro S., Fukao Y., & Gordeev E. (2000). Signature of remnant slabs in the North Pacific from P-wave tomography. *Geophysical Journal International*, *142*, 27-36. https://doi.org/10.1046/j.1365-246x.2000.00122.x

Grand, S. P. (1997). Tomographic for shear velocity beneath the North American plate, *Journal of Geophysical Research*, *92*, 14065-14090. https://doi.org/10.1029/JB092iB13p14065

Grand, S. P. (2002). Mantle shear-wave tomography and the fate of subducted slabs. *Philosophical Transactions of the Royal Society of London. Series A: Mathematical, Physical and Engineering Sciences*, *360*(1800), 2475-2491. https://doi.org/10.1098/rsta.2002.1077

Gréaux, S., Irifune, T., Higo, Y., Tange, Y., Arimoto, T., Liu, Z., & Yamada, A. (2019). Sound velocity of CaSiO3 perovskite suggests the presence of basaltic crust in the Earth's lower mantle. *Nature*, *565*, 218-221. https://doi.org/10.1038/s41586-018-0816-5

Gu, Y. J., Dziewonski, A. M., Su, W. J., & Ekstrom, G. (2001). Models of the mantle shear velocity and discontinuities in the pattern of lateral heterogeneities. *Journal of Geophysical Research*, *106*, 11169-11199. https://doi.org/10.1029/2001JB000340

Gu, Y. J., Dziewonski, A. M., & Ekstrom, G. (2003). Simultaneous inversion for mantle shear velocity and topography of transition zone discontinuities. *Geophysical Journal International*, *104*, 559-583. https://doi.org/10.1046/j.1365-246X.2003.01967.x

Gung, Y., Panning, M., & Romanowicz, B. (2003). Global anisotropy and the thickness of continents. *Nature*, *422*, 707-711. https://doi.org/10.1038/nature01559

Hara, T. (2004). Waveform inversion for 3-D Earth structure using the direct solution method implemented on vector-parallel supercomputer, *Physics of the Earth and Planetary Interiors*, 146, 65-74. https://doi.org/10.1016/j.pepi.2003.06.010

Hara, T. & Geller, R. J. (2000). Simultaneous waveform inversion for three-dimensional Earth structure and Earthquake source parameters considering a wide range of modal coupling. *Geophysical Journal International*, *142*, 539-550. https://doi.org/10.1046/j.1365-246x.2000.00168.x

Hara, T., Tsuboi, S., & Geller, R. J. (1991). Inversion for laterally heterogeneous Earth structure using a laterally heterogeneous starting model: Preliminary results. *Geophysical Journal International*, *104*, 523-540. https://doi.org/10.1111/j.1365-246X.1991.tb05699.x

Hara, T., Tsuboi, S., & Geller, R. J. (1993). Inversion for laterally heterogeneous upper mantle S-wave velocity structure using iterative waveform inversion. *Geophysical Journal International*, *115*, 667-698. https://doi.org/10.1111/j.1365-246X.1993.tb01487.x

Hasegawa, K., Konishi, K., & Fuji, N. (2018). Improvement of accuracy of the spectral element method for elastic wave computation using modified numerical integration operators. *Computer Methods in Applied Mechanics and Engineering*, *342*, 200-223. https://doi.org/10.1016/j.cma.2018.07.025

He, X., & Long, M. D. (2011). Lowermost mantle anisotropy beneath the northwest-ern Pacific: evidence from PcS, ScS, SKS, and SKKS phases. *Geochemistry Geophysics Geosystem*, *12*, Q12012. http://dx.doi.org/10.1029/2011GC003779.

He Y., Wen L., & Zheng T. (2014). Seismic evidence for an 850 km thick low-velocity structure in the Earth's lowermost mantle beneath Kamchatka. *Geophysical Research Letters*, *41*, 7073-7079.

He, Y., Wen, L., & Zheng, T. (2006). Geographic boundary and shear wave velocity structure of the “Pacific anomaly” near the core-mantle boundary beneath western Pacific. *Earth and Planetary Science Letters, 244*, 302-314. https://doi.org/10.1016/j.epsl.2006.02.007

Helmberger, D. V., & Burdick, L. J. (1979). Synthetic seismograms. *Annual Reviews of the Earth and Planetary Sciences*, *7*, 417-442. https://doi.org/10.1146/annurev.ea.07.050179.002221

Houser, C., Masters, G., Shearer, P., & Laske, G. (2008). Shear and compressional velocity models of the mantle from cluster analysis of long-period waveforms. *Geophysical Journal International*, *174*, 195-212. https://doi.org/10.1111/j.1365-246X.2008.03763.x

Idehara, K., Tanaka, S., & Takeuchi, N. (2013). High-velocity anomaly adjacent to the western edge of the Pacific low-velocity province. *Geophysical Journal International*, *192*, 1-6. https://doi.org/10.1093/gji/ggs002

Inoue, H., Fukao, Y., Tanabe. K., & Ogata, Y. (1990). Whole mantle P-wave traveltime tomography. *Physics of the Earth and Planetary Interiors*, *59*, 294-328. https://doi.org/10.1016/0031-9201(90)90236-Q

Jackson, I. (1998). Elasticity, composition and temperature of the Earth's lower mantle: a reappraisal. *Geophysical Journal International*, *134*, 291-311. https://doi.org/10.1046/j.1365-246x.1998.00560.x

Kaneshima, S., & Helffrich, G. (2013). Vp structure of the outermost core derived from analyzing large scale array data of SmKS waves. *Geophysical Journal International*, *193*, 1537-1555. https://doi.org/10.1093/gji/ggt042

Kamiya S., Miyatake T. & Hirahara K. (1988). How deep can we see the high-velocity anomalies beneath the Japan Islands? *Geophysical Research Letters*, *15*, 828-831. https://doi.org/10.1029/GL015i008p00828

Karason, H., & van der Hilst R. D. (2001). Improving global tomography models of P-wave speed I: incorporation of differential traveltimes for refracted and diffracted core phases (PKP, Pdiff). *Journal of Geophysical Research*, *106*, 6569-6587.

Karato, S. (1998). Some remarks on the origin of seismic anisotropy in the D″ layer. *Earth Planets Space*, *50*, 1019-1028. https://doi.org/10.1186/BF03352196

Karki, B. B., Wentzcovitch, R. M., de Gironcoli, S., & Baroni, S. (1999). First principles determination of elastic anisotropy and wave velocities of MgO at lower mantle conditions. *Science*, *286*, 1705-1707. https://doi.org/10.1126/science.286.5445.1705

Kawai, K., & Geller, R. J. (2010a). Inversion of seismic waveforms for shear wave velocity structure in the lowermost mantle beneath the Hawaiian hotspot. *Physics of the Earth and Planetary Interiors*, *183*, 136-142. https://doi.org/10.1016/j.pepi.2010.08.001

Kawai, K., & Geller, R. J. (2010b). Waveform inversion for localized seismic structure and an application to D″ structure beneath the Pacific. *Journal of Geophysical Research*, *115*, B01305, https://doi:10.1029/2009JB006503

Kawai, K. & Geller, R. J. (2010c). The vertical flow in the lowermost mantle beneath the Pacific from inversion of seismic waveforms for anisotropic structure. *Earth and Planetary Science Letters*, *297*, 190-198. https://doi.org/10.1016/j.epsl.2010.05.037

Kawai, K., Takeuchi, N., & Geller R. J. (2006). Complete synthetic seismograms up to 2 Hz for transversely isotropic spherically symmetric media. *Geophysical*

Journal International, *164*, 411-424. https://doi.org/10.1111/j.1365-246X.2005.02829.x

Kawai, K., Takeuchi, N., Geller, R. J., & Fuji, N. (2007a). Possible evidence for a double crossing phase transition in D″ beneath Central America from inversion of seismic waveforms. *Geophysical Research Letters*, *34*, L09314, https://doi:10.1029/2007GL029642

Kawai, K., Geller, R. J., & Fuji, N. (2007b). D″ beneath the Arctic from inversion of shear waveforms. *Geophysical Research Letters*, *34*, L21305, https://doi:10.1029/2007GL031517

Kawai, K., & Tsuchiya, T. (2009). Temperature profile in the lowermost mantle from seismological and mineral physics joint modeling. *Proceedings of the National Academy of Sciences*, *106*, 22119-22123. https://doi.org/10.1073/pnas.0905920106

Kawai, K., Sekine, S., Fuji, N., & Geller, R. J. (2009). Waveform inversion for D″ structure beneath northern Asia using Hi-net tiltmeter data. *Geophysical Research Letters*, *36*, L20314, https://doi:10.1029/2009GL039651

Kawai, K., Konishi, K., Geller, R. J., & Fuji, N. (2014). Methods for inversion of body-wave waveforms for localized three-dimensional seismic structure and an application to D″ structure beneath central America. *Geophysical Journal International*, *197*, 495-524. https://doi.org/10.1093/gji/ggt520

Kllogg, L.H., Hager, B.H. & van der Hilst, R. (1999). Compositional stratification in the deep mantle. *Science*, *283*, 1881–1884, https://doi.org/10.1126/science.283.5409.1881

Koelemeijer, P., Ritsema, J., Deuss, A., & van Heijst, H. J. (2016). SP12RTS: a degree-12 model of shear- and compressional-wave velocity for Earth's mantle. *Geophysical Journal International, 204*, 1024-1036. https://doi.org/10.1093/gji/ggv481

Komatitsch, D., Barnes, C., & Tromp, J. (2000). Wave propagation near a fluid-solid interface: a spectral element approach. *Geophysics*, *65*, 623-631. https://doi.org/10.1190/1.1444758

Komatitsch, D., & Vilotte, J.-P. (1998). The spectral element method: an efficient tool to simulate the seismic response of 2D and 3D geological structures. *Bulletin of the Seismological Society of America*, *88*, 368-392.

Komatitsch, D., & Tromp, J. (2002a). Spectral-element simulations of global seismic wave propagation -I. Validation. *Geophysical Journal International*, *149*, 390-412. https://doi.org/10.1046/j.1365-246X.2002.01653.x

Komatitsch, D., & Tromp, J. (2002b). Spectral-element simulation of global seismic wave propagation-II. Three-dimensional models, oceans, rotation and self-gravitation. *Geophysical Journal International*, *150*, 303-318. https://doi.org/10.1046/j.1365-246X.2002.01716.x

Komatitsch, D., Vilotte, J. P., Tromp, J., Afanasiev, M., Bozdag, E., Charles, J., Chen, M., Goddeke, D., Hjorleifsdottir, V., Labarta, J., Le Goff, N., Le Loher, P., Liu, Q., Maggi, A., Martin, R., McRitchie, D., Messmer, P., Michea, D., Nissen-Meyer, T., Peter, D., Rietmann, M., de Andrade, S., Savage, B., Schuberth, B., Siemenski, A., Strand, L., Tape, C., Xie, Z., & Zhu, H. (2015). SPECFEM3D GLOBE v7.0.0 (Computational Infrastructure for Geodynamics); https://geodynamics.org/cig/software/specfem3d_globe/

Komatitsch, D., Vinnik, L. P., & Chevrot, S. (2010). SHdiff-SVdiff splitting in an isotropic Earth. *Journal of Geophysical Research, 115*, B07312. http://dx.doi.org/10.1029/2009JB006795

Konishi, K., Kawai, K., Geller, R. J., & Fuji, N. (2014). Waveform inversion for localized three-dimensional seismic velocity structure in the lowermost mantle beneath the western Pacific, *Geophysical Journal International*, *199*, 1245-1267. https://doi.org/10.1093/gji/ggu288

Kustowski, B., Ekström, G., & Dziewonski, A. M. (2008). Anisotropic shear-wave velocity structure of the Earth's mantle: A global model. *Journal of Geophysical Research*, *113*, B06306, https://doi:10.1029/2007JB005169

Labrosse, S., Hernlund, J. W., & Coltice, N. (2007). A crystallizing dense magma ocean at the base of the Earth's mantle. *Nature*, *450*, 866-869. https://doi.org/10.1038/nature06355

Lay, T., & Garnero, E. J. (2011). Deep mantle seismic modeling and imaging. *Annual Review of the Earth and Planetary Science*, *39*, 91-123. https://doi.org/10.1146/annurev-earth-040610-133354

Lay, T., & Helmberger, D. V. (1983). The shear-wave velocity gradient at the base of the mantle. *Journal of Geophysical Research*, *88*, 8160-8170. https://doi.org/10.1029/JB088iB10p08160

Lebedev, S., & van der Hilst, R. D. (2008). Global upper-mantle tomography with the automated multimode inversion of surface and S-wave forms. *Geophysical Journal International*, *173*, 505-518. https://doi.org/10.1111/j.1365-246X.2008.03721.x

Lekic, V., & Romanowicz, B. (2011). Inferring upper-mantle structure by full waveform tomography with the spectral element method. *Geophysical Journal International*, *185*, 799-831. https://doi.org/10.1111/j.1365-246X.2011.04969.x

Li, M., McNamara, A. K., & Garnero, E. J. (2014). Chemical complexity of hotspots caused by cycling oceanic crust through mantle reservoirs. *Nature Geoscience*, *7*, 336-370. https://doi.org/10.1038/ngeo2120

Li, X. D., & Romanowicz, B. (1995). Comparison of global waveform inversions with and without considering cross-branch modal coupling. *Geophysical Journal International*, *121*, 695-709. https://doi.org/10.1111/j.1365-246X.1995.tb06432.x

Li, X. D., & Romanowicz, B. (1996). Global mantle shear velocity model developed using nonlinear asymptotic coupling theory. *Journal of Geophysical Research*, *22*, 245-272. https://doi.org/10.1029/96JB01306

Li, X. D., & Tanimoto, T. (1993). Waveforms of long-period body waves in a slightly aspherical Earth model. *Geophysical Journal International*, *112*, 92-102. https://doi.org/10.1111/j.1365-246X.1993.tb01439.x

Lithgow-Bertelloni, C., & Richards, M. A. (1998). The dynamics of Cenozoic and Mesozoic plate motions. *Review of Geophysics*, *36*, 27-78. https://doi.org/10.1029/97RG02282

Masters, G., Laske, G., Bolton, H., & Dziewonski, A. (2000). The relative behavior of shear velocity, bulk sound speed, and compressional velocity in the mantle: implications for chemical and thermal structure. In *Earth's Deep Interior: Mineral Physics and Tomography From the Atomic to the Global Scale*, pp. 63-87, eds. Karato, S., Forte, A. M., Libermann, R. C., Masters, G., & Stixrude, L., America Geophysical Union. https://doi.org/10.1029/GM117p0063

Matthews, K. J., Maloney, K. T., Zahirovic, S., Williams, S.E., Seton, M., & Müller, R. D. (2016). Global plate boundary evolution and kinematics since the late Paleozoic. *Global and Planetary Change*, *146*, 226-250. https://doi.org/10.1016/j.gloplacha.2016.10.002

Maupin, V. (1994). On the possibility of anisotropy in the D″ layer as inferred from the polarization of diffracted S waves. *Physics of the Earth and Planetary Interiors*, *87*, 1–32. https://doi.org/10.1016/0031-9201(94)90019-1

Maupin, V., Garnero, E. J., Lay, T., & Fouch, M. J. (2005). Azimuthal anisotropy in the D″ layer beneath the Caribbean. *Journal of Geophysical Research: Solid Earth*, *110*, 1-20. https://doi.org/10.1029/2004JB003506

Maupin, V., & Park, J. (2008). Seismic anisotropy: theory and observations. In *Treatise in Geophysics*, eds. Romanowicz, B., Dziewonski, A. M., Vol. 1, pp. 289-321. Amsterdam: Elsevier.

McNamara, A. K., van Keken, P. E., & Karato, S.-I. (2003). Development of finite strain in the convecting lower mantle and its implications for seismic anisotropy. *Journal of Geophysical Research: Solid Earth*, 108, 1-14. https://doi.org/10.1029/2002jb001970

McNamara, A., & Zhong, S. (2005). Thermochemical structures beneath Africa and the Pacific Ocean. *Nature, 437*, 1136-1139. https://doi.org/10.1038/nature04066

Mégnin, C., & Romanowicz, B. (2000). The shear velocity structure of the mantle from the inversion of body, surface, and higher modes waveforms. *Geophysical Journal International, 143*, 709-728. https://doi.org/10.1046/j.1365-246X.2000.00298.x

Mitchell, B. J., & Helmberger, D. V. (1973). Shear velocities at the base of the mantle from observations of S and ScS. *Journal of Geophysical Research*, 78, 6009-6020. https://doi.org/10.1029/JB078i026p06009

Miyagi, L., & Wenk, H. R. (2016). Texture development and slip systems in bridgmanite and bridgmanite + ferropericlase aggregates. *Physics and Chemistry of Minerals*, *43*, 597–613. https://doi.org/10.1007/s00269-016-0820-y

Montagner, J.-P. (1999). Where can seismic anisotropy be detected in the Earth's mantle? In boundary layers. *Pure and Applied Geophysics*, *151*, 223-256. https://doi.org/10.1007/s000240050113

Montagner J.-P. (2002). Seismic Anisotropy Tomography. In: Fink M., Kuperman W. A., Montagner J. P., Tourin A. (eds) *Imaging of Complex Media with Acoustic and Seismic Waves. Topics in Applied Physics*, *84*, Springer. https://doi.org/10.1007/3-540-44680-X_8

Montagner, J.-P. & Kennett B. L. N. (1996). How to reconcile body-wave and normal-mode reference earth models, *Geophysical Journal International*. *125*, 229-248, https://doi.org/10.1111/j.1365-246X.1996.tb06548.x

Montagner, J.-P., & Tanimoto, T. (1990). Global anisotropy in the upper mantle inferred from the regionalization of phase velocities. *Journal of Geophysical Research*, *95*, 4797- 4819, http://doi:10.1029/JB095iB04p04797.

Montagner, J.-P., & Tanimoto, T. (1991). Global upper mantle tomography of seismic velocities and anisotropies. *Journal of Geophysical Research*, *96*, 20337- 20351, https://doi:10.1029/91JB01890.

Müller, R. D., Seton, M., Zahirovic, S., Williams, S.E., Matthews, K. J., Wright, N.M., Shephard, G. E., Maloney, K. T., Barnett-Moore, N., Hosseinpour, M., Bower, D. J., & Cannon, J. (2016). Ocean basin evolution and global-scale plate reorganization events since Pangea breakup. *Annual Review of Earth and Planetary Sciences*, *44*, 107-138. https://doi.org/10.1146/annurev-earth-060115-012211

Murakami, M., Hirose, K., Kawamura, K., Sata, N., & Ohishi, O. (2004). Post-perovskite phase transition in $MgSiO_3$. *Science, 304*(5672), 855-858. https://doi.org/10.1126/science.1095932

Nakada, M., Iriguchi, C., & Karato, S. (2012). The viscosity structure of the D" layer of the Earth's mantle inferred from the analysis of Chandler wobble and tidal deformation. *Physics of the Earth and Planetary Interiors*, *208*, 11-24. https://doi.org/10.1016/j.pepi.2012.07.002

Nakagawa, T., & Tackley, P. J. (2005). Deep mantle heat flow and thermal evolution of the Earth's core in thermochemical multiphase models of mantle convection. *Geochemistry, Geophysics, Geosystems*, *6*, 1–12. https://doi.org/10.1029/2005GC000967

Nakagawa, T., & Tackley, P. J. (2014). Influence of combined primordial layering and recycled MORB on the coupled thermal evolution of Earth's mantle and core. *Geochemistry, Geophysics, Geosystems*, *15*, 619-633. https://doi.org/10.1002/2013GC005128

Nataf, H. C., Nakanishi, I., & Anderson, D. L. (1984). Anisotropy and shear velocities in the upper mantle. *Geophysical Research Letters*, *11*, 109-112. http://dx.doi.org/10.1029/ GL011i002p00109.

Nataf, H. C., Nakanishi, I., & Anderson D. L. (1986). Measurements of mantle wave velocities and inversion for lateral heterogeneities and anisotropy. Part III: inversion, *Journal of Geophysical Research*, *91*, 7261-7307.

Ni, S., Tan, E., Gurnis, M., & Helmberger, D. V. (2002). Sharp sides to the African superplume. *Science*, *296*, 1850-1852. https://doi.org/10.1126/science.1070698

Nolet, G., & Dahlen, F. A. (2000). Wavefront healing and the evolution of seismic delay times. *Journal of Geophysical Research*, *105*, 19043-19054. https://doi.org/10.1029/2000JB900161

Nowacki, A., Wookey, J., & Kendall, J.-M. (2010). Deformation of the lowermost mantle from seismic anisotropy. *Nature*, *467*, 1091-1094. http://dx.doi.org/10.1038/nature09507

Nowacki, A., & Wookey, J. (2016). The limits of ray theory when measuring shear wave splitting in the lowermost mantle with ScS waves. *Geophysical Journal International*, *207*, 1573-1583. https://doi.org/10.1093/gji/ggw358

Obayashi, M., & Fukao, Y. (1997). P and PcP traveltime tomography for the core-mantle boundary. *Journal of Geophysical Research*, *102*, 17825-17841. https://doi.org/10.1029/97JB00397

Panning, M. & Romanowicz, B. (2004). Influences on flow at the base of the Earth's mantle based on seismic anisotropy. *Science*, *303*, 351-353. https://doi.org/10.1126/science.1091524

Panning, M. P., Capdeville, Y., & Romanowicz, B. A. (2009). Seismic waveform modelling in a 3-D Earth using the Born approximation: potential shortcomings and a remedy. *Geophysical Journal International*, *177*, 161-178. https://doi:10.1111/j.1365-246X.2008.04050.x

Parisi, L., Ferreira, A. M. G., & Ritsema, J. (2018). Apparent Splitting of S Waves Propagating Through an Isotropic Lowermost Mantle. *Journal of Geophysical Research: Solid Earth*, *123*, 3909-3922. https://doi.org/10.1002/2017JB014394

Porcelli, D., & Halliday, A. N. (2001). The core as a possible source of mantle helium. *Earth and Planetary Science Letters*, *192*, 45-56. https://doi.org/10.1016/S0012-821X(01)00418-6

Pratt, R. G. (1999) Seismic waveform inversion in the frequency domain, Part 1: theory and verification in a physical scale model. *Geophysics*, *64*, 888-901. https://doi.org/10.1190/1.1444597

Pysklywec R. N., & Ishii M. (2005). Time dependent subduction dynamics driven by the instability of stagnant slabs in the transition zone. *Physics of the Earth and Planetary Interiors*, *149*, 115-132. https://doi.org/10.1016/j.pepi.2004.08.019

Raitt, R. W. (1963) Marine physics laboratory. Scripps Institution of Oceanography, University of California San Diego. MPL-U-23/63.

Rawlinson, N., & Spakman, W. (2016). On the use of sensitivity tests in seismic tomography. *Geophysical Journal International*, 205, 1221-1243. https://doi.org/10.1093/gji/ggw084

Ringwood, A. E. (1989). Significance of the terrestrial Mg/Si ratio. *Earth and Planetary Science Letters*, *95*, 1–7. https://doi.org/10.1016/0012-821X(89)90162-3

Ritsema, J., van Heijst, H. J., & Woodhouse, J. H. (1999). Complex shear velocity structure imaged beneath Africa and Iceland, *Science*, *286*, 1925-1928. https://doi.org/10.1126/science.286.5446.1925

Ritsema J, McNamara A. K., & Bull A. (2007). Tomographic filtering of geodynamic models: implications for model interpretation and large-scale mantle structure. *Journal of Geophysical Research*, *112*, https://10.1029/2006JB004566

Ritsema, J., van Heijst, H. J., Deuss, A., & Woodhouse, J. H. (2011). S40RTS: a degree-40 shear velocity model for the mantle from new Rayleigh wave dispersion, teleseismic traveltimes, and normal-mode splitting function measurements. *Geophysical Journal International*, *184*, 1223-1236. https://doi.org/10.1111/j.1365-246X.2010.04884.x

Robertson, G. S., & Woodhouse, J. H. (1996). Ratio of relative S to P velocity heterogeneity in the lower mantle, *Journal of Geophysical Research*, *101*, 20041-20052. https://doi.org/10.1029/96JB01905

Romanowicz, B. (2003). Global mantle tomography, Progress status in the past 10 years. *Annual Reviews of the Earth and Planetary Science*, *31*, 303-328. https://doi.org/10.1146/annurev.earth.31.091602.113555

Rost, S., & Garnero, E. J. (2004). Array seismology advances research into Earth's interior. *Eos Transactions AGU*, *85*, 301-306. https://doi:10.1029/2004EO320002.

Schubert, G., Masters, G., Olsen, P., & Tackley, P. (2004). Superplumes or plume clusters? *Physics of the Earth and Planetary Interiors*, *146*, 147-162. https://doi.org/10.1016/j.pepi.2003.09.025

Schuberth, B. S. A., Bunge, H.-P., & Ritsema, J. (2009). Tomographic filtering of high-resolution mantle circulation models: can seismic heterogeneity be explained by temperature alone? *Geochemistry, Geophysics, Geosystems*, *10*, Q05W03, https://doi.org/10.1029/2009GC002401

Sengupta, M. K. & Toksöz, M. N. (1976). Three dimensional model of seismic velocity variation in the Earth's mantle. *Geophysical Research Letters*, *3*, 84-86. https://doi.org/10.1029/GL003i002p00084

Shephard, G. E., Matthews, K. J., Hosseini, K., & Domeier, M. (2017). On the consistency of seismically imaged lower mantle slabs. *Scientific Reports*, *7*, 10976. https://doi.org/10.1038/s41598-017-11039-w

Silver, P. G., & Chan, W. W. (1991). Shear Wave Splitting and Sub continental Mantle Deformation. *Journal of Geophysical Research*, *96*, 16429-16454. https://doi.org/10.1029/91JB00899

Simmons, N. A., Forte, A., Boschi, L., & Grand, S. P. (2010). GyPSuM: a joint tomographic model of mantle density and seismic wave speeds. *Journal of Geophysical Research*, *115*, B12310. https://doi.org/10.1029/2010JB007631

Stixrude, L., & Lithgow-Bertelloni, C. (2011). Thermodynamics of mantle minerals – II. Phase equilibria. *Geophysical Journal International*, *184*, 1180-1213. https://doi:10.1111/j.1365-246X.2010.04890.x

Stevenson D. J. (1981). Models of the Earth's core. *Science, 214*, 611-619. https://doi.org/10.1126/science.214.4521.611

Su, W. J., & Dziewonski, A. M. (1997). Simultaneous inversion for 3-D variations in shear and bulk velocity in the mantle. *Physics of the Earth and Planetary Interiors*, *100*, 135-156. https://doi.org/10.1016/S0031-9201(96)03236-0

Su, W. J., Woodward, R. L., & Dziewonski, A. M. (1994). Degree-1-2 of shear velocity het- erogeneity in the mantle. *Journal of Geophysical Research*, *99*, 6945-6980. https://doi.org/10.1029/93JB03408

Sun, D., Helmberger, D., Ni, S., & Bower, D. (2009). Direct measures of lateral velocity variation in the deep Earth. *Journal of Geophysical Research*, *114*, B05303. https://doi.org/10.1029/2008JB005873

Suzuki, Y., Kawai, K., Geller, R. J., Borgeaud, A. F. E., & Konishi, K. (2016). Waveform inversion for 3-D S-velocity structure of D″ beneath the Northern

Pacific: possible evidence for a remnant slab and a passive plume. *Earth Planets and Space, 68*, 198. https://doi.org/10.1186/s40623-016-0576-0

Tackley, P. J. (2011). Living dead slabs in 3-D: The dynamics of compositionally-stratified slabs entering a “slab graveyard" above the core-mantle boundary. *Physics of the Earth and Planetary Interiors*, *188*, 150-162. https://doi.org/10.1016/j.pepi.2011.04.013

Takeuchi, N. (2007). Whole mantle SH-velocity model constrained by waveform inversion based on three-dimensional Born kernels, *Geophysical Journal International*, *169*, 1153-1163. https://doi.org/10.1111/j.1365-246X.2007.03405.x

Takeuchi, N. (2012). Detection of ridge-like structures in the Pacific large low-shear-velocity province. *Earth and Planetary Science Letters, 319-320*, 55-64. https://doi.org/10.1016/j.epsl.2011.12.024

Takeuchi, N., & Kobayashi, M. (2004). Improvement of seismological earth models by using data weighting in waveform inversion. *Geophysical Journal International*, *158*, 681–694. https://doi.org/10.1111/j.1365-246X.2004.02334.x

Takeuchi, N., Morita, Y., Xuyen, N. D., & Zung N. Q. (2008). Extent of the low-velocity region in the lowermost mantle beneath the western Pacific detected by the Vietnamese Broadband Seismograph Array. *Geophysical Research Letters*, *35*, L05307. https://doi.org/10.1029/2008GL033197

Tan, E., Gurnis, M., & Han, L. (2002). Slabs in the lower mantle and their modulation of plume formation. *Geochemistry Geophysics Geosystems*, *3*, 1067, https://doi:10.1029/2001GC000238

Tanaka, S., Kawakatsu, H., Obayashi, M., Chen, Y. J., Ning, J., Grand, S. P., Niu, F., & Ni, J. (2015). Rapid lateral variation of P-wave velocity at the base of the mantle near the edge of the Large-Low Shear Velocity Province beneath the western Pacific. *Geophysical Journal International, 200*, 1050-1063. https://doi.org/10.1093/gji/ggu455

Tanaka, S., Siripunvaraporn, W., Boonchaisuk, S., Noisagool, S., Kim, T., Kawai, K., Suzuki, Y., Ishihara, Y., Iritani, R., Miyakawa, K., Takeuchi, N., & Kawakatsu, H. (2019). Thai Seismic Array (TSAR) Project. *Bulletin of the Earthquake Research Institute, in press.*

Tanimoto, T. (1986). The Backus-Gilbert approach to the 3-D structure in the upper mantle - II. SH and SV velocity. *Geophysical Journal of the Royal Astronomical Society*, *84*, 49-69. https://doi.org/10.1111/j.1365-246X.1986.tb04344.x

Tanimoto, T. (1990). Long-wavelength S-wave velocity structure throughout the mantle. *Geophysical Journal International*, *100*, 327-336. https://doi.org/10.1111/j.1365-246X.1990.tb00688.x

Tanimoto, T., & Anderson, D. L. (1985). Mapping convection in the mantle. *Geophysical Research Letters*, *11*, 287-290. https://doi.org/10.1029/GL011i004p00287

Tape, C., Liu, Q., Maggi, A., & Tromp, J. (2009). Adjoint tomography of the southern California crust. *Science*, *325*, 988-992. https://doi.org/10.1126/science.1175298

Tape, C., Liu, Q., Maggi, A., & Tromp, J. (2010). Seismic tomography of the southern California crust based on spectral-element and adjoint methods. *Geophysical Journal International*, *180*, 433-462. https://doi.org/10.1111/j.1365-246X.2009.04429.x

Tarantola, A. (1986). A strategy for nonlinear elastic inversion of seismic reflection data. *Geophysics*, *51*, 1893-1903. https://doi.org/10.1190/1.1442046

Thomson, A. R., Crichton, W. A., & Brodholt, J. P., Wood, I. G., Siersch, N. C., Muir, J. M. R., Dobson D. P., & Hunt, S. A. (2009). Seismic velocities of $CaSiO_3$ perovskite can explain LLSVPs in Earth's lower mantle. *Nature*, *572*, 643-647 https://doi.org/10.1038/s41586-019-1483-x

To, A., Romanowicz, B., Capdeville, Y., & Takeuchi, N. (2005). 3D effects of sharp boundaries at the borders of the African and Pacific Superplumes: Observation and modeling. *Earth and Planetary Science Letters*, *233*, 137-153. http://dx.doi.org/10.1016/j. epsl.2005.01.037

Tsuboi, S., & Geller, R. J. (1987). Partial derivatives of synthetic seismograms for a laterally heterogeneous Earth model. *Geophysical Research Letters*, *14*, 832-835. https://doi.org/10.1029/GL014i008p00832

Tsuchiya, T. (2011). Elasticity of subducted basaltic crust at the lower mantle pressures: Insights on the nature of deep mantle heterogeneity. P*hysics of the Earth and Planetary Interiors*, *188*, 142-149. https://doi.org/10.1016/j.pepi.2011.06.018

Tsuchiya, T., & Tsuchiya, J. (2006). Effect of impurity on the elasticity of perovskite and postperovskite: velocity contrast across the postperovskite transition in (Mg,

Fe, Al) (Si, Al)O_3. *Geophysical Research Letters*, *33*, L12S04. https://doi.org/10.1029/2006GL025706

Tsuchiya, T., Tsuchiya, J., Umemoto, K., & Wentzcovitch, R. M. (2004). Phase transition in $MgSiO_3$ perovskite in the Earth's lower mantle. *Earth and Planetary Science Letters*, *224*, 241-248. https://doi.org/10.1016/j.epsl.2004.05.017

Tsujino, N., Nishihara, Y., Yamazaki, D., Seto, Y., Higo, Y., & Takahashi, E. (2016). Mantle dynamics inferred from the crystallographic preferred orientation of bridgmanite. *Nature*, *539*, 81-84. https://doi.org/10.1038/nature19777

van der Hilst R. D., & Spakman, W. (1989). Importance of the reference model in linearized tomography and images of the subduction below the Caribbean plate. *Geophysical Research Letters*, 16, 1093-1096.

van Der Hilst, R. D., Widiyantoro, S., & Engdahl, E. R. (1997). Evidence for deep mantle circulation from global tomography. *Nature*, 386(6625), 578–584. https://doi.org/10.1038/386578a0

van der Meer, D. G., Spakman, W., van Hinsbergen, D. J. J., Amaru, M. L., & Torsvik, T. H. (2010). Towards absolute plate motions constrained by lower-mantle slab remnants. *Nature Geoscience*, 3, 36–40. https://doi.org/10.1038/ngeo708

van der Meer, D. G., van Hinsbergen, D. J. J, & Spakman, W. (2018). Atlas of the underworld: Slab remnants in the mantle, their sinking history, and a new outlook on lower mantle viscosity. *Tectonophysics*, *723*, 309-448. https://doi.org/10.1016/j.tecto.2017.10.004

Vinnik, L., Breger, L., & Romanowicz, B. (1998). Anisotropic structures at the base of the Earth's mantle. *Nature*, *39*, 564–567. https://doi.org/10.1038/31208

Wentzcovitch, R. M., Tsuchiya, T., & Tsuchiya, J. (2006). $MgSiO_3$ postperovskite at D″ conditions. *Proceedings of the National Academy of Sciences*, *103*, 543-546. https://doi.org/10.1073/pnas.0506879103

Woodhouse, J. H., & Dziewonski, A. M. (1984). Mapping the upper mantle: Three-dimensional modeling of the Earth structure by inversion of seismic waveforms. *Journal of Geophysical Research*, *89*, 5953-5986. https://doi.org/10.1029/JB089iB07p05953

Wookey, J., & Kendall, J. M. (2007). Seismic Anisotropy of Post-Perovskite and the Lowermost Mantle. In Post-Perovskite: The Last Mantle Phase Transition (eds

K. Hirose, J. Brodholt, T. Lay and D. Yuen). *Geophysical Monograph Series*, *174*, 171-189. https://doi.org/10.1029/174GM13

Wookey, J., & Kendall, J. M. (2008). Constraints on lowermost mantle mineralogy and fabric beneath Siberia from seismic anisotropy. *Earth and Planetary Science Letters*, *275*, 32–42. https://doi.org/10.1016/j.epsl.2008.07.049

Wysession, M. E., Lay, T., Revenaugh, J., Williams, Q., Garnero E. J., Jeanloz, R., & Kellogg L. H. (1998). The D″ discontinuity and its implications. in *The Core-Mantle Boundary Region*, pp 273-297, eds. Gurnis, M., Wysession, M., Knittle, E., Buffett, B. A., American Geophysical Union.

Yamaya, L., Borgeaud, A. F. E., Kawai, K., Geller, R. J., & Konishi, K. (2018). Effects of redetermination of source time functions on the 3-D velocity structure inferred by waveform inversion. *Physics of the Earth and Planetary Interiors*, *282*, 117–143. https://doi.org/10.1016/j.pepi.2018.04.012

Yamazaki, D., & Karato, S. I. (2002). Fabric development in (Mg,Fe)O during large strain, shear deformation: Implications for seismic anisotropy in Earth's lower mantle. *Physics of the Earth and Planetary Interiors*, *131*, 251–267. https://doi.org/10.1016/S0031-9201(02)00037-7

Yamazaki, D., Yoshino, T., Ohfuji, H., Ando, J., & Yoneda, A. (2006). Texture of $(Mg,Fe)SiO_3$ perovskite and ferro-periclase aggregate: Implications for rheology of the lower mantle. *Earth and Planetary Science Letters*, *252*, 372-378.

Yamazaki, D., Yoshino, T., Matsuzaki, T., Katsura, T., & Yoneda, A. (2009). Origin of seismic anisotropy in the D″ layer inferred from shear deformation experiments on postperovskite phase. *Physics of the Earth and Planetary Interiors*, *174*, 138-144. https://doi.org/10.1016/j.epsl.2006.10.004

Young, C. J., & Lay, T. (1990). Multiple phase analysis of the S-velocity structure in the D″ region beneath Alaska. *Journal of Geophysical Research*, *95*, 17385-17402. https://doi.org/10.1029/JB095iB11p17385

Young, A., Flament, N., Maloney, K., Williams, S., Matthews, K., Zahirovic, S., & Müller, R. D. (2019). Global kinematics of tectonic plates and subduction zones since the late Paleozoic Era. *Geoscience Frontiers*, *10*, 989-1013. https://doi.org/10.1016/j.gsf.2018.05.011

Yu, S., & Garnero, E. J. (2018). Ultralow velocity zone locations: A global assessment. *Geochemistry, Geophysics, Geosystems*, *19*, 396-414. https://doi.org/10.1002/2017GC007281

Yu, Y., Hung, T.D., Yang, T., Xue, M., Liu, K.H., & Gao, S. (2017). Lateral variations of crustal structure beneath the Indochina Peninsula. *Tectonophysics*, *712-713*, 193-199. https://doi.org/10.1016/j.tecto.2017.05.023

Zhang, N., Zhong, S. J., Leng, W., & Li, Z. X. (2010). A model for the evolution of Earth's mantle structure since the early Paleozoic. *Journal of Geophysical Research*, *115*, B06401. https://doi.org/10.1029/2009JB006896

Zhang, S., Cottaar, S., Liu, T., Stackhouse, S., & Militzer, B. (2006). High-pressure, temperature elasticity of Fe- and Al-bearing $MgSiO_3$: Implications for the Earth's lower mantle. *Earth and Planetary Science Letters*, *434*, 264-273. https://doi.org/10.1016/j.epsl.2015.11.030

Appendix A Sensitivity to SKS phase on elastic moduli in D″

Phase and group velocities

We begin by stating the constitutive relation for a TI medium.

$$\begin{pmatrix} c_{11} & c_{12} & c_{13} & & & \\ c_{12} & c_{22} & c_{23} & & O & \\ c_{13} & c_{23} & c_{33} & & & \\ & & & c_{44} & & \\ & O & & & c_{44} & \\ & & & & & c_{66} \end{pmatrix} = \begin{pmatrix} A & H & F & & & \\ H & A & F & & O & \\ F & F & C & & & \\ & & & L & & \\ & O & & & L & \\ & & & & & N \end{pmatrix}, \tag{A.1}$$

where

$$H = A - 2N. \tag{A.2}$$

Thus, there are five independent elastic constants, A, C, F, L, and N in a TI medium. For an isotropic medium the relations between the above five constants and λ and μ are as follows:

$$\lambda + 2\mu = A = C \tag{A.3}$$

$$\mu = L = N \tag{A.4}$$

$$\lambda = F = H. \tag{A.5}$$

We first derive below the theory for a flat-layered transversely isotropic (TI) medium for SH- and P-SV-waves, then extend them to spherical case.

SH waves in a flat-layered TI medium

We consider SH waves for which the displacement is

$$u_y = D \exp(i(\omega t - k_x x - k_z z)) \tag{A.6}$$

with $u_x = u_z = 0$.

The non-zero strains e_{ij} are given by

$$e_{xy} = \frac{1}{2}u_{y,x} = \frac{1}{2}(-ik_x u_y) \tag{A.7}$$

$$e_{yz} = \frac{1}{2}u_{y,z} = \frac{1}{2}(-ik_z u_y). \tag{A.8}$$

The explicit values of the non-zero components of the stress tensor for the 2-D SH case are as follows:

$$\sigma_{xy} = -Nik_x u_y \tag{A.9}$$

$$\sigma_{yz} = -Lik_z u_y. \tag{A.10}$$

The strain energy is

$$PE = \frac{1}{2}e_{ij}^{*}\sigma_{ij} \tag{A.11}$$

$$= \frac{1}{2}\left(2e_{xy}^{*}\sigma_{xy} + 2e_{yz}^{*}\sigma_{yz}\right) \tag{A.12}$$

$$= \frac{1}{2}\mathbf{W}^{*}\mathbf{H}\mathbf{W}, \tag{A.13}$$

where

$$\mathbf{H} = (Nk_x^2 + Lk_z^2) \tag{A.14}$$

$$\mathbf{W} = (D), \tag{A.15}$$

and $\mathbf{W}^{*}$ is the conjugate transpose of $\mathbf{W}$.

The kinetic energy is

$$KE = \frac{1}{2}\omega^2 u_i^{*}\rho u_i \tag{A.16}$$

$$= \frac{1}{2}\omega^2(u_x^{*}\rho u_x + u_z^{*}\rho u_z) \tag{A.17}$$

$$= \frac{1}{2}\omega^2\mathbf{W}^{*}\mathbf{T}\mathbf{W}, \tag{A.18}$$

where

$$\mathbf{T} = \rho \tag{A.19}$$

The equations of motion are obtained by setting to zero the gradient of the Lagrangian $L(\mathbf{W})$

$$\mathbf{L} = \frac{1}{2}\omega^2 \mathbf{W}^* \mathbf{T} \mathbf{W} - \frac{1}{2}\mathbf{W}^* \mathbf{H} \mathbf{W} \tag{A.20}$$

and when $\delta L = 0$

$$(\omega^2 \mathbf{T}\mathbf{W} - \mathbf{H}\mathbf{W}) = 0. \tag{A.21}$$

The phase velocities of the SH-wave are obtained by solving the equation of motions (A.21):

$$\omega = \sqrt{\frac{Nk_x^2 + Lk_z^2}{\rho}}. \tag{A.22}$$

The group velocity $\mathbf{U} = (U_x, U_z)$ is given by

$$U_x = \frac{\partial \omega}{\partial k_x} = \frac{k_x N/\rho}{\sqrt{(Nk_x^2 + Lk_z^2)/\rho}} \tag{A.23}$$

$$U_z = \frac{\partial \omega}{\partial k_z} = \frac{k_z L/\rho}{\sqrt{(Nk_x^2 + Lk_z^2)/\rho}}. \tag{A.24}$$

P-SV waves in a flat-layered TI medium

We consider P-SV waves for which the displacement is

$$\begin{aligned} u_x &= A_x \exp\left(i\left(\omega t - k_x x - k_y y\right)\right) \\ u_y &= 0 \\ u_z &= A_z \exp\left(i\left(\omega t - k_x x - k_y y\right)\right). \end{aligned} \tag{A.25}$$

The non-zero strains e_{ij} are given by

$$e_{xx} = u_{x,x} = -ik_x u_x \tag{A.26}$$

$$e_{zz} = u_{z,z} = -ik_z u_z \tag{A.27}$$

$$e_{xz} = \frac{1}{2}\left(u_{x,z} + u_{z,x}\right) = -\frac{i}{2}(k_x u_z + k_z u_x). \tag{A.28}$$

The explicit values of the non-zero components of the stress tensor for the 2-D P-SV case are as follows:

$$\sigma_{xx} = -i(Ak_x u_x + Fk_z u_z) \tag{A.29}$$

$$\sigma_{yy} = -i(Hk_x u_x + Fk_z u_z) \tag{A.30}$$

$$\sigma_{zz} = -i(Fu_x k_x + Cu_z k_z) \tag{A.31}$$

$$\sigma_{xz} = iL(k_x u_z + k_z u_x). \tag{A.32}$$

The strain energy is

$$PE = \frac{1}{2} e_{ij}^* \sigma_{ij} \tag{A.33}$$

$$= \frac{1}{2}(e_{xx}^* \sigma_{xx} + e_{zz}^* \sigma_{zz} + e_{xz}^* \sigma_{xz}) \tag{A.34}$$

$$= \frac{1}{2}\mathbf{W}^* \mathbf{H} \mathbf{W}, \tag{A.35}$$

where $\mathbf{W} = (A_x \; A_z)^T$, and $\mathbf{W}^*$ is the conjugate transpose of $\mathbf{W}$ and

$$H = \begin{pmatrix} Ak_x^2 + Lk_z^2 & k_x k_z (F + L) \\ k_x k_z (F + L) & kk_x^2 + Ck_z^2 \end{pmatrix}. \tag{A.36}$$

The kinetic energy is

$$KE = \frac{1}{2}\omega^2 u_i^* \rho u_i \tag{A.37}$$

$$= \frac{1}{2}\omega^2 (u_x^* \rho u_x + u_z^* \rho u_z) \tag{A.38}$$

$$= \frac{1}{2}\omega^2 \mathbf{W}^* \mathbf{T} \mathbf{W}, \tag{A.39}$$

where

$$\mathbf{T} = \begin{pmatrix} \rho & \\ & \rho \end{pmatrix}. \tag{A.40}$$

The two eigenvalues $\omega_{\pm}$ for pseudo-P and pseudo-S waves are given, respectively, by

$$\omega_+^2 = \frac{1}{2\rho}\Big[k_1^2(A+L) + k_3^2(C+L) + \Big\{\big(k_1^2(A-L) - k_3^2(C-L)\big)^2 + 4k_1^2k_3^2(F+L)^2\Big\}^{\frac{1}{2}}\Big] \tag{A.41}$$

$$\omega_-^2 = \frac{1}{2\rho}\Big[k_1^2(A+L) + k_3^2(C+L) - \Big\{\big(k_1^2(A-L) - k_3^2(C-L)\big)^2 + 4k_1^2k_3^2(F+L)^2\Big\}^{\frac{1}{2}}\Big]. \tag{A.42}$$

The corresponding group velocities are $U_\pm = (U_x^\pm\ U_z^\pm)^T$ are given by

$$U_x^\pm = \frac{\partial\omega_\pm}{\partial k_x} = \frac{1}{4\rho\omega}\left(2k_x(A+L) - \frac{2k_x(A-L)\{k_x^2(A-L) - k_z^2(C-L)\} + 4k_xk_z^2(F+L)^2}{[\{k_x^2(A-L) - k_z^2(C-L)\}^2 + 4k_x^2k_z^2(F+L)^2]^{\frac{1}{2}}}\right) \tag{A.43}$$

$$U_z^\pm = \frac{\partial\omega_\pm}{\partial k_z} = \frac{1}{4\rho\omega}\left(2k_z(C+L) - \frac{2k_z(L-C)\{k_x^2(A-L) - k_z^2(C-L)\} + 4k_{xz}^2(F+L)^2}{[\{k_x^2(A-L) - k_z^2(C-L)\}^2 + 4k_x^2k_z^2(F+L)^2]^{\frac{1}{2}}}\right). \tag{A.44}$$

Appendix B List of Events

I show the list of events used to infer the structure of the D″ region beneath the western Pacific in chapter 3, and of the D″ region beneath the northern Pacific in chapter 4.

Table B1 Events list used in chapter 3

Event#	Date (YYYY MM DD)	Latitude (°)	Longitude (°)	Depth (km)	Mw	Half duration (sec.)
1	1996 04 20	-22.44	-179.71	594.4	5.7	1.5
2	1996 05 06	-24.85	178.97	575.4	5.5	1.4
3	1996 05 14	-17.77	-178.51	629.0	5.7	1.7
4	1998 01 26	-22.32	-176.36	160.8	5.6	1.7
5	1998 01 27	-20.73	-179.16	651.4	5.9	2.3
6	1998 01 27	-22.39	179.29	629.4	6.4	4.1
7	1998 01 27	-22.53	179.29	616.9	6.3	3.5
8	1998 03 29	-17.57	-178.85	553.7	7.1	9.3
9	1998 04 14	-23.73	-179.81	509.6	6.1	2.7
10	1998 04 28	-21.88	-179.49	618.4	5.7	1.7
11	1998 05 16	-21.80	-176.17	178.0	5.5	1.3
12	1998 05 16	-22.27	-179.35	608.8	6.8	6.5
13	1998 07 09	-30.51	-178.71	154.5	6.9	6.8
14	1998 09 01	-17.55	-174.52	219.2	5.6	1.6
15	1998 09 02	-29.59	-178.38	206.3	5.5	1.4
16	1998 09 27	-20.38	-175.54	231.9	5.6	1.6
17	1998 10 11	-20.91	-178.99	638.1	5.9	1.0
18	1998 10 24	-17.74	-174.96	271.0	5.5	1.4
19	1998 11 15	-21.55	-175.87	171.0	6.2	3.3
20	1998 11 24	-16.42	-174.46	235.8	6.0	2.5
21	1998 12 22	-25.01	179.87	513.0	5.5	1.4
22	1998 12 27	-21.69	-175.86	159.6	6.8	6.4

23	1999 01 25	-17.83	-178.27	650.1	5.7	1.9
24	1999 01 27	-22.29	-178.82	449.4	5.5	1.4
25	1999 03 06	-21.60	-179.04	634.1	5.6	1.7
26	1999 03 23	-20.79	-178.65	584.1	5.6	1.7
27	1999 04 09	-26.37	178.28	635.6	6.1	3.3
28	1999 04 13	-21.54	-175.89	172.8	6.8	6.3
29	1999 05 18	-38.47	175.29	275.9	5.7	1.7
30	1999 06 26	-17.76	-178.17	623.9	6.0	2.6
31	1999 07 09	-20.36	-177.97	585.6	5.6	1.5
32	1999 07 18	-22.45	179.70	586.5	5.9	2.3
33	1999 07 21	-18.20	-177.85	583.5	5.6	1.6
34	1999 08 18	-36.91	177.60	153.0	5.7	1.8
35	1999 10 08	-21.77	-176.35	184.0	5.5	1.5
36	1999 10 25	-38.49	175.78	157.6	6.0	2.4
37	1999 11 30	-21.12	-178.52	556.8	5.8	2.0
38	1999 12 10	-22.05	179.85	611.3	5.6	1.6
39	1999 12 11	-17.64	-178.62	579.2	5.7	1.8
40	2000 01 02	-17.74	-178.56	610.6	5.5	1.3
41	2000 01 08	-16.84	-173.81	162.4	7.2	9.7
42	2000 01 13	-17.38	-178.63	564.6	6.2	3.3
43	2000 01 15	-21.11	-179.10	650.7	6.0	2.5
44	2000 02 12	-15.77	-174.60	237.6	5.9	2.3
45	2000 02 28	-17.46	-178.81	562.6	5.9	2.3
46	2000 03 01	-19.04	-179.08	686.4	5.8	1.9
47	2000 03 01	-19.19	-179.20	687.7	5.6	1.6
48	2000 03 18	-24.14	179.02	539.5	5.5	1.4
49	2000 04 01	-17.62	-178.67	575.8	5.6	1.6
50	2000 04 01	-18.13	-178.34	606.6	5.5	1.2
51	2000 04 07	-18.86	-175.77	223.7	5.7	1.9
52	2000 04 11	-27.93	-178.03	188.3	5.8	2.0
53	2000 04 17	-22.00	-179.22	559.8	5.5	1.6
54	2000 04 18	-20.73	-176.07	220.0	5.9	2.3

55	2000 05 02	-15.41	-177.24	423.5	5.5	1.4
56	2000 05 04	-17.72	-178.31	539.8	6.4	4.2
57	2000 05 08	-31.07	-179.98	394.3	5.6	1.6
58	2000 05 20	-23.28	179.77	553.6	5.6	1.4
59	2000 06 14	-25.45	178.38	615.4	6.4	4.1
60	2000 06 16	-28.74	-178.09	230.3	5.5	1.4
61	2000 07 01	-34.89	178.82	201.4	5.6	1.6
62	2000 07 13	-18.23	-175.27	266.7	5.5	1.4
63	2000 08 02	-18.21	-174.46	202.8	5.5	1.4
64	2000 08 15	-31.42	-179.95	367.4	6.6	4.7
65	2000 09 02	-17.82	-178.30	620.9	5.7	1.8
66	2000 09 02	-19.90	-178.92	698.4	5.9	2.3
67	2000 09 03	-20.63	-177.71	383.6	5.7	1.9
68	2000 09 22	-29.53	-178.47	156.0	5.5	1.4
69	2000 10 11	-20.77	-177.73	495.6	5.8	2.2
70	2000 10 21	-17.40	-174.79	299.6	6.2	3.3
71	2000 11 13	-21.23	-178.90	638.2	5.6	1.7
72	2000 11 15	-21.67	170.36	155.4	5.9	2.5
73	2000 12 18	-21.08	-178.98	654.9	5.6	1.7
74	2000 12 18	-21.11	-178.98	655.7	6.5	4.7
75	2000 12 25	-21.18	-179.14	660.2	5.6	1.6
76	2000 12 30	-12.70	167.02	221.6	5.5	1.5
77	2001 03 11	-25.40	-177.59	244.7	5.8	2.0
78	2001 04 28	-18.07	-176.68	367.4	6.8	6.4
79	2001 05 19	-19.88	-177.23	392.1	5.9	2.4
80	2001 05 23	-17.82	-178.61	588.1	5.6	1.6
81	2001 05 26	-20.25	-177.65	413.9	6.3	3.8
82	2001 06 03	-29.37	-178.23	199.3	7.1	9.3
83	2001 06 14	-21.99	-179.34	603.3	5.7	1.8
84	2001 07 04	-21.81	-176.31	186.5	6.5	4.4
85	2001 07 19	-17.02	-174.32	230.1	5.8	2.1
86	2001 07 23	-22.83	-179.52	610.9	5.5	1.3

87	2001 07 31	-17.76	-178.69	575.8	5.5	1.4
88	2001 08 15	-22.47	179.39	604.2	5.6	1.6
89	2001 09 12	-20.84	-178.90	634.1	6.4	4.2
90	2001 09 13	-21.06	-179.02	629.5	5.5	1.4
91	2001 09 26	-26.48	178.34	623.1	5.8	2.1
92	2001 10 10	-23.65	-179.31	538.1	5.5	1.1
93	2001 10 22	-20.94	-179.04	639.3	5.5	1.6
94	2001 10 28	-21.72	-176.43	186.0	5.6	1.7
95	2001 11 05	-17.12	-178.96	579.7	6.2	3.3
96	2001 12 27	-14.66	167.13	161.7	6.1	3.0
97	2001 12 29	-17.62	-178.67	591.8	5.6	1.6
98	2002 01 02	-17.63	178.84	680.8	6.1	3.0
99	2002 01 04	-26.21	178.26	634.8	5.5	1.3
100	2002 01 05	-17.78	178.74	670.1	5.5	1.3
101	2002 01 25	-20.93	-178.49	586.6	5.7	1.8
102	2002 01 31	-12.57	169.76	661.9	5.7	1.7
103	2002 04 23	-12.47	166.91	218.1	5.5	1.4
104	2002 05 04	-17.68	-178.64	580.3	5.7	1.8
105	2002 05 30	-19.23	168.86	162.1	5.5	1.5
106	2002 06 16	-17.65	-178.50	588.1	5.9	2.2
107	2002 06 21	-14.79	-175.71	322.1	5.7	1.7
108	2002 06 27	-13.43	166.84	194.5	6.0	2.6
109	2002 06 30	-22.13	179.43	631.6	6.4	4.0
110	2002 07 28	-17.87	-178.23	607.2	5.5	1.5
111	2002 08 07	-21.92	-176.16	178.5	5.7	1.9
112	2002 08 09	-16.25	-175.85	381.3	6.1	2.7
113	2002 09 07	-20.29	-175.61	208.4	5.9	2.3
114	2002 09 07	-24.80	179.91	503.0	5.5	1.3
115	2002 09 08	-22.82	179.16	630.1	5.9	2.2
116	2002 10 04	-20.86	-178.74	650.8	6.3	3.6
117	2002 10 07	-18.73	169.30	253.6	5.6	1.5
118	2002 10 17	-19.80	-178.23	621.9	6.1	2.9

119	2002 10 22	-20.50	-178.30	560.5	6.1	2.9
120	2002 10 23	-30.69	-179.56	363.8	5.8	1.9
121	2002 11 11	-23.25	-179.82	554.6	5.7	1.7
122	2002 11 14	-17.96	-178.57	568.8	5.6	1.5
123	2002 12 03	-17.51	-178.69	584.1	5.5	1.5
124	2002 12 10	-24.02	179.28	538.8	6.0	2.4
125	2002 12 25	-17.62	-178.77	584.6	5.5	1.3
126	2002 12 28	-18.00	-178.40	635.5	5.8	2.0
127	2003 01 04	-20.72	-177.32	394.7	6.5	4.1
128	2003 01 20	-20.57	-177.97	561.0	5.5	1.6
129	2003 02 13	-22.34	-179.33	607.0	5.5	1.4
130	2003 02 21	-25.86	-178.04	251.8	5.8	1.9
131	2003 03 14	-17.50	-174.77	282.4	6.3	3.6
132	2003 04 02	-25.11	179.93	490.3	5.7	1.7
133	2003 05 19	-18.02	-178.42	578.5	5.9	2.2
134	2003 07 26	-17.60	-174.74	237.0	5.7	1.7
135	2003 07 27	-21.09	-176.12	215.6	6.6	4.7
136	2003 08 03	-22.66	-176.53	173.4	5.5	1.4
137	2003 08 14	-19.81	-177.65	588.8	5.9	2.2
138	2003 10 11	-17.97	-178.28	607.0	5.7	1.7
139	2003 10 15	-17.84	-178.59	594.9	5.9	2.3
140	2003 10 23	-23.84	179.98	551.3	5.7	1.8
141	2003 11 20	-24.40	-179.54	490.2	5.6	1.5
142	2003 12 16	-18.98	-177.03	386.4	5.6	1.6
143	2003 12 26	-17.24	-178.70	573.5	5.5	1.4
144	2004 01 11	-16.27	-176.05	381.4	5.9	2.1
145	2004 01 11	-20.21	-179.20	682.5	6.0	2.5
146	2004 02 01	-31.57	179.92	356.0	5.7	1.8
147	2004 03 05	-20.80	-178.68	628.7	5.5	1.4
148	2004 03 08	-20.77	-179.01	616.4	5.5	1.4
149	2004 03 12	-15.48	-174.74	290.6	5.9	2.3
150	2004 04 17	-23.66	-179.92	550.9	5.6	1.5

151	2004 05 06	-15.76	-174.74	289.2	5.6	1.6
152	2004 06 02	-23.72	179.47	560.4	5.5	1.5
153	2004 06 13	-17.99	-178.32	598.7	5.7	1.6
154	2004 06 22	-19.14	-175.29	241.9	5.5	1.4
155	2004 07 01	-25.29	-179.25	408.2	5.6	1.6
156	2004 07 15	-17.68	-178.52	577.2	7.1	8.2
157	2004 08 17	-26.45	-177.54	175.2	5.6	1.6
158	2004 11 17	-19.87	-178.40	629.4	6.5	4.3
159	2004 11 18	-20.92	-178.98	634.2	5.7	1.7
160	2004 11 21	-15.22	-174.59	270.0	5.9	2.2
161	2004 11 23	-24.26	179.11	569.4	5.8	2.1
162	2004 12 03	-34.36	179.71	155.5	5.7	1.8
163	2004 12 06	-18.84	-178.27	465.6	6.1	2.3
164	2004 12 17	-21.92	-179.15	607.4	5.8	1.9
165	2004 12 19	-17.95	-178.72	586.9	5.8	1.9
166	2004 12 20	-15.8	-174.22	256.1	5.8	1.9
167	2004 12 24	-20.21	-178.55	620.9	5.7	1.8
168	2005 01 18	-22.88	179.27	590.2	5.8	1.9
169	2005 02 22	33.15	137.16	372.2	5.6	1.6
170	2005 02 27	-17.66	-178.52	580.9	5.7	1.7
171	2005 03 16	-24.42	-179.98	525.0	5.5	1.4
172	2005 03 19	-21.88	-179.27	609.2	6.3	3.4
173	2005 03 30	-22.31	-179.64	585.1	6.1	2.8
174	2005 04 19	29.66	139.03	417.9	5.9	2.1
175	2005 05 20	-24.43	179.04	573.3	5.9	2.3
176	2005 06 07	-29.20	-178.90	326.1	5.7	1.8
177	2005 07 01	31.90	139.30	199.5	5.5	1.4
178	2005 08 06	-19.60	-175.35	217.7	6.0	2.3
179	2005 09 01	-24.55	179.92	542.8	5.6	1.4
180	2005 09 12	-17.51	-177.09	415.7	5.7	1.8
181	2005 10 14	-34.60	179.25	203.4	5.6	1.6
182	2005 10 15	25.29	123.43	194.6	6.4	4.0

183	2005 10 23	37.36	134.61	393.5	5.9	2.3
184	2005 11 21	30.97	130.31	155.0	6.2	2.9
185	2005 11 25	-25.88	-177.46	180.7	5.5	1.5
186	2005 12 01	-20.97	-178.91	651.0	5.5	1.5
187	2005 12 10	-24.61	179.95	503.7	5.6	1.5
188	2005 12 20	-25.52	179.48	529.4	5.5	1.4
189	2006 01 02	-19.80	-177.72	589.5	7.2	9.3
190	2006 01 23	-25.20	178.29	589.0	5.6	1.6
191	2006 02 02	-17.77	-178.13	611.6	6.7	5.5
192	2006 02 17	24.10	141.58	174.2	5.6	1.6
193	2006 02 24	-17.94	-179.42	640.9	6.1	2.6
194	2006 02 26	-23.59	-179.82	553.9	6.4	3.8
195	2006 03 02	-18.00	-178.24	632.9	5.5	1.4
196	2006 03 05	-20.09	-175.22	213.9	6.1	2.7
197	2006 03 20	-23.85	179.97	550.7	5.8	1.8
198	2006 03 27	-17.64	-178.72	559.3	5.6	1.6
199	2006 03 28	31.72	137.79	411.6	5.9	2.2
200	2006 04 14	-25.99	-177.44	166.8	5.5	1.4
201	2006 04 16	30.29	138.60	423.6	5.7	1.8
202	2006 05 06	-25.03	179.90	528.2	5.6	1.5
203	2006 06 02	-20.77	-178.54	584.6	6	2.4
204	2006 06 09	-17.36	-178.62	585.9	6.1	2.7
205	2006 06 09	-17.99	-178.46	601.3	5.5	1.3
206	2006 06 11	-20.66	-179.21	670.3	5.9	2.1
207	2006 06 27	-19.77	-178.04	596.7	6.3	3.3
208	2006 07 16	-19.95	-178.36	600.7	5.7	1.7
209	2006 07 18	-20.00	-178.26	600.0	5.7	1.8
210	2006 07 23	-17.97	-178.42	597.9	5.8	1.9
211	2006 07 29	-22.17	-179.37	627.6	5.5	1.3
212	2006 08 02	-31.35	179.70	454.2	5.7	1.7
213	2006 08 07	-15.76	167.63	157.7	6.8	6.1
214	2006 08 15	-21.18	-175.70	162.5	6.1	2.8

215	2006 08 21	33.65	135.94	419.1	5.5	1.3
216	2006 09 03	-23.92	179.03	568.8	5.9	2.2
217	2006 09 16	41.33	135.71	382.2	5.9	2.1
218	2006 09 29	-16.17	-176.07	379.8	5.6	1.5
219	2006 11 13	-17.77	-178.25	619.1	5.5	1.4
220	2006 12 10	-18.66	-177.90	567.5	5.5	1.4
221	2006 12 22	-17.49	-178.58	598.0	5.5	1.3
222	2007 01 08	-18.46	-177.68	423.7	6.3	3.3
223	2007 01 15	34.94	138.81	169.8	5.9	2.1
224	2007 01 28	-17.73	179.90	594.5	5.6	1.5
225	2007 03 09	43.22	133.65	451.1	6	2.5
226	2007 03 23	-18.87	-178.24	644.6	5.8	1.9
227	2007 04 01	32.31	137.67	378.4	5.7	1.8
228	2007 04 09	-20.00	-177.97	613.7	5.9	2.3
229	2007 04 17	-31.55	179.93	427.8	5.6	1.5
230	2007 05 03	-27.09	-177.79	213.7	5.5	1.3
231	2007 05 06	-19.31	-179.05	691.6	6.0	2.6
232	2007 05 06	-19.44	-179.04	690.8	6.5	4.1
233	2007 05 07	-19.37	-178.99	696.6	5.6	1.6
234	2007 05 07	-21.08	-178.48	573.2	5.7	1.7
235	2007 05 13	-19.58	-179.03	694.9	5.8	2.0
236	2007 07 01	-22.32	-179.37	610.5	5.6	1.5
237	2007 07 16	36.84	135.03	374.9	6.8	6.2
238	2007 07 26	-20.44	-178.41	583.2	5.7	1.7
239	2007 08 02	-21.61	-179.03	622.1	5.6	1.6
240	2007 08 11	-22.20	-179.00	609.9	5.7	1.7
241	2007 08 23	-19.87	-177.65	579.2	5.7	1.7
242	2007 09 14	-23.64	179.83	580.2	5.9	2.1
243	2007 09 25	-30.69	-179.85	420.6	6.2	3.0
244	2007 10 05	-25.27	179.50	540.8	6.5	4.3
245	2007 10 08	-20.60	-177.10	338.1	5.6	1.6
246	2007 10 16	-25.70	179.72	512.4	6.6	4.8

247	2007 11 19	-21.05	-178.63	562.5	6.3	3.4
248	2008 01 15	-22.05	-179.34	603.3	6.5	4.4
249	2008 01 18	-20.91	-179.00	649.2	5.5	1.3
250	2008 02 01	-21.53	-179.27	629.5	6.0	2.4
251	2008 02 07	-22.65	-178.96	494.0	5.6	1.5
252	2008 03 28	-32.6	179.57	360.3	5.7	1.7
253	2008 03 30	-26.05	-177.51	177.4	5.5	1.3
254	2008 04 10	-25.98	178.19	622.6	5.5	1.3
255	2008 04 16	39.08	140.18	169.9	5.8	1.9
256	2008 04 18	-17.26	-178.98	577.8	6.3	3.5
257	2008 05 19	42.51	131.96	530.3	5.6	1.6
258	2008 06 04	41.59	139.15	204.3	5.7	1.7
259	2008 06 15	-17.77	-179.66	623.6	5.9	2.2
260	2008 06 29	45.12	137.37	328.3	6.0	2.3
261	2008 07 03	-23.41	-179.69	589.9	6.2	3.2
262	2008 07 19	-17.22	-177.05	395.3	6.4	3.9
263	2008 07 20	27.81	139.60	485.6	5.8	2.0
264	2008 09 01	-25.51	-177.25	172.3	6.0	2.4
265	2008 09 04	-12.17	167.04	261.4	5.6	1.6
266	2008 09 05	-13.24	166.83	155.3	5.6	1.5
267	2008 09 14	-23.73	-176.87	189.9	5.5	1.3
268	2008 09 22	41.46	140.50	152.5	5.6	1.6
269	2008 10 01	30.21	138.88	393.8	5.7	1.8
270	2008 10 22	-18.40	-174.98	244.0	6.4	3.7
271	2008 11 04	-17.03	168.31	231.6	6.3	3.6
272	2008 11 05	-17.22	-174.06	185.6	5.7	1.8
273	2008 11 19	-22.20	-179.30	604.1	5.8	2.0
274	2008 11 23	-20.23	-175.12	184.5	5.5	1.3
275	2008 11 29	-18.72	-177.52	396.6	6.0	2.4
276	2008 12 09	-15.98	168.04	236.7	6.0	2.6
277	2008 12 09	-20.89	-178.62	607.4	5.7	1.7
278	2008 12 17	-17.77	-178.30	547.8	5.8	2.0

279	2008 12 18	-23.84	-179.65	562.4	5.6	1.4
280	2009 01 07	-20.62	-179.15	669.0	5.6	1.6
281	2009 01 24	-19.74	-178.90	682.5	5.6	1.5
282	2009 01 26	-17.83	-178.55	616.5	5.8	2.0
283	2009 01 27	-17.81	-178.51	612.7	5.9	2.1
284	2009 02 20	-18.44	-178.53	534.4	5.6	1.6
285	2009 03 01	-21.83	-176.16	180.1	5.5	1.4
286	2009 03 05	-17.46	-178.90	553.3	5.9	2.1
287	2009 03 26	27.32	126.93	161.0	5.9	2.1
288	2009 04 18	-20.58	-178.41	574.8	5.7	1.8
289	2009 04 26	-30.19	-178.24	151.9	6.1	2.7
290	2009 05 23	-24.40	178.99	561.0	5.5	1.3
291	2009 06 07	-22.05	-179.39	607.3	5.5	1.4
292	2009 06 08	-22.20	-179.43	607.6	5.5	1.4
293	2009 08 08	-22.82	179.24	634.9	5.5	1.3
294	2009 08 09	33.05	138.19	301.8	7.1	8.3
295	2009 08 15	-19.83	-178.17	608.4	5.6	1.5
296	2009 08 16	-17.94	-179.18	649.1	5.5	1.4
297	2009 08 18	-25.99	-178.08	277.3	6.3	3.5
298	2009 09 02	-29.24	-178.67	259.4	6.1	2.9
299	2009 09 03	31.08	130.19	168.4	6.2	3.0
300	2009 10 25	-23.00	-178.97	419.3	6.0	2.3
301	2009 11 09	-17.11	178.53	603.9	7.3	10.5
302	2009 11 12	-20.93	-178.70	583.6	5.7	1.8
303	2009 11 22	-17.72	-178.36	546.4	6.3	3.5
304	2009 11 22	-31.47	179.66	437.1	6.2	2.9
305	2009 12 24	42.12	134.93	390.4	6.3	3.5
306	2010 02 07	-23.26	-179.83	554.8	5.8	2.1
307	2010 02 07	-23.39	179.99	560.8	5.6	1.5
308	2010 02 18	42.48	130.66	578.7	6.9	6.7
309	2010 03 04	-13.65	167.00	185.1	6.4	4.1
310	2010 03 18	-23.24	-176.75	161.5	5.5	1.4

311	2010 04 10	-20.12	-175.74	278.2	5.9	2.2
312	2010 06 17	-32.9	179.94	204.8	6.0	2.3
313	2010 06 22	-19.16	-177.49	587.4	5.8	2.0
314	2010 06 30	-23.19	179.26	581.6	6.4	3.7
315	2010 07 08	-24.03	-179.70	536.5	5.8	1.8
316	2010 08 06	-21.89	-179.24	611.5	5.5	1.4
317	2010 08 10	-14.42	167.15	189.0	5.9	2.1
318	2010 08 15	-21.82	-179.61	584.6	5.5	1.4
319	2010 08 16	-20.74	-178.67	604.0	6.2	2.9
320	2010 09 05	-23.86	-179.83	559.3	5.6	1.6
321	2010 09 06	-18.25	-174.78	217.6	5.5	1.3
322	2010 11 02	46.82	146.87	362.4	5.5	1.3
323	2010 11 30	28.69	139.26	460.6	6.8	6.0
324	2010 12 11	-21.88	-179.06	603.1	5.5	1.3
325	2010 12 28	-23.49	-179.73	571.4	6.3	3.4
326	2011 01 10	-19.51	-175.58	249.6	5.6	1.5
327	2011 01 12	26.94	139.94	511.5	6.5	4.4
328	2011 01 23	-20.43	-175.73	235.1	5.8	2.0
329	2011 01 27	-38.49	176.03	158.6	5.6	1.5
330	2011 01 29	21.71	142.85	319.1	5.5	1.3
331	2011 02 21	-25.95	178.47	567.5	6.5	4.5
332	2011 03 20	-30.90	-179.66	328.8	5.7	1.6
333	2011 04 03	-17.65	-178.45	562.3	6.4	3.9
334	2011 04 05	-17.68	-178.39	567.9	5.7	1.7
335	2011 04 15	-18.65	-174.93	218.6	5.7	1.8
336	2011 05 04	-20.25	-178.40	597.2	5.6	1.5
337	2011 05 05	-25.12	-177.16	186.3	5.6	1.6
338	2011 05 28	-27.12	-178.49	314.2	5.5	1.4
339	2011 05 28	-27.14	-178.26	318.0	5.5	1.4
340	2011 06 25	-24.51	179.58	538.6	5.6	1.5
341	2011 07 05	-38.63	175.68	159.1	5.5	1.4
342	2011 07 19	-23.69	179.18	557.9	5.5	1.4

343	2011 07 22	-20.18	-178.51	604.7	5.9	2.2
344	2011 07 29	-23.78	179.92	539.0	6.7	5.6
345	2011 08 02	-23.96	179.16	546.4	5.7	1.8
346	2011 08 07	-11.69	168.31	409.3	5.7	1.6
347	2011 08 11	-24.68	179.99	503.5	5.7	1.8
348	2011 08 12	-21.86	-176.63	214.6	5.6	1.5
349	2011 08 19	-16.52	-176.73	415.0	6.2	3.2
350	2011 08 27	-24.47	179.96	516.8	5.7	1.7
351	2011 09 03	-20.79	169.72	151.6	7.0	8.0
352	2011 09 07	-27.80	-178.15	258.0	5.5	1.4
353	2011 09 15	-14.89	-177.77	375.5	5.6	1.5
354	2011 09 15	-21.61	-179.21	624.9	7.3	11.1
355	2011 10 04	26.73	140.35	439.6	5.7	1.6
356	2011 10 15	-25.71	-177.11	166.8	5.5	1.3
357	2011 10 21	43.83	142.52	191.5	6.2	2.9
358	2011 10 27	-17.98	-179.40	608.7	6.0	2.4
359	2011 10 30	25.32	122.91	213.1	5.7	1.7
360	2011 11 08	27.13	125.77	230.6	6.9	7.0
361	2011 11 30	-22.20	-176.31	170.9	5.6	1.5
362	2011 12 09	46.93	144.60	390.0	5.8	1.8
363	2011 12 11	-24.03	178.51	571.2	5.7	1.6
364	2012 01 01	31.61	138.17	352.0	6.8	6.1
365	2012 01 24	-25.00	178.72	581.8	6.3	3.6
366	2012 02 10	-17.98	-178.42	598.0	5.9	2.3
367	2012 02 26	-18.35	-178.30	609.5	5.5	1.3
368	2012 02 27	-20.21	-178.77	621.4	5.5	1.3
369	2012 02 28	28.23	139.31	504.1	5.5	1.4
370	2012 05 26	26.87	140.17	472.1	6.0	2.3
371	2012 05 28	-20.03	-175.51	212.2	5.9	2.2
372	2012 05 29	-22.12	-179.37	596.4	5.8	2.0
373	2012 06 07	-20.37	-175.96	276.7	5.9	2.1
374	2012 06 21	-17.97	-178.15	552.6	5.5	1.3

375	2012 07 03	-40.05	173.63	230.4	6.3	3.5
376	2012 07 06	-14.74	167.19	168.7	6.4	3.8
377	2012 07 18	-20.78	-178.49	544.2	5.9	2.2
378	2012 07 20	-21.26	-179.30	639.3	5.5	1.4
379	2012 07 29	47.29	138.90	506.9	5.7	1.8
380	2012 08 05	-21.03	-178.26	491.0	5.8	1.9
381	2012 09 20	-20.64	-178.30	569.6	5.7	1.7
382	2012 10 23	29.07	139.19	443.0	5.9	2.3
383	2012 10 25	-19.78	-178.13	606.0	5.5	1.4
384	2012 10 30	-18.04	-178.47	578.7	5.5	1.4
385	2012 11 12	-24.13	178.87	551.2	5.7	1.8
386	2012 11 12	29.79	137.91	506.0	5.7	1.8
387	2012 11 29	-21.03	-178.67	544.3	5.5	1.5
388	2012 11 29	-28.07	-178.02	252.6	5.5	1.3
389	2012 11 30	-18.87	-175.15	233.3	5.6	1.6
390	2012 12 07	-38.31	176.08	165.1	6.3	3.6
391	2013 02 12	-18.05	-177.85	534.6	5.6	1.5
392	2013 02 16	-36.10	178.20	185.2	5.8	2.0
393	2013 02 26	-21.48	-179.31	626.1	5.8	1.9
394	2013 03 01	21.86	144.22	152.1	5.5	1.3
395	2013 04 05	42.77	131.02	571.9	6.3	3.3
396	2013 04 06	42.82	131.05	575.2	5.8	1.9
397	2013 04 21	30.02	138.88	429.8	6.1	2.8
398	2013 04 26	-28.67	-178.82	356.0	6.2	2.9
399	2013 05 11	-17.89	-174.74	242.2	6.3	3.6
400	2013 05 12	22.01	143.95	156.1	5.5	1.4
401	2013 05 23	-20.67	-175.29	160.4	6.3	3.4
402	2013 06 07	-23.83	179.07	557.1	5.9	2.2
403	2013 06 15	-33.82	179.63	200.4	6.0	2.5
404	2013 07 24	-23.23	-176.81	169.2	6.0	2.3
405	2013 08 04	46.97	145.22	378.0	5.8	2.0
406	2013 08 08	-20.37	-176.22	262.9	5.5	1.3

407	2013 08 12	-30.46	-179.58	347.9	6.1	2.9
408	2013 08 28	-27.73	179.84	492	6.2	3.2
409	2013 08 29	-19.35	-178.94	684.6	5.8	1.9
410	2013 08 31	47.86	148.12	389.3	5.7	1.8
411	2013 09 02	42.19	133.65	454.7	5.7	1.7
412	2013 09 04	30.02	138.79	412.0	6.5	4.4
413	2013 09 06	20.24	122.31	187.7	6.0	2.4
414	2013 10 11	-30.57	-178.43	155.5	6.2	3.1
415	2013 10 23	-23.08	-176.74	168.4	6.0	2.4
416	2013 11 18	34.35	136.86	339.9	5.7	1.7
417	2013 11 23	-17.09	-176.38	386.6	6.5	4.3
418	2013 11 24	-24.3	179.18	535.4	5.7	1.6
419	2013 12 01	-17.46	-178.33	544.0.	5.7	1.8
420	2013 12 04	-25.40	178.29	586.0	5.8	1.8
421	2013 12 17	-20.64	-178.75	614.2	5.7	1.7
422	2013 12 25	-17.87	-178.08	597.3	5.6	1.6
423	2014 01 01	-13.89	167.10	198.2	6.5	4.5
424	2014 01 10	-31.27	-179.49	217.4	5.7	1.7
425	2014 03 23	-20.63	-178.83	621.0	5.8	2.0
426	2014 03 26	-26.13	179.59	493.2	5.8	1.9
427	2014 03 26	-26.14	179.32	510.0	6.4	3.7
428	2014 04 09	-14.62	-176.09	341.2	5.5	1.4
429	2014 05 04	-24.67	179.12	529.6	6.6	4.7
430	2014 05 04	-25.80	178.25	654.5	6.4	3.8
431	2014 05 04	34.89	139.48	165.2	6.0	2.5
432	2014 05 09	-18.99	-175.15	228.1	6.0	2.3
433	2014 06 30	28.42	138.75	522.9	6.2	3.2
434	2014 07 03	-22.07	-179.57	602.2	5.5	1.3
435	2014 07 19	-15.64	-174.18	233.8	6.2	3.1
436	2014 07 21	-19.68	-178.32	627.1	6.9	7.0
437	2014 09 10	-24.76	179.26	540.6	5.6	1.6
438	2014 09 16	-22.30	-179.54	589.5	5.6	1.5

439	2014 09 21	28.01	139.46	486.3	5.5	1.3
440	2014 09 30	-17.85	-178.59	587.0	5.5	1.3
441	2014 11 01	-19.76	-177.61	445.4	7.1	8.7
442	2014 11 17	-21.52	-179.23	625.0	5.5	1.3
443	2014 12 10	25.51	122.40	262.0	6.1	2.9
444	2014 12 11	-20.96	-179.06	618.4	5.7	1.8
445	2014 12 12	-18.83	-176.43	328.0	5.8	1.9
446	2014 12 27	-17.93	-179.48	632.6	5.5	1.3
447	2014 12 30	-20.27	-178.59	611.5	6.0	2.5
448	2014 12 31	-20.28	-178.61	608.6	5.9	2.3
449	2014 12 31	-25.73	178.37	606.6	5.5	1.4
450	2015 01 23	-17.06	168.36	231.0	6.8	6.0
451	2015 01 28	-20.97	-178.23	487.5	6.2	3.0
452	2015 03 08	-19.84	-177.95	566.3	5.5	1.4
453	2015 03 17	-17.79	-178.57	560.0	5.6	1.5
454	2015 03 22	-17.84	-178.48	615.8	6.1	2.7
455	2015 04 02	-17.68	-178.57	563.8	5.9	2.2
456	2015 04 03	-17.28	-176.98	386.2	5.8	1.9
457	2015 04 21	-18.32	-178.08	499.6	5.7	1.8
458	2015 04 28	-20.79	-178.71	591.4	6.1	2.7
459	2015 05 06	-25.59	178.17	618.6	5.6	1.5
460	2015 05 20	-19.35	-175.14	206.0	6.0	2.5
461	2015 06 03	-19.70	-179.01	681.4	5.5	1.3
462	2015 06 16	-20.42	-178.93	664.5	6.0	2.5
463	2015 06 20	-23.53	-176.82	157.4	5.9	2.3
464	2015 06 21	-20.34	-178.36	571.1	6.0	2.4
465	2015 06 23	27.68	139.85	458.5	6.5	4.4
466	2015 07 07	-23.15	-176.82	171.4	5.8	2.0
467	2015 07 09	-18.70	-177.10	367.0	5.5	1.3
468	2015 07 17	-18.05	-178.18	549.3	5.8	2
469	2015 08 03	-16.45	-174.14	183.7	5.7	1.8
470	2015 08 06	-26.46	-178.15	270.4	6.0	2.5

471	2015 08 24	-30.33	-178.86	243.2	6.0	2.5
472	2015 09 01	-29.62	178.67	583.3	5.7	1.7
473	2015 09 03	-15.43	-174.61	244.9	5.5	1.3
474	2015 09 06	-24.99	179.93	492.2	5.5	1.4
475	2015 09 07	-24.28	179.07	551.6	5.8	2.0
476	2015 10 20	27.16	140.19	317.7	5.7	1.7
477	2015 10 24	-30.19	-179.2	321.5	5.5	1.3
478	2015 10 28	-11.03	166.29	151.4	5.8	1.9
479	2015 11 02	-18.27	-177.96	631.0	5.6	1.6
480	2015 11 26	-17.7	179.89	629.8	5.7	1.7
481	2015 12 06	-18.06	-178.61	558.3	5.6	1.5
482	2015 12 18	-16.95	-178.82	557.9	5.5	1.3
483	2016 01 02	44.83	129.75	587.4	5.8	2.0
484	2016 01 05	22.03	143.87	174.7	5.7	1.7
485	2016 01 11	-23.18	179.11	576.0	5.6	1.6
486	2016 01 11	44.46	141.01	253.9	6.3	3.3
487	2016 01 13	-15.10	-174.67	264.2	5.9	2.2
488	2016 01 26	-20.46	-177.49	526.9	5.7	1.6
489	2016 02 01	-30.81	-179.82	390.6	6.3	3.3
490	2016 02 02	25.51	123.38	201.0	5.7	1.8
491	2016 02 14	30.43	138.67	421.5	5.8	1.8
492	2016 02 20	-22.01	-179.4	593.0	5.8	1.9
493	2016 03 04	-20.88	-179.03	628.6	5.5	1.3
494	2016 03 14	29.76	129.11	225.8	5.6	1.6
495	2016 03 29	-32.97	179.77	248.8	5.5	1.3
496	2016 04 20	-19.26	-177.28	368.0	5.6	1.6
497	2016 04 25	-17.91	-178.33	602.5	5.7	1.7
498	2016 05 08	-21.91	-179.41	599.0	5.5	1.4
499	2016 05 13	-25.58	179.23	535.8	5.7	1.7
500	2016 05 27	-20.77	-178.61	581.4	6.4	4.1
501	2016 05 28	-22.13	-178.17	417.5	6.9	7.0
502	2016 05 31	25.42	122.35	250.4	6.4	3.7

503	2016 06 03	-16.15	-175.75	361.5	5.6	1.5
504	2016 06 15	-13.39	167.04	201.3	5.5	1.4
505	2016 07 10	-14.66	167.22	170.3	5.6	1.6
506	2016 07 18	-19.22	-177.33	589.1	5.5	1.3
507	2016 07 20	-18.97	168.85	174.8	6.1	2.7
508	2016 07 23	47.68	146.91	423.2	5.8	2.0
509	2016 08 04	24.98	141.91	522.7	6.3	3.3
510	2016 08 22	29.95	138.89	408.8	5.6	1.5
511	2016 08 25	30.69	137.78	473.2	5.9	2.2
512	2016 09 03	31.78	137.96	343.4	5.5	1.3
513	2016 09 21	-18.08	-175.12	269.4	5.5	1.3
514	2016 09 24	-18.17	-174.72	207.4	6.4	3.9
515	2016 09 24	-19.77	-178.15	606.8	6.9	7.0
516	2016 10 01	-23.69	-179.85	540.7	5.8	2.0
517	2016 10 18	-23.39	-179.78	551.8	5.9	2.3
518	2016 10 20	-18.02	-179.40	649.5	5.5	1.3
519	2016 11 10	-20.31	-178.43	560.7	5.6	1.6
520	2016 11 12	-24.87	178.64	565.9	5.9	2.1
521	2016 11 23	27.36	140.02	491.1	5.8	2.0
522	2016 11 30	-21.37	-179.18	628.8	5.5	1.3
523	2016 12 03	-22.62	-176.13	165.7	5.5	1.3
524	2016 12 17	-26.80	-177.19	192.6	5.6	1.5
525	2017 01 02	-23.29	179.29	572.8	6.3	3.5
526	2017 01 02	-9.680	155.10	23.70	5.1	0.9
527	2017 02 08	-18.02	-178.40	642.7	5.8	1.9
528	2017 02 24	-17.93	-178.42	592.5	5.9	2.2
529	2017 02 24	-23.44	-178.77	417.9	6.9	7.3
530	2017 02 26	-18.45	169.20	267.5	5.6	1.5
531	2017 04 05	-19.02	169.39	266.1	5.7	1.6
532	2017 04 13	-18.30	-178.05	503.8	5.8	1.9
533	2017 04 18	-18.03	-178.37	646.5	6.1	2.7
534	2017 04 19	-13.95	170.08	619.3	5.6	1.5

535	2017 05 09	-14.55	167.20	181.4	6.8	5.9
536	2017 05 16	-23.71	-177.42	264.0	5.7	1.8
537	2017 06 17	-24.15	179.66	537.5	6.1	2.7
538	2017 06 19	-20.72	-176.46	293.1	5.9	2.1
539	2017 06 29	-30.93	-179.92	409.5	6.0	2.6
540	2017 07 30	-20.88	-178.81	577.9	5.7	1.7
541	2017 08 19	-17.80	-178.77	559.8	6.5	4.3
542	2017 09 05	-16.21	167.82	190.0	5.6	1.5
543	2017 09 20	-18.85	168.95	208.0	6.4	4.0
544	2017 09 26	-23.88	-179.90	566.2	5.7	1.6
545	2017 09 28	-24.92	-179.64	483.5	5.5	1.3

Table B2 Events list used in chapter 4

Event #	Date (YYYY MM DD)	Latitude (˚)	Longitude (˚)	Depth (km)	Mw	Half dur. (sec.)
1	2000 01 10	27.3	140.3	454.4	5.7	1.7
2	2001 01 14	22.2	143.9	112.5	5.9	2.2
3	2000 01 28	25.9	124.6	200.8	6.0	2.5
4	2002 02 01	45.5	136.7	369.6	5.8	2.0
5	2001 02 07	52.7	154.0	434.2	5.7	1.8
6	2000 02 13	42.8	131.6	524.3	6.0	2.4
7	2001 02 14	48.6	153.3	149.1	5.6	1.5
8	2001 02 26	46.8	144.5	396.4	6.0	2.7
9	2002 03 07	48.0	146.9	453.8	5.6	1.4
10	2000 04 21	35.7	135.3	357.7	5.5	1.4
11	2002 05 21	44.6	146.7	146.0	5.5	1.3
12	2000 06 09	30.4	138.0	484.7	5.7	1.8
13	2002 06 28	43.7	130.5	581.5	7.3	10.9
14	2001 07 03	21.7	143.0	307.7	6.4	4.0
15	2004 07 08	47.1	151.7	132.8	6.3	3.4
16	2000 07 10	46.8	145.6	361.3	5.8	1.9
17	2002 07 17	48.5	153.3	143.9	5.5	1.6
18	2003 07 27	47.0	139.2	477.2	6.7	5.5
19	2002 08 02	29.4	139.3	441.5	6.2	3.2
20	2000 08 06	28.9	139.7	411.3	7.3	10.3
21	2000 08 27	22.3	143.8	105.7	5.6	1.6
22	2003 08 31	43.4	132.4	493.0	6.1	2.7
23	2002 09 15	44.8	130.0	589.4	6.4	3.7
24	2001 10 03	47.0	148.6	288.1	5.9	2.3
25	2000 10 14	23.4	142.1	123.6	5.5	1.6
26	2004 10 15	24.5	122.7	102.1	6.6	4.7
27	2002 10 16	51.8	157.6	104.7	6.2	3.2
28	2000 10 27	26.3	140.7	387.6	6.0	2.8
29	2002 11 05	49.1	142.3	604.0	5.6	1.6

30	2004 11 07	47.9	144.5	493.0	6.1	2.8
31	2003 11 11	22.4	143.5	107.1	5.9	2.2
32	2003 11 12	33.3	137.1	381.8	6.3	3.6
33	2001 12 02	39.5	141.1	123.7	6.4	4.3
34	2000 12 22	44.8	147.1	140.8	6.1	3.0
35	2005 02 22	33.2	137.2	372.2	5.6	1.6
36	2005 04 19	29.7	139.0	417.9	5.9	2.1
37	2005 07 01	31.9	139.3	199.5	5.5	1.4
38	2005 09 21	43.9	146.4	107.2	6.0	2.5
39	2005 10 15	25.3	123.4	194.6	6.4	4.0
40	2005 10 23	37.4	134.6	393.5	5.9	2.3
41	2005 11 21	31.0	130.3	155.0	6.2	2.9
42	2005 11 23	50.0	147.8	638.8	5.5	1.4
43	2006 02 17	24.1	141.6	174.2	5.6	1.6
44	2006 03 28	31.7	137.8	411.6	5.9	2.2
45	2006 04 16	30.3	138.6	423.6	5.7	1.8
46	2006 05 22	54.2	158.9	198.0	6.2	3.0
47	2006 06 11	33.2	131.3	144.5	6.4	3.7
48	2006 06 22	45.4	149.5	104.8	5.9	2.3
49	2006 08 21	33.7	135.9	419.1	5.5	1.3
50	2006 09 16	41.3	135.7	382.2	5.9	2.1
51	2006 11 22	44.1	146.8	105.5	5.6	1.6
52	2007 01 15	34.9	138.8	169.8	5.9	2.1
53	2007 03 08	29.9	140.5	135.2	6.1	2.7
54	2007 03 09	43.2	133.7	451.1	6.0	2.5
55	2007 03 12	46.8	152.1	136.3	5.6	1.5
56	2007 03 30	44.1	146.2	102.9	5.5	1.4
57	2007 04 01	32.3	137.7	378.4	5.7	1.8
58	2007 04 18	42.7	142.0	125.6	5.5	1.4
59	2007 05 30	52.0	157.8	123.0	6.4	4.0
60	2007 07 01	43.6	144.8	130.2	5.8	1.9
61	2007 07 16	36.8	135.0	374.9	6.8	6.2

62	2007 08 22	42.1	140.8	126.9	5.6	1.5
63	2007 08 28	49.6	154.8	117.6	5.6	1.5
64	2007 09 03	45.8	150.3	100.3	6.2	3.0
65	2008 03 06	51.4	157.0	123.3	5.5	1.3
66	2008 04 16	39.1	140.2	169.9	5.8	1.9
67	2008 05 19	42.5	132.0	530.3	5.6	1.6
68	2008 06 04	41.6	139.2	204.3	5.7	1.7
69	2008 06 29	45.1	137.4	328.3	6.0	2.3
70	2008 07 20	27.8	139.6	485.6	5.8	2.0
71	2008 09 09	24.6	122.5	108.7	5.5	1.3
72	2008 09 22	41.5	140.5	152.5	5.6	1.6
73	2008 10 01	30.2	138.9	393.8	5.7	1.8
74	2008 11 24	54.3	154.7	502.3	7.3	10.9
75	2009 02 28	42.6	142.1	111.2	5.5	1.3
76	2009 03 26	27.3	126.9	161.0	5.9	2.1
77	2009 04 21	50.6	155.6	151.8	6.2	3.0
78	2009 07 29	22.7	143.2	128.0	5.5	1.3
79	2009 08 09	33.1	138.2	301.8	7.1	8.3
80	2009 09 03	31.1	130.2	168.4	6.2	3.0
81	2009 10 10	47.8	152.8	125.6	5.9	2.3
82	2009 12 10	53.4	152.8	655.7	6.3	3.4
83	2009 12 24	42.1	134.9	390.4	6.3	3.5
84	2010 01 15	26.6	126.5	135.5	5.7	1.8
85	2010 02 18	42.5	130.7	578.7	6.9	6.7
86	2010 07 25	49.6	155.0	136.3	5.6	1.5
87	2010 11 02	46.8	146.9	362.4	5.5	1.3
88	2010 11 07	24.4	141.7	102.7	5.6	1.6
89	2010 11 30	28.7	139.3	460.6	6.8	6.0
90	2011 01 12	26.9	139.9	511.5	6.5	4.4
91	2011 01 29	21.7	142.9	319.1	5.5	1.3
92	2011 02 22	22.2	144.0	106.3	5.5	1.4
93	2011 04 16	25.3	124.0	138.1	5.8	1.9

94	2011 05 10	43.6	131.0	564.5	5.7	1.7
95	2011 07 18	52.8	153.0	499.1	5.5	1.3
96	2011 10 04	26.7	140.4	439.6	5.7	1.6
97	2011 10 21	43.8	142.5	191.5	6.2	2.9
98	2011 10 30	25.3	122.9	213.1	5.7	1.7
99	2011 11 08	27.1	125.8	230.6	6.9	7.0
100	2011 12 09	46.9	144.6	390.0	5.8	1.8
101	2012 01 01	31.6	138.2	352.0	6.8	6.1
102	2012 02 28	28.2	139.3	504.1	5.5	1.4
103	2012 03 12	45.1	147.9	124.9	5.6	1.5
104	2012 03 15	35.9	139.5	101.5	5.5	1.4
105	2012 05 26	26.9	140.2	472.1	6.0	2.3
106	2012 07 29	47.3	138.9	506.9	5.7	1.8
107	2012 10 23	29.1	139.2	443.0	5.9	2.3
108	2012 11 12	29.8	137.9	506.0	5.7	1.8
109	2013 02 02	42.9	143.2	105.3	6.9	7.1
110	2013 03 01	21.9	144.2	152.1	5.5	1.3
111	2013 04 05	42.8	131.0	571.9	6.3	3.3
112	2013 04 06	42.8	131.1	575.2	5.8	1.9
113	2013 04 19	46.0	150.9	104.5	7.3	10.3
114	2013 04 21	30.0	138.9	429.8	6.1	2.8
115	2013 05 12	22.0	144.0	156.1	5.5	1.4
116	2013 05 24	52.4	151.5	642.4	6.7	5.6
117	2013 08 04	47.0	145.2	378.0	5.8	2.0
118	2013 08 31	47.9	148.1	389.3	5.7	1.8
119	2013 09 02	42.2	133.7	454.7	5.7	1.7
120	2013 09 04	30.0	138.8	412.0	6.5	4.4
121	2013 09 06	20.2	122.3	187.7	6.0	2.4
122	2013 10 01	53.2	152.8	585.5	6.7	5.6
123	2013 11 18	34.4	136.9	339.9	5.7	1.7
124	2014 03 02	27.3	127.5	124.9	6.5	4.3
125	2014 05 04	34.9	139.5	165.2	6.0	2.5

126	2014 06 30	28.4	138.8	522.9	6.2	3.2
127	2014 09 18	50.8	149.9	504.4	5.6	1.5
128	2014 09 21	28.0	139.5	486.3	5.5	1.3
129	2014 10 02	52.3	158.4	151.7	5.8	1.9
130	2014 12 10	25.5	122.4	262.0	6.1	2.9
131	2015 06 23	27.7	139.9	458.5	6.5	4.4

Appendix C Supporting information

Slab volume calculation

We calculate the volume of the slabs in D″ for three different subduction zone, the western Pacific, the northern Pacific, and the Caribbean Sea, using our group's tomography models (Suzuki et al., 2019 for the western Pacific; Suzuki et al., 2016 for the northern Pacific; Borgeaud et al., 2017 for the Caribbean Sea). Since the parameterization of these models are different (5˚ x 5˚ x 100 km for northern Pacific; 150 km x 150 km x 50 km for northern Pacific; 5˚ x 5˚ x 50 km for the Caribbean Sea), we resample the model parameter as 1˚ x 1˚ x 50 km using nearest three points interpolation. We defined the threshold for slab region as $\delta Vs > +0.3$ percent.